



## Durham E-Theses

---

### *Drying Agrochemical Droplets on Model Surfaces*

PINEIRO-ROMERO, AXA,AZAHARA

#### How to cite:

---

PINEIRO-ROMERO, AXA,AZAHARA (2019) *Drying Agrochemical Droplets on Model Surfaces*, Durham theses, Durham University. Available at Durham E-Theses Online: <http://etheses.dur.ac.uk/12984/>

#### Use policy

---

The full-text may be used and/or reproduced, and given to third parties in any format or medium, without prior permission or charge, for personal research or study, educational, or not-for-profit purposes provided that:

- a full bibliographic reference is made to the original source
- a [link](#) is made to the metadata record in Durham E-Theses
- the full-text is not changed in any way

The full-text must not be sold in any format or medium without the formal permission of the copyright holders.

Please consult the [full Durham E-Theses policy](#) for further details.

# Drying Agrochemical Droplets on Model Surfaces

*A thesis submitted in partial fulfilment of the requirements for the degree of  
Doctor of Philosophy at the University of Durham by*

Axa Piñeiro Romero



Department of Chemistry

Durham University

October 2018

# **I. Dedication**

I dedicate this work to my parents, Jorge Antonio Piñeiro Cristín and Mercedes Romero Blanco, and my Tita Cay.

## II. Acknowledgements

Though only my name appears on the cover of this thesis, many people have contributed to its production. I owe my gratitude to all those people who have made this thesis possible and because of whom my PhD experience has been one that I will cherish forever.

My deepest gratitude is to my supervisor Colin Bain for his invaluable guidance, perseverance, understanding and advice received. Thank you to the Bain group. Special thanks to Lisong Yang, thank you for your magic hands that saved me thousands of times and Ceyla Yorucu, thank you because without you some parts of this thesis would have not been able to be written. Jing Shi and Matthew Royle who helped me when I was away!. Also, thank you to Jonathan Millican, because even not being in my research group you have been one of my biggest supports during my thesis in Durham. Finally, this thesis could not have been finished without the support of AkzoNobel, especially Dennis Selse, Solmaz Bayati, Turgut Battal and Sakis Tsetsilas from Agro and Analytical group who helped me stay motivated until the end of my PhD.

I really need to thank every single *Son of Durham* who stayed with me during these long four years because each of you gave my unforgettable moments: Antonio, my Durham HC: Celia and Nuria, Manu, Cristiano, Juan, Aritz, Stina... It is impossible to name all of you.

Lastly, I want to thank all my family for encouraging me in any decision. You are always there for me.

Thank you! ¡Gracias! Tak! 謝謝!

### **III. Declaration**

MATLAB post-processing codes were composed by Lisong Yang and Mario Possiwan at the University of Durham.

NMR measurements were advised and processed in collaboration with Juan Aguilar Malavia the University of Durham.

### **Copyright**

The copyright of this thesis rests with the author. No quotation from it should be published without the prior written consent and information derived from it should be acknowledged.

## IV. Abstract

This project addressed the mechanism of the action of surfactants, used as agrochemical adjuvants, and the physico-chemical interaction between adjuvants and a fungicide active ingredient (AI), on a model surface. The first part of the project studied the influence of surfaces with different wettabilities on the mode of evaporation for water droplets, as a reference, and then with different surfactant solutions at different concentrations with and without the addition of AI. In order to do that, a reproducible method to print droplets with the specific size for agrochemical applications was developed. The internal flows for different agrochemical solutions were studied to understand the transport of surfactants and particles within the droplets.

Two main agrochemical formulations were used: an alkyl ethoxylate surfactant (Surf1) and an amidoamine-based surfactant (Surf2) both with the addition of a fungicide called Tebuconazole resulting in a suspension and an emulsion respectively. The properties of the bulk solutions were analysed by surface tensiometry and proton nuclear magnetic resonance ( $^1\text{H-NMR}$ ) to determine the ability of these surfactants to form micelles and solubilise a hydrophobic active ingredient (AI). Diffusion-ordered spectroscopy (DOSY) showed that only Surf1 formed micelles. There was no difference in the diffusion coefficient for Surf2 at any of the concentrations tested, from which it can be concluded that Surf2 does not form micelles.

The evaporation of droplets made of different solutions gave different dried deposits on a substrate. Different strategies were developed to control the deposit structure in order to inhibit the coffee-ring effect (CRE): i) a sol-gel transition in a suspension of a nanoparticle clay (Laponite) and ii) silica particles; both added to the alkyl ethoxylate surfactant. The addition of Laponite and silica particles increased the surface tension of the final formulations at any of the concentrations. The purpose of these two strategies was to obtain more uniform deposits so that the amount of surfactant and AI were more equal along the deposit. However, Laponite formed uniform deposits because the contact line (CL) receded producing deposits of a smaller area and silica particles did not suppress the CRE. “Superspreaders” such as Silwet Gold, an

organosilicone surfactant, and Capstone® FS30, a fluorosurfactant, were added to the amidoamine-based surfactant in order to lower the contact angle of the oil drops after drying to increase the contact between the agrochemical solution and the surface, and thus increase the efficacy. The contact angle of the small droplets inside the deposit was lower when Silwet Gold was added to Surf2 + AI at 0.03 wt%.

The morphology of the dried deposit and the spatial distribution of the AI particles were analysed by scanning electron microscopy (SEM) and the chemical composition was analysed by energy dispersive X-ray spectroscopy (EDS) and Raman spectroscopy. A Raman imaging system was developed to improve the ability to map compounds on a surface. Raman imaging had the required sensitivity to confirm the co-localization of surfactant and AI molecules in the dried deposit. A quantitative method to achieve compositions by Raman spectroscopy was developed.

The last part of the thesis consists of a study of the penetration of AI through the cuticle of *Clivia Regel Minata* in a Franz diffusion cell by two different methods: infinite dose system and simulation of foliar penetration (SOFP). *Clivia* is selected as a model plant as it does not have stomata that might affect the transport of AI<sup>1</sup>. The penetration of AI was improved by the addition of surfactant to the formulation. Surfactants below the CMC behaved very similarly to the surfactant-free formulations. Surfactants above CMC or above the solubility limit showed the highest penetration for the infinite dose experiments. In SOFP, the difference in AI penetration between the formulations were not significantly different. Franz cell diffusion is a useful method to study the trends for the penetration of AI through the cuticles of the leaves, however, the leaf-to-leaf variation is still too large to draw firm conclusions about foliar efficiency.

# V. Contents

<i>I. Dedication.....</i>	<i>ii</i>
<i>II. Acknowledgements .....</i>	<i>iii</i>
<i>III. Declaration .....</i>	<i>iv</i>
<i>IV. Abstract.....</i>	<i>v</i>
<i>V. Contents.....</i>	<i>vii</i>
<i>VI. Symbols list.....</i>	<i>xii</i>
<i>VII. Abbreviations.....</i>	<i>xvi</i>
<b>1. Introduction.....</b>	<b>1</b>
<b>1.1 Challenges of crop protection application.....</b>	<b>1</b>
<b>1.2 Aerial spray on plants .....</b>	<b>3</b>
<b>1.3 Leaf surface characteristic, routes for pesticide penetration and     environmental factors affecting foliar-applied herbicide uptake.....</b>	<b>4</b>
1.3.1 Leaf surface characteristic .....	4
1.3.2 Pathways of diffusion across plant cuticles .....	6
1.3.3 Environmental factors affecting foliar-applied herbicide uptake .....	7
<b>1.4 Surfactants .....</b>	<b>8</b>
1.4.1 Physico-chemical properties of surfactants .....	8
1.4.2 Thermodynamics of micellization.....	12
1.4.3 Micellar solubilisation: Basic thermodynamic principles.....	14



1.4.4	Surfactant concentration in relation to pesticide uptake .....	16
<b>1.5</b>	<b>From the nozzle to the model surface .....</b>	<b>18</b>
<b>1.6</b>	<b>Diffusion experiments across plant cuticles.....</b>	<b>20</b>
<b>1.7</b>	<b>Clivia Miniata Regel as a model cuticle.....</b>	<b>23</b>
<b>1.8</b>	<b>Tebuconazole as a model compound .....</b>	<b>24</b>
<b>2.</b>	<b><i>Evaporation Dynamics of Sessile Droplets .....</i></b>	<b>26</b>
2.1	Wettability of a sessile droplet.....	26
2.2	Geometry of a sessile droplet .....	29
2.3	Evaporation of a sessile droplet: single solvent fluids.....	31
2.4	Particle transport in drying droplets.....	34
2.4.1	The “coffee ring effect” .....	34
2.4.2	Marangoni flows.....	36
2.5	Evaporation of complex liquids .....	37
2.5.1	Influence of aqueous surfactant solutions on droplet evaporation .....	37
2.5.2	Influence of colloidal suspensions on droplet evaporation.....	38
<b>3.</b>	<b><i>Experimental methods: instrumentation and procedures .....</i></b>	<b>39</b>
3.1	Substrate preparation .....	39
3.2	Fluid preparation.....	40
3.3	Experimental set up for printing system .....	41
3.4	Pendant drop tensiometry and contact angle measurements.....	45
3.4.1	Surface tensiometry.....	45
3.4.2	Contact angle measurements .....	47

3.5	<b>Raman spectroscopy .....</b>	<b>50</b>
3.6	<b>Proton nuclear magnetic resonance (<sup>1</sup>H NMR) and Diffusion-ordered NMR spectroscopy (DOSY NMR).....</b>	<b>52</b>
3.6.1	Sample preparation .....	53
3.7	<b>Scanning electron microscopy (SEM) and Energy-Dispersive X-Ray Spectroscopy (EDS).....</b>	<b>54</b>
3.7.1	Sample preparation .....	55
3.8	<b>Liquid Chromatography-Mass Spectroscopy (LC-MS).....</b>	<b>56</b>
4.	<b><i>Determination of physico-chemical properties .....</i></b>	<b>58</b>
4.1	<b>Introduction .....</b>	<b>58</b>
4.2	<b>Formulations .....</b>	<b>59</b>
4.3	<b>Surface tension .....</b>	<b>60</b>
4.4	<b><sup>1</sup>H-NMR and Diffusion resolution in DOSY.....</b>	<b>62</b>
4.5	<b>Solubility of AI in nonionic surfactant solutions.....</b>	<b>67</b>
4.6	<b>Summary .....</b>	<b>71</b>
5.	<b><i>Residual droplet patterns on substrates with different wettabilities and evaporation modes.....</i></b>	<b>73</b>
5.1	<b>Introduction .....</b>	<b>73</b>
5.2	<b>Experimental.....</b>	<b>76</b>
5.3	<b>Water droplets on hydrophilic and hydrophobic substrates .....</b>	<b>77</b>
5.4	<b>Aqueous surfactant solutions on hydrophobic substrates.....</b>	<b>80</b>
5.5	<b>Aqueous surfactant solutions + Active ingredient: Colloidal suspensions.....</b>	<b>87</b>

5.5.1	Variation of the contact angle and diameter during the different modes of evaporation for agrochemical solutions with and without AI.....	90
<b>5.6</b>	<b>Effect of variations in temperature of the substrate and relative humidity ..</b>	<b>93</b>
5.6.1	Temperature of the substrate .....	94
5.6.2	Humidity variation .....	95
<b>5.7</b>	<b>Control of the deposit morphology through an evaporation-driven sol-gel transition.....</b>	<b>96</b>
5.7.1	Preparation of the Laponite and silica suspension: .....	99
5.7.2	Surface tension measurements of the solutions.....	99
5.7.3	Morphology of the dried deposit after the addition of additives .....	100
<b>5.8</b>	<b>Addition of “Superspreaders” .....</b>	<b>103</b>
<b>5.9</b>	<b>Summary .....</b>	<b>111</b>
<b>6.</b>	<b><i>Chemical characterization of the residual droplet patterns .....</i></b>	<b><i>113</i></b>
<b>6.1</b>	<b>Introduction .....</b>	<b>113</b>
<b>6.2</b>	<b>Experimental.....</b>	<b>114</b>
<b>6.3</b>	<b>Results .....</b>	<b>115</b>
<b>6.4</b>	<b>Quantification of AI and surfactant ratio on a deposit.....</b>	<b>130</b>
<b>6.5</b>	<b>Summary .....</b>	<b>133</b>
<b>7.</b>	<b><i>Franz Diffusion Cell: Penetration of Tebuconazole over a cuticular membrane (Clivia Miniata Regel).....</i></b>	<b><i>134</i></b>
<b>7.1</b>	<b>Introduction .....</b>	<b>134</b>
<b>7.2</b>	<b>Experimental.....</b>	<b>137</b>
<b>7.3</b>	<b>Results .....</b>	<b>141</b>

7.3.1	Infinite dose experiments .....	141
7.3.2	Spray application experiments.....	148
<b>7.4</b>	<b>Summary .....</b>	<b>151</b>
<b>8.</b>	<b><i>Concluding remarks</i> .....</b>	<b>153</b>
<b>9.</b>	<b><i>References</i> .....</b>	<b>156</b>

## VI. Symbols list

In order of appearance and units used in this thesis:

$W_{\text{coh}}$	work of cohesion, $\text{mN m}^{-1}$
$m_{\text{surf}}$	surfactant concentration, $\text{g L}^{-1}$
$R$	universal molar gas constant, $\text{J mol}^{-1} \text{K}^{-1}$
$T$	temperature, $\text{K}$
$A_{\text{m}}$	area per molecule, $\text{\AA}^2$
$N_{\text{A}}$	Avogadro's constant, $\text{mol}^{-1}$
$k_{\text{B}}$	Boltzmann constant, $\text{kg m}^2 \text{s}^{-2} \text{K}^{-1}$
$X'_m$	activity of the surfactant in micelles
$X_m$	mole fraction of surfactant in a micelle of aggregation number $m$
$f_1$	activity coefficient of the surfactant in micelles
$J_i$	evaporative flux, $\text{kg m}^{-2} \text{s}^{-1}$
$D_i$	vapour diffusion coefficient in the ambient atmosphere, $\text{m}^2 \text{s}^{-1}$
$c_i$	concentration, $\text{mol L}^{-1}$
$a_i$	activity of component $i$
$F$	flow, $\text{mol s}^{-2}$
$A$	area, $\text{m}^2$
$\nabla C$	concentration gradient across the cuticle, $\text{mol L}^{-1}$
$P$	permeance, $\text{m s}^{-1}$
$t_e$	lag time, $\text{s}$
$L$	cuticle thickness, $\mu\text{m}$
$D_{\text{m}}$	diffusion coefficient in homogenous membranes, $\text{m}^2 \text{s}^{-1}$
$t$	time, $\text{s}$

$R_0$	initial contact radius of droplet, m
$R(t)$	contact radius of droplet at time $t$ , m
$B_o$	Bond number
$g$	gravitational acceleration, $m\ s^{-2}$
$h_0$	initial height of the droplet, m
$Ca$	capillary number
$\bar{u}_r$	average radial velocity induced by droplet evaporation, $m\ s^{-1}$
$r$	radial coordinate
$z$	axial coordinate
$h(r,t)$	local height, m
$J(r,t)$	local evaporation flux, $kg\ m^{-2}\ s^{-1}$
$S$	surface of a droplet
$V$	volume of droplet, $m^3$
$D_w$	vapour diffusion coefficient of water in air, $m\ s^{-1}$
$t_k$	time for the kinetic process, s
$r$	radial distance from the centre of the droplet, m
$m$	average rate of evaporative mass transfer, $kg\ m^{-1}\ s^{-1}$
$D_{vap}$	vapour diffusion coefficient at room temperature, $m\ s^{-2}$
$M$	molecular molar mass, $kg\ mol^{-1}$
$J_{ave}$	average evaporative mass loss per unit area, $kg\ cm^{-2}\ s^{-1}$
$\Delta H_{vap}$	heat of vaporization per unit mass of liquid, $J\ mol^{-1}$
$k_L$	thermal conductivity of the liquid, $Wm^{-1}\ K^{-1}$
$\nabla T$	temperature gradient from the bottom to the top of the droplet, K
$x$	tangential coordinate
$n$	normal coordinate
$u$	tangential component of the fluid velocity at the liquid-vapour interface

$C_{\text{mon}}$	free surfactant concentration, $\text{g L}^{-1}$
$C_{\text{T}}$	total surfactant concentration, $\text{g L}^{-1}$
$C_{\text{mic}}$	surfactant concentration in micelles, $\text{g L}^{-1}$
$Re$	Reynolds number
$D_{\text{f}}$	diameter of the droplet in flight, m
$D_{\text{max}}$	maximum diameter, m
$G'$	elastic modulus, Pa
$p$	Laplace pressure, Pa
$r_c$	radius curvature of the surface, m
$D_{\text{fr}}$	distance between fringes, nm
$n$	refractive index
$S_f$	sensitivity factor
$G$	Gibbs energy, J
$H$	enthalpy, J
$S$	entropy, $\text{J K}^{-1}$
$AI_{\text{cumulative}}$	cumulative amount of AI that has passed through the leaf, $\mu\text{g cm}^{-2}$
$V_{\text{s}}$	sampling volume, L
$V_{\text{d}}$	volume of donor compartment, L
$a$	cuticle area, $\text{cm}^2$
$P$	dipole moment, C m
$E$	external electric field, $\text{N C}^{-1}$
$\sigma_{\text{lv}}$	liquid–vapour interfacial tension, $\text{mN m}^{-1}$
$\sigma_{\text{sv}}$	solid–vapour interfacial tensions, $\text{mN m}^{-1}$
$\sigma_{\text{sl}}$	solid–liquid interfacial tensions, $\text{mN m}^{-1}$
$\Gamma_{\text{surf}}$	surface excess of surfactant, $\text{mol m}^{-2}$
$\mu$	chemical potential, $\text{J mol}^{-1}$

$\mu_m^e$	chemical potential of m in the standard state, J mol <sup>-1</sup>
$\theta$	contact angle, degrees
$\theta_r$	receding contact angle, degrees
$\theta_a$	advancing contact angle, degrees
$\rho$	density, kg m <sup>-3</sup>
$\sigma$	surface tension of fluid, mN m <sup>-1</sup>
$\eta$	fluid viscosity, Pa s
$\rho_\infty$	ambient vapour density, kg m <sup>-3</sup>
$\rho_{vap}$	saturation vapour density at the $T$ of the droplet surface, kg m <sup>-3</sup>
$p_{vap}$	vapour pressure, Pa
$\lambda(\theta)$	parameter reflecting the uniformity of evaporation flux along the drop surface
$\lambda$	wavelength, nm
$\nu_s$	frequency of the scattered light, Hz
$\delta_{obsd}$	observed chemical shift
$\delta_{mon}$	free monomer's chemical shift
$\delta_{mic}$	micelles' chemical shift
$v_d$	drop impact velocity, m s <sup>-1</sup>
$\varepsilon$	ratio of the elastic modulus to the capillary pressure



## VII. Abbreviations

Surf1	2-propylheptanol ethoxylate
Surf2	coco amidopropyldimethylamine
AI	active ingredient
<sup>1</sup> H-NMR	proton nuclear magnetic resonance
CRE	coffee-ring effect
SEM	scanning electron microscope
EDS	energy-dispersive X-ray Spectroscopy
SOFP	simulation of foliar penetration
<i>RH</i>	relative humidity
CM	cuticular membrane
log <i>P</i>	partition coefficient
EO	ethylene oxide
log <i>K<sub>o/w</sub></i>	n-Octanol/Water partition coefficient
CMC	critical micelle concentration
HLB	hydrophilic/lipophilic balance
DOD	drop-on-demand
UDOS	unilateral desorption of the outer surface
log <i>K<sub>c/w</sub></i>	cuticle/water partition coefficient
CL	contact line
DNA	deoxyribonucleic acid
RNA	ribonucleic acid
CAH	contact angle hysteresis
CCR	constant contact radius mode
CCA	constant contact angle mode

OTS	octadecyltrichlorosilane
CDO	chloro(dimethyl)octylsilane
HMDS	hexamethyldisilazane
PS	polystyrene
SC	suspension concentrate
LED	light-emitting diode
NA	numerical aperture
WD	working distance
PID	proportional–integral–derivative
fps	frames per seconds
DOSY	diffusion-ordered NMR spectroscopy
LC-MS	liquid chromatography-mass spectroscopy
ESI	electrospray ionization
APCI	atmospheric pressure chemical ionization
MRM	multiple reaction monitoring
CID	Collision Induced Dissociation
TBP	tunable bandpass filter
BP	bandpass filter
DMSO	dimethyl sulfoxide
IS	internal standard
TQD	triple quadrupole
TFA	trifluoroacetic acid
HAc	acetic acid

# Chapter 1

## 1. Introduction

### 1.1 Challenges of crop protection application

Despite the negative perception of the public, pesticides are still going to be used for many decades to ensure the food supply for the ever-growing world population. The simple reason is that alternative methods for plant protection are either inefficient or too costly for farmers<sup>2</sup>. It is estimated that of the total amount of pesticides applied for weed and pest control, only a very small part (less than 0.1%) actually reaches the sites of action<sup>2</sup>, with the larger proportion being lost via spray drift, off-target deposition, run-off, photodegradation and so on. This inefficiency not only increases the cost of crop protection but also causes serious environmental pollution.

A crop protection product includes the active ingredient (AI) which is the chemical substance that is biologically active, also known as biocide<sup>3</sup>. Depending on the target organisms being in general either weeds, pests or plant pathogens, AIs are classified as herbicides, insecticides or fungicides<sup>4</sup>. These biocidal compounds have different modes of action when applied to the field<sup>2</sup>.

By improving the efficiency, the dosage of AI can be reduced. One of the most important ways to improve the efficacy of pesticides and to minimize the impact on off-target organisms is through increasing the penetration of AIs into plant foliage. As foliar uptake is important for the efficacy of systemic pesticides, then diffusion into plant tissues is a prerequisite for their activity. Foliar uptake of pesticides<sup>5</sup> is a complex process, depending on leaf surfaces, physico-chemical properties of the chemicals, types and concentration of the additives and environmental conditions.

For systemic pesticides<sup>6</sup>, the cuticle of a leaf is an almost impenetrable barrier for the AI so adjuvants have to be added to the solution to enhance the passage of the AI through the cuticle. It is believed that to be effective, AI and adjuvant have to end up in the same position when the droplet dries out on the surface of the leaf, though firm experimental evidence is lacking. This project is concerned with the co-localization of agrochemical adjuvants and AIs on a leaf deposit and the effect of the distribution of molecules on the uptake of the AI by the leaf. Another purpose of this thesis is to get a better understating of the foliar uptake process to lead to a more rational use of pesticides and minimize their negative impact on the environment.

This chapter is organised as follows: first, the complex process of spraying a fluid onto a surface is mentioned (Section 1.2). Second, the characteristic of the leaf surface, the different routes for pesticide penetration and the effect of temperature and relative humidity (*RH*) on foliar pesticide uptake is given (Section 1.3). Third, physico-chemical properties of surfactants, the thermodynamics of micellization and their mode of action in enhancing pesticide are shown (Section 1.4). Fourth, an explanation about how droplets are generated until they reached the model surface is explained (Section 1.5). Fifth, how the foliar penetration process occurs across plant cuticles is described (Section 1.6). At the end of this chapter, the model surface and the AI properties are mentioned (Section 1.7 and 1.8).

Chapter 2 describes the main theoretical concepts relevant to my thesis like the evaporation of sessile droplets due to their geometry and wettability and the causes of particle transport within the droplet (coffee-ring effect and Marangoni flows). Chapter 3 summarises the experimental methods including the instrumentation and procedures used in this thesis. Chapter 4 describes the physico-chemical characterisation of the formulations used in this thesis using techniques such as surface tensiometry and NMR. Chapter 5 shows the different modes of evaporation of agrochemical droplets depending on the substrate and the final residual pattern. Also, some strategies for the modification of the final deposit are tested. Chapter 6 combines scanning electron microscopy (SEM) and energy dispersive X-ray (EDS) spectroscopy with Raman spectroscopy in order to confirm if there is or not co-localization between the surfactant and AI. Chapter 7 combines studies using Franz cell diffusion: i) infinite

dose and ii) simulation of foliar penetration, in order to study the penetration of the AI through the cuticle of the leaf.

## **1.2 Aerial spray on plants**

Spraying a fluid onto a surface is a complex process where a multitude of different factors need to be considered. The first obstacle one encounters during spray treatments occurs once a fluid leaves the nozzle. This step is made difficult by the fact that wind and air currents can entrain the droplets and cause them to drift off course on their way to the plant surface. This phenomenon is known as spray drift, and it represents a major problem, as pesticides in the formulation can be deposited in undesirable areas with serious consequences, such as water contamination and health risks for animal and people. The droplets most prone to spray drift are usually small in size, less than 200  $\mu\text{m}$  in diameter. Hence, one might think that spray drift can be easily solved by increasing the droplet size, however, this remedy introduces another problem when these drops reach the plant surface. Upon impact onto the plant surface aqueous drops have a tendency to splash or bounce and land on the ground. This effect is due to the wax-like layer of a plant leaf, producing a non-wetting interface that repels water. This repulsion is both inefficient and hazardous since crop treatment chemicals in the formulation will eventually contaminate the soil and water supplies. Hence, we see that there is a certain antagonistic effect concerning droplet size characteristics; large drops help control spray drift but promote droplet rebound.

The last step concerning the spray treatment of plants, addresses retention and adhesion of the active molecules onto the surface. After a drop successfully lands and stays on the surface, it is desirable for it not to be washed off during the next rain shower. This latter effect is termed washing resistance.

## **1.3 Leaf surface characteristic, routes for pesticide penetration and environmental factors affecting foliar-applied herbicide uptake**

### 1.3.1 Leaf surface characteristic

Before reviewing how surfactants enhance movement of herbicides across the cuticle it is important to understand the overall composition of plant cuticles.

- *Epicuticular wax*

Epicuticular wax (probably the rate-limiting barrier to herbicide absorption) covers the leaf surface and its hydrophobic nature makes it difficult to obtain good wetting of leaf surfaces with aqueous sprays. Epicuticular wax consists of a variety of long-chain even-numbered ( $C_{22}$ – $C_{24}$ ) primary alcohols, acetates, aldehydes, fatty acids, and their hydroxyl- and oxi- derivatives, as well as odd-carbon-numbered ( $C_{17}$ – $C_{35}$ ) hydrocarbons, secondary alcohols, ketones, and  $\beta$ -diketoles.

The chemical or physical properties of the wax appear to be more important than thickness in restricting penetration. The epicuticular wax present on the leaf surface has two main forms, crystalline and amorphous. The crystalline wax is undoubtedly an obstacle for spray retention and an intimate contact between pesticide droplets and leaf surface, but it does not seem to be a formidable barrier for pesticide uptake.

Deposition, distribution and retention of spray droplets are affected by the extent of coverage and chemical composition of the epicuticular wax and by leaf surface microroughness. High levels of microroughness may inhibit herbicide penetration (caused by epicuticular waxes, cell surface contours, leaf venation and trichomes). Trichomes are structures on a plant's leaves that look like tiny hairs sticking out from the surface of the leaf.

- *Cuticle*

All aerial surfaces of plants are covered by the cuticle. The waxy sheet of cuticle not only prevents water loss, but also functions in defence by forming a barrier that resists

physical damage and microbial invasion. The plant cuticle is a thin continuous layer (< 0.1–10  $\mu\text{m}$ ) of predominantly lipid material synthesized by the epidermal cells and deposited on their outer walls<sup>7</sup>. The cuticle consists of a polymer matrix (cutin), polysaccharides and associated solvent-soluble lipids (cuticular waxes). Cutin is a three-dimensional polymer of mostly C<sub>16</sub> and C<sub>18</sub> hydroxy fatty acids crosslinked by ester and other bonds. Cutin is present as both amorphous and lamellar forms. Cuticular wax is a general term for complex mixtures of a homologous series of long-chain aliphatics like alkanes, alcohols, aldehydes, fatty acids, and esters with the addition of varying proportions of cyclic compounds like pentacyclic triterpenoids and hydroxycinnamic acid derivatives. For waxes, the chain length ranges from 20 to 36 carbons and they are present in crystalline and amorphous forms, with leaves having a dominant crystalline wax form being more difficult to wet<sup>8</sup>. Whereas the overall chemical composition of the cuticle is lipophilic, it has both hydrophilic and lipophilic components and both lipophilic and hydrophilic compounds can diffuse through it. It was postulated<sup>9</sup> that lipophilic and hydrophilic chemicals follow distinct pathways, i.e., polar (aqueous pores) and apolar (cutin matrix and wax) routes.

A third component of the cuticle is the pectin (primarily polymers of galacturonic acid) and it is located at the cutin/cell wall interface or dispersed within the cutin layer. Pectin is very hydrophilic and, like cutin, provides pathways for water-soluble herbicides when hydrated.

- *Stomata and guard cells*

Stomata are tiny pores in a plant leaf surrounded by a pair of guard cells that regulate their opening and closure, and serve as the site for gas exchange.

The stomatal uptake of pesticides varies greatly with plant species (e.g. very limited on grass species). Guard cells have been found to be an easy entrance for xenobiotics, a chemical compound foreign to a given biological system, especially for hydrophilic compounds. However, the percentage uptake of xenobiotics via guard cells is very small (< 3%) compared with the total dose applied on the leaf surface.

### 1.3.2 Pathways of diffusion across plant cuticles

The mechanism of foliar uptake is still poorly understood. There may be separate routes or pathways through the cuticle for different compounds, i.e. a lipophilic and an aqueous pathway. In general, neutral compounds of intermediate lipophilicity are taken up faster than charged ones.

- The lipophilic path of diffusion

Many synthetic compounds (pesticides, herbicides and other xenobiotics) are non-ionic and many of these molecules are lipophilic. Lipophilic compounds must diffuse across lipophilic wax and cutin domains of the cuticle<sup>10</sup>. The permeability of the cuticle to water and to lipophilic molecules increases with mobility (diffusion coefficients) and solubility (partition coefficients) of these compounds within the transport-limiting barrier of the cuticles. Significantly less is known about the permeability of the cuticle to ionic compounds.

The cuticular pathway for uptake into or release from the leaf is the exclusive one for scarcely volatile to non-volatile solutes contained in liquid or solid deposits on the leaf surface or releasing from the interior of the leaf. Compounds with higher volatility, in principle, can take two parallel paths to and from the interior of a leaf as long as the stomata are open. The pathway preferred depends on the lipophilicity of the compound and its volatility. With stomata closed or absent, volatiles have to take the cuticular pathway.

Transport of material across the plant/atmosphere interface arises from non-equilibrium conditions: the chemical potentials of water, solutes or gaseous compounds differ between the interior of the leaf and the outside. This, for instance, leads to the loss of water vapour (transpiration) or to the uptake of solutes (e.g. foliar penetration of pesticides). In any case, the important fact is to know how long it takes until biologically relevant amounts of material are lost or taken up. The decisive function of the plant cuticle is kinetic control of uptake and loss.



- The polar path of diffusion

In contrast to large lipophilic molecules and small polar but still uncharged molecules like water, ionic compounds (mostly  $\text{Ca}^{+2}$  salts) have only recently been extensively analysed for cuticular permeability<sup>11,12,13,14,15</sup>. Schonherr<sup>19</sup> showed convincingly that charged molecules can diffuse across isolated cuticles. Since charged molecules carry hydration shells<sup>16</sup>, which cannot be shed, they will not be soluble in the lipophilic cutin and wax domains of the cuticles.

This very different behaviour of lipophilic and ionic compounds strongly suggests that these two groups of compounds of physico-chemically very different nature penetrate plant cuticles via alternative paths. It must be concluded that ionic compounds use aqueous polar paths of diffusion, whereas lipophilic molecules diffuse along the lipophilic wax and cutin domains. The nature of the lipophilic paths across cuticles must be formed by the lipophilic cutin and wax domains.

### 1.3.3 Environmental factors affecting foliar-applied herbicide uptake

Among the many environmental factors that can affect herbicide uptake, two of the most important are temperature and humidity, with optimal uptake being favoured by warm, humid conditions<sup>17</sup>. Temperature can affect herbicide uptake by changing the viscosity of cuticle waxes, the rate of diffusion and in conjunction with humidity, cuticle hydration<sup>18</sup>. While higher temperatures increase diffusion of herbicides across the cuticle, increased efficacy is not always observed<sup>19</sup>. This may be due to reduced herbicide availability caused by rapid drying of droplets to solid deposits in warm conditions. Price<sup>22</sup> suggested that effective herbicide uptake at high temperature requires high humidity to prevent rapid droplet drying.

In contrast to the direct physical effects that temperature has on cuticular components, the effects of humidity on herbicide uptake are usually related to its impact on cuticle hydration and the rate of herbicide-droplet drying<sup>21,22</sup>. Several researchers who have investigated the impact of both temperature and humidity found that humidity has a

greater influence on herbicide efficacy than temperature<sup>20,21</sup>. However, humidity and temperature interactions can vary from species to species.

While it is clear that environmental variables have a profound effect on the uptake and efficacy of foliar-applied herbicides, there is relatively little information on the exact mechanisms involved in the influence of humidity and temperature on herbicide and surfactant performance<sup>22</sup>. However, since it is clear that both temperature and humidity have an impact on droplet drying, a measure of air moisture that takes temperature into account is more appropriate.

## 1.4 Surfactants

The term '*surfactant*' is derived from '*surface active agent*' and should not mixed-up with the term '*adjuvant*', since adjuvants are not limited to surfactants<sup>23</sup>.

### 1.4.1 Physico-chemical properties of surfactants

Surfactants are defined by their amphiphilic character, combining a nonpolar lipophilic and a polar hydrophilic portion in one molecule, which is the most important requirement on physiochemical actions<sup>24</sup>. The lipophilic portion usually consists of an elongated alkyl chain and is often just called the 'tail'. The polar hydrophilic part is called the 'head'<sup>25</sup>. Surfactants are efficient additives in enhancing pesticide efficacy.

Surfactants are classified as follows:

- i) *Non-ionic surfactants* have no electrical charge. The hydrophobic group is balanced by such non-ionized hydrophilic groups as polymerized ethylene oxide (EO), polyhydric alcohols, esters of polyhydric alcohols or polyether alcohols. They are generally compatible with most pesticides and they are most commonly used because of their universal fit as they are chemically inert because of their lack of ionization. They are also poor foamers, which is important if you are mixing a concentrated formulation with water in a tank. The

main functions are to reduce surface tension, improve spreading and sticking.

- ii) *Anionic surfactants* have a hydrophobic group (paraffinic chain, alkyl-substituted benzene or naphthalene ring) balanced with a negatively charged hydrophilic group (carboxyl, sulphate, sulphonate or phosphate). Anionic surfactants are more specialized and sometimes used as dispersants or compatibility agents.
- iii) *Cationic surfactants* are compounds having similar hydrophobic groups as listed for anionic surfactants, but balanced with a positively charged hydrophilic group (quaternary ammonium). Cationic surfactants are used less frequently than non-ionic surfactants.
- iv) *Ampholytic surfactants* are compounds having a molecular arrangement of hydrophilic groups with the potential to become cationic in an acidic medium and anionic in a basic medium.
- v) *Zwitterionic surfactants* are compounds with both cationic and anionic groups attached to the same molecule. The cationic part is based on primary, secondary, or tertiary amines or quaternary ammonium cations. The anionic part can be more variable and include sulfonates (for example, betaines).
- vi) The *organosilicone-based materials* are another group of surfactants more recently introduced. These surfactants are used in place of or in addition to more traditional non-ionic surfactants. They have strong reduction of surface tension, improve absorption and rainfastness, and facilitate stomatal and cuticular uptake.

Surfactants exhibit a number of properties in solution as a consequence of the hydrophobicity of their tail group. They form aggregates in solution, termed micelles. Also, they adsorb to interfaces or surfaces. The preferred orientation and structure of the surfactant at the interface is determined by the nature of the interface: at

hydrophobic interfaces they attach with the hydrophobic chain facing the interface, either as a monolayer or as a hemi-micelle aggregate; at hydrophilic interfaces they absorb either as bilayers or as separate aggregated structures (admicelles) with the surfactants immediately adjacent to the interface orientated with their head group facing the interface. The air-water surface acts like a hydrophobic interface.

From an energetic point of view, molecules have a lower energy in the interior of the volume phase or bulk phase rather than at the surface, because a molecule interacts with fewer molecules at the surface than in the bulk phase. In contrast, due to the special amphiphilic structure of surfactants, their presence at the surface is more beneficial, and therefore the surface tension can be efficiently reduced already when only a small amount of surfactants is present. Micelles form when the chemical potential of a monomer in solution and in a micelle are equal. Micelles are diverse clusters of single surfactant molecules that structure in a spherical, cylindrical, lamellar or vesicular shape and have the ability to incorporate substances which are not soluble in the bulk liquid<sup>26</sup>. There is a characteristic concentration, depending on the nature of the surfactant, at which micelles start to build. This typical transition concentration is described as the ‘critical micelle concentration’ (CMC), which is an important individual value for each surfactant. This action of surfactants as micelle-forming substances is of special importance for the application as detergency and solubilisation aids.

The most important and fundamental physiochemical property of surfactants is the ability to lower interfacial tension between two phases<sup>27</sup> (Figure 1.1).

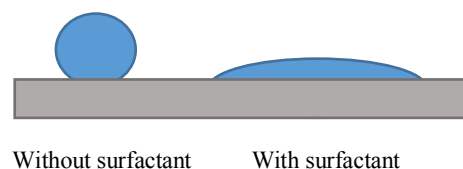


Figure 1.1: Effect of the addition of a surfactant on the spreading of a sessile droplet.

The interfacial tension changes with concentration of surfactant. Interfacial tension is the free energy change associated with increasing the surface area of a medium by unit

area, which is the equivalent to the minimum work of separating two half unit areas from contact to infinity

$$\sigma_{lv} = -\frac{1}{2}W_{coh} \quad \text{Eq. 1.1}$$

where  $W_{coh}$  is the work of cohesion. For the liquid-vapour interface the conventional SI units for the interfacial tension,  $\sigma_{lv}$  are  $\text{mN m}^{-1}$ .

At very low concentrations of surfactant, the interfacial tension of the solution is dominated by the interfacial tension of the bulk liquid. As the concentration of surfactant increases, more becomes adsorbed onto the surface and the interfacial tension decreases with concentration of surfactant. The interfacial tension stops decreasing at the CMC, above the CMC the interfacial tension remains constant and the extra surfactant forms micelles. Below the CMC, the tangent of the curve of interfacial tension against the natural log of concentration  $\ln(m_{surf})$  can be used to calculate the Gibbs surface excess concentration. The surface excess remains constant in the region where interfacial tension is linear with log concentration and the changes in interfacial tension are caused by the change in surfactant activity in the bulk solution<sup>28</sup>. The surface excess is calculated using the Gibbs equation,

$$\Gamma_{surf} = \frac{1}{nRT} \left( \frac{d\sigma}{d\ln(m_{surf}/m^o)} \right) \quad \text{Eq. 1.2}$$

where  $m_{surf}$  is the concentration of surfactant,  $m^o$  is  $m_{surf}$  in the standard state (1 g/L) and  $n$  is 1 for non-ionic and zwitterionic surfactants and  $n$  is 2 for anionic surfactants in the absence of salt. From the surface excess, the minimum area occupied by the surfactant absorbed at the interface ( $A_m$ ) can be calculated using

$$A_m = \frac{1}{\Gamma N_A} \quad \text{Eq. 1.3}$$

It is common for a hydrophobic solute to decrease the CMC. CMC calculations can be used to determine the concentration of surfactant in micelles and understand the amount of surfactant available to solubilize the active ingredient, Tebuconazole.

## 1.4.2 Thermodynamics of micellization

Micelles are structures in equilibrium with surfactant monomers. Accordingly, the free energies or chemical potentials of all the aggregates must be equal and can thus be expressed as<sup>29</sup>,

$$\mu = \mu_1^o + k_B T \ln X_1' = \mu_2^o + \frac{1}{2} k_B T \ln \frac{X_2'}{2} = \mu_3^o + \frac{1}{3} k_B T \ln \frac{X_3'}{3} = \dots \quad \text{Eq. 1.4}$$

where  $k_B$  is the Boltzmann constant,  $T$  is the temperature of the system,  $\mu_m^o$  is the standard chemical potential of a monomer in a micelle aggregation number  $m$  and  $X_m'$  is the activity of the micelles with aggregation number  $m$  which can be expressed as  $X_m' = X_m f_1$  where  $X_m$  is the mole fraction of surfactants and  $f_1$  is the activity coefficient of the micelles. Eq. 1.4 can be simplified to,

$$\mu_m = \mu_m^o + \frac{k_B T}{m} \ln \frac{X_m'}{m} = \text{constant} \quad \text{Eq. 1.5}$$

The first term in Eq. 1.5 represents the free energy of a surfactant in a micelle and the free energy of its interactions with other surfactants in the micelle. The second term is a statistical contribution to the chemical potential arising from the entropy of mixing a micelle with water and has the general form  $k_B T \ln(X_m/m)$ . The  $1/m$  factor outside the logarithm converts this to the contribution per monomer.

If the micelle concentration is sufficiently low it is possible to neglect non-ideality of micelle–micelle interactions so that  $f_m = 1$  and  $X_m' = X_m$  for  $m > 1$ . However, since the concentration of monomers is much higher it is not possible to neglect the possibility of non-ideality of monomer–monomer interactions so that a micellar system can be described by<sup>36</sup>,

$$\mu_m^o - \mu_1^o = k_B T \ln X_1 + k_B T \ln f_1 - \frac{k_B T}{m} \ln \frac{X_m}{m} \quad \text{Eq. 1.6}$$

where  $f_1$  is the monomer activity coefficient and has been separated from  $X_1'$  for convenience.

Eq. 1.6 is a fundamental equation describing a surfactant system and can also be derived using the mass action model which is another popular approach to the thermodynamic analysis of micellization. In this method micelles and monomers are assumed to be in association–dissociation equilibrium as illustrated in Figure 1.2.

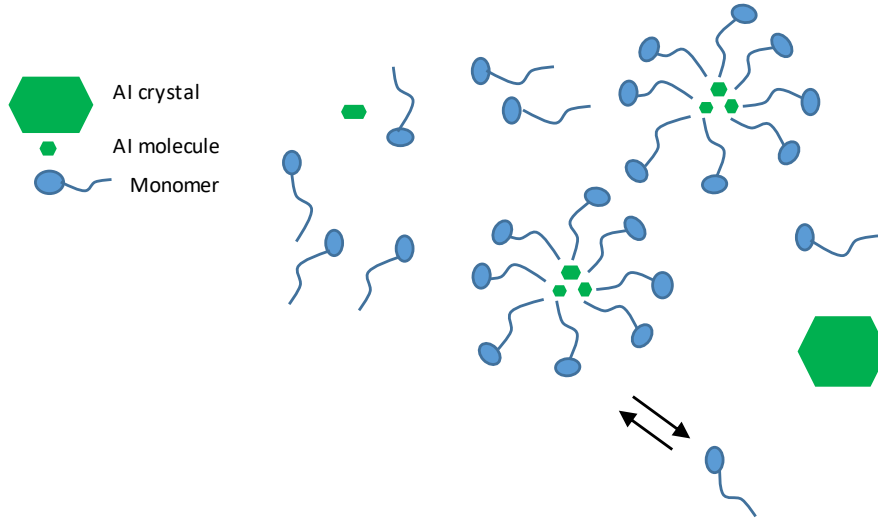


Figure 1.2: Cartoon illustration of mass action model. Monomers are in dynamic equilibrium with micelles of all sizes.

With some simple manipulation Eq. 1.6 can be expressed as

$$X_m = m \left[ X_1' e^{-\left[ \frac{(\mu_1^0 - \mu_m^0)}{kT} \right]} \right]^m \quad \text{Eq. 1.7}$$

Another important feature of Eq. 1.7 is the relation to the CMC. If the concentration of surfactant is low enough that

$$X_1 e^{-\left[ \frac{(\mu_1^0 - \mu_m^0)}{kT} \right]} \ll 1, \quad X_1 > X_2 > X_3 > \dots \quad \text{Eq. 1.8}$$

meaning that most surfactant molecules exist as individual monomers. However, since  $X_m$  cannot exceed unity it is clear from Eq. 1.7 that when  $X_1$  approaches  $e^{\left[\frac{(\mu_m^0 - \mu_1^0)}{kT}\right]}$  it can no longer increase. Thus, at this critical concentration further addition of surfactant must lead to the formation of aggregates. This concentration, therefore, corresponds to the CMC and can be expressed as,

$$CMC = e^{\left[\frac{(\mu_m^0 - \mu_1^0)}{kT}\right]} \quad \text{Eq. 1.9}$$

### 1.4.3 Micellar solubilisation: Basic thermodynamic principles.

A useful property of micelles is their ability to solubilise hydrophobic substances while remaining thermodynamically stable in aqueous solution. The solubilisation of hydrophobic and hydrophilic substances in micelles arises due to the presence of different regions with varying chemical nature within the micelle. In the standard core-shell micelle, for example, the core, shell and palisade layer all have different characteristics. The core consists exclusively of hydrocarbon tails and is thus extremely hydrophobic. The shell, on the other hand, contains head groups and water, making it hydrophilic. The palisade layer at the interface between the core and shell has properties that depend on the specific structures of the head and tail. Consequently, these three main domains are attractive to non-polar, polar and amphiphilic substances, respectively.

The size and shape of micelles depend on the specific interactions of the head and tail groups with the solvent and one another. This means that the influence of a solubilisate on the physical properties of a micelle will depend on how it influences these interactions. In general, solubilisates do not influence the interactions between the surfactant tail and water, but their presence in the micelle does often affect interactions between surfactant head groups<sup>30</sup>. The more hydrophobic the substance is the deeper it penetrates into micelles. The findings of Fischer et al<sup>31</sup> were broadly consistent with this perception. In their study, the hydrophobicity was quantified using the octanol-water partition coefficient,  $\log P_{ow}$ , where higher  $\log P_{ow}$  coefficients represent more



hydrophobic molecules. It was found that when  $\log P_{ow} > 3.5$  the molecules fully solubilised in the micelles and were located in the core. For intermediate  $\log P_{ow}$  value they dissolved in the bulk solvent and the micelles. Those molecules in the micelles were generally in the core but near the palisade layer. For low  $\log P_{ow}$  they were mostly partitioned in the bulk solvent but a small fraction of molecules in the micelles preferred to be in or near the hydrophilic shell. Thus, according to the current theory a location of a solubilisate in a micelle can be determined by its  $\log P_{ow}$ . In this thesis, proton nuclear magnetic resonance ( $^1\text{H-NMR}$ ) was used to study the solubility of a model AI, Tebuconazole, (see Section 1.8), in one of the formulations.

#### 1.4.3.1 Micelles vs Emulsions

The most common commercial Tebuconazole formulations are suspensions or emulsions. The formulation type will depend on the state of the AI. If the AI is in liquid state solubilized in the solvent an emulsion will form upon mixing with water and if the AI is in solid state dispersed in the solvent a suspension will be formed.

Emulsions are not thermodynamically stable systems and will eventually separate into two different phases. Then, these kinds of formulations are often subjected to a wide range of temperatures, meaning that the emulsifier blend has to provide a long life in a fairly wide range of temperatures. How long this will take depends on how well the emulsifiers are stabilizing the system. If phase separation does occur it can lead to recrystallization of AIs which can undermine product efficacy.

Micellar solutions can offer far more favourable properties. Most importantly, they are thermodynamically stable so that the formulations would be less likely to degrade over time and would provide a better application efficacy and more uniform AI dosage. In addition, they can be entirely water based and thus avoid the need for non-polar solvents which can, in turn, reduce adverse impact on environment. In spite of these benefits, there is one major drawback to the use of micelles, that is, they tend to have lower solubilisation capacities than emulsions. Many workers<sup>32,33</sup> have studied ways in which the additive concentration in micellar formulations can be maximised but the AI capacities of emulsions are still far superior to those achievable in micellar formulations.

Two main agrochemical solutions were used in this thesis: i) a non-ionic alkyl ethoxylate surfactant composed of a hydrophobic alkyl chain of length,  $m$ , and a hydrophilic ethoxylate group consisting of  $n$  ethoxylate units  $(-\text{CH}_2\text{CH}_2\text{O}-)_n$  (in this thesis  $m = 10$ ,  $n = 8$ ) and ii) an amidoamine-based surfactant. Both formulations involved the addition of Tebuconazole resulting in a suspension and an emulsion, respectively.

#### 1.4.4 Surfactant concentration in relation to pesticide uptake

As a general rule<sup>39</sup>, pesticide uptake increases with increasing surfactant concentration from 0.01 to 1% (v/v). However, in rare cases, high surfactant concentrations may have detrimental effect on pesticide uptake. This is the case for glyphosate uptake into grass species with organosilicone surfactant, Silwet L-77. When the silicone surfactant was used at a normal concentration range (0.1 to 0.5% (v/v)), glyphosate uptake was reduced compared to control with no surfactants, a phenomenon referred to as antagonism<sup>34</sup>. Interestingly, the same surfactant used at very low concentrations (0.01 and 0.02% (v/v)) gave small spread areas and improved markedly glyphosate uptake<sup>35</sup>.

##### 1.4.4.1 The modes of action of surfactants in enhancing pesticide uptake

By knowing how important the foliar uptake for the plant protection is, an understanding of biodelivery of agrochemical is crucial. An effective biodelivery can be reached exclusively when the application parameters are optimised by choosing the right compound with the exact concentration at the right time of application (environmental conditions). Several AIs are innately biologically inactive and need other substances added to activate them or they have physico-chemical properties making them difficult to apply because of insolubility. Therefore, a crop protection product is only effective if the diverse mixture of auxiliary substances is right.

Surfactants can affect each of the following steps in the uptake process<sup>36,9,37,38</sup>:

- i) Effect on pesticide deposits on the leaf surface: the presence of surfactants in the spray mixture may have multiple functions on the leaf surface, all contributing to the improvement of pesticide uptake. These include: (a) ensuring an intimate contact between the droplets and the leaf surface related

to the reduction of surface tension, especially on waxy species; (b) preventing or delaying crystal formation in the droplet residue; (c) delaying droplet drying through a hygroscopic effect.

Surfactants that maintain herbicides in a soluble form on the leaf surface increase the driving force (concentration gradient) across the cuticle. The mechanism of action of surfactants once inside the cuticle is not well understood.

- ii) Effect on the transcuticular diffusion of pesticides: it has been speculated<sup>9</sup> that surfactants increase the penetration of hydrophilic compounds by hydrating the cuticle, whereas they accelerate the uptake of lipophilic chemicals by increasing the fluidity (or reducing the viscosity) of the cuticular wax. Both hypotheses are largely substantiated by results obtained with isolated cuticles.
- iii) Effect on the permeability of plasma membrane. Although it is difficult to estimate the relative contribution of increasing the permeability of plasma membrane to the overall uptake enhancement provided by surfactants, faster diffusion of the solute into epidermal cells should help to maintain a higher concentration gradient between the cuticle and the sub-cuticular apoplast, which in turn, accelerates the overall uptake.

In order to associate surfactant mechanism of action with surfactant type, one of the most important measures assigned is hydrophilic/lipophilic balance (HLB), as described by Griffin in 1949<sup>39</sup> and 1954<sup>40</sup>. HLB is a number ranging from 1 to 20 and it is used to characterize the solubility of a substance in the CM. For non-ionic surfactants this value is approximated by the weight percent of the total weight of the surfactant that is hydrophilic divided by 5. For ionic surfactants, HBL is less straightforward and is usually determined experimentally. Lipophilic surfactants have HBL values of 8 and below. Surfactants with HLB numbers between 9 and 11 are intermediate, and those with HLB numbers above 11 are hydrophilic<sup>41</sup>. Therefore, low HLB surfactants are more lipophilic and more able to diffuse into the lipophilic cuticle than high-HLB surfactants that are less lipophilic.

Even though surfactants are the most used adjuvant type in agrochemical applications, and generally the most efficient additives in enhancing pesticide efficacy, there are other ones such as crop oil concentrate, vegetable oil concentrate, nitrogen fertilizer, etc. The surfactants mostly used in this work are shown in Section 4.2.

## **1.5 From the nozzle to the model surface**

The process of generating and controlling small droplets of constant size is necessary to achieve a reproducible method to print different solutions because of their strong influence on the droplet impact behavior on the surfaces. Droplet characteristics will depend on nozzle type, orifice size<sup>42</sup>, liquid properties<sup>43</sup>, etc. The combination with an imaging technique allows a reliable evaluation of droplet characteristics and behavior.

Droplet generation can be accomplished by making one short duration fluid jet which condenses into a single droplet of desired diameter (Droplet-On-Demand (DOD) mode) or by breaking up a continuous fluid jet into uniform sized droplets with a source of acoustic energy (continuous mode) as described in detail by Lee<sup>44</sup>. The first mode, DOD mode, has been used in many technical, industrial and scientific applications because only a small amount of fluid is needed to form droplets e.g.: inkjet printing<sup>45</sup>, calibration of particle sizing instruments<sup>46,47</sup>, one-drop-fill technology<sup>48</sup>, biotechnology and medicine<sup>49</sup>. Continuous mode has also been used in applications like fabrication of metal parts<sup>50</sup> and inkjet printing<sup>51</sup>.

DOD technique was used in this thesis where the fluid was ejected through the nozzle using a piezoelectric device which expands or contracts in response to an applied electric field. Droplet formation in DOD-mode requires some conditions in order to generate uniform and single droplets in a repeatable way<sup>53</sup>. Air bubbles are detrimental to the droplet generation and should be removed. To prevent fluid from dripping out and air bubbles from entering the system via the nozzle orifice, the fluid pressure should be controlled until a meniscus is just visible on the tip of the nozzle. This can be achieved by changing the liquid column height in the fluid reservoir. The used to

make the transducer work in a piezoelectric DOD print head can be varied in order to modify the size of the drops being ejected (Figure 1.3)<sup>52</sup>.

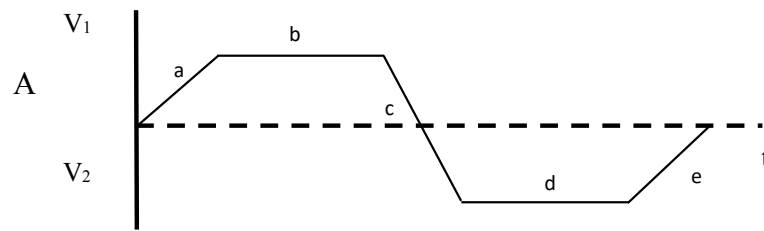


Figure 1.3: Example profile of a typical waveform used for droplet emission in this thesis (amplitude (A) over time (t)). Typical time periods used for water droplets were a) a rise time of 13  $\mu\text{s}$ , b) a dwell time of 29  $\mu\text{s}$ , c) a fall time of 13  $\mu\text{s}$ , d) an echo time of 28  $\mu\text{s}$ , and e) a final rise time of 13  $\mu\text{s}$ .

In general, an increase of both pulse widths (rise time and echo time) tends to increase of the droplet diameter. This effect is more pronounced for larger nozzles. Also, increasing the nozzle orifice increases the droplet diameter. The smaller the nozzle orifice size, the more difficult it is to produce droplets. This comes from the fact that if the pressure (pulse width and the voltage amplitude) is not high enough to overcome surface tension, a droplet is not ejected. Laplace pressure is inversely proportional to the radius of the orifice, so a larger pressure pulse is needed to eject the drop. By selecting the size nozzle and pulse width values one could generate a realistic size range for real pesticide sprays.

The typical drop sizes in DOD are between 10 and 100  $\mu\text{m}$  with frequencies of the order of tens kHz and velocities of 5–8  $\text{m s}^{-1}$ . The desired diameter in crop sprays is 250  $\mu\text{m}$  and to achieve this size multiple droplets are ejected ending up in the same place on the substrate. The droplet generation time (130 ms) is much shorter than the total evaporation time (16 s), so it can be treated as a single droplet<sup>1</sup>.

On the other hand, in continuous fluid jets (Figure 1.4), the fluid is forced through a nozzle forming a jet which is broken-up into droplets due to a perturbation caused by a vibrating piezoelectric crystal that induces a Plateau-Rayleigh instability. As a result

<sup>1</sup> Data collected for a 1.5nL water droplet on a hydrophobic surface.

of this instability bulges and necks are formed. Drops produced in continuous jetting systems typically have velocities  $> 10$  m/s, with generation frequencies  $> 100$  kHz<sup>53</sup> and a drop sizes around 40–70  $\mu\text{m}$ .

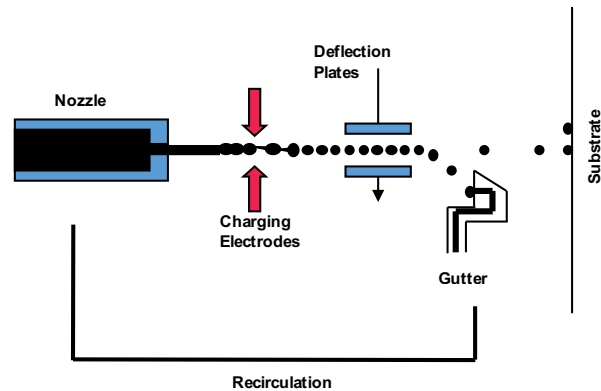


Figure 1.4: Schematic diagram showing the continuous jetting process.

A pressure pump causes a continuous jet from the nozzle. The eventual droplet size is controlled with a piezoelectric actuator. After leaving the nozzle, the droplets are selected to be printed or recycled. The unnecessary droplets are charged by an electrode close to the nozzle and directed toward a recycling gutter by an electric field. Continuous jetting process is mainly used for coding in the packing industry, due to its high speed and reliability.

## 1.6 Diffusion experiments across plant cuticles

In order to study diffusion of an AI *in vivo*, the outermost layer of the leaf, where the main penetration barrier exists, is used as membrane. Three main ways of studying the penetration of CM exists: using a horizontal membrane, using a vertical membrane with a flow of solution through the membrane or using a vertical membrane with a static solution<sup>54</sup>. UDOS (unilateral desorption of the outer surface) is a method using a horizontal membrane where desorption of solute is measured by applying the formulation to the morphological inner surface of the CM. One drawback with this method is that the effect of accelerators or other added compounds on solute permeability is lost<sup>5</sup>.

In this study a method with vertical membrane and static solution will be used first, called Franz cell diffusion<sup>55</sup>. The formulation (1 mL) is applied to the outer surface of the CM and the amount of the AI that penetrates to the backside of the CM is measured. The boundary conditions are kept fixed by having an effectively infinite dose of solution. Second, SOFP (simulation of foliar penetration) is a similar method to the previous one but with the difference that the agrochemical solution is allowed to dry on the surface.

In spray application of pesticides, foliar penetration commences when the spray is retained by the plant surface. Transport through the cuticle is believed to be a diffusion-controlled process. The diffusion process of liquids and gases can be described by Fick's first law,

$$J_i = D_i \frac{dc_i}{dz} \quad \text{Eq. 1.10}$$

The diffusion flux,  $J_i$ , is a measurement on how many molecules that will pass through a defined area during a specific time. The driving force for diffusion is the concentration gradient,  $\frac{dc_i}{dz}$ , where  $c_i$  is the concentration and  $z$  is the position. This law states that molecules travel from areas with high concentrations to other areas with lower concentrations. The diffusion coefficient,  $D_i$ , is the molecular mobility of the diffusing substance. However, when looking at diffusion from a liquid phase through a membrane Eq. 1.10 becomes inadequate. When dealing with diffusion between different phases, for example liquid to solid, simply looking at the concentration gradient as the driving force is not enough. When the saturation level of the liquid inside the solid phase is reached, the concentration in the solid material can still differ from the liquid phase, due to a difference in the local chemical interaction.

Eq 1.10 then suggests that even at equilibrium there should be a driving force of liquid into the solid phase. To solve this problem one needs to change concentration to chemical potential, since the chemical potential in two phases is equal at equilibrium. The driving force for diffusion could then be redefined as the gradient in chemical potential. Rewriting Eq. 1.10 with the chemical potential as the driving force gives the generalized form of Fick's first law, (see Eq. 1.11).

$$J_i = -\frac{D_i}{RT} c_i \frac{d\mu_i}{dz} \quad \text{Eq. 1.11}$$

where  $\mu_i$  is the chemical potential,  $c_i$  is the concentration inside the membrane,  $R$  is the universal gas constant and  $T$  is the absolute temperature. The chemical potential for a neutral substance over a membrane can be defined as in Eq. 1.12.

$$\mu_i = \mu^o + RT \ln a_i \quad \text{Eq. 1.12}$$

Combining Eq. 1.10 and 1.11 into Eq. 1.12, it is apparent that there are different components affecting the diffusion over a membrane. First it's the gradient of thermodynamic activity of the solute over the membrane,  $\frac{da_i}{dz}$ , and second the effects within the membrane, the diffusion coefficient and concentration ( $D_i, c_i$ ).

$$J_i = -\frac{D_i c_i}{RT} \frac{d\mu_i}{dz} = -D_i c_i \frac{d \ln a_i}{dz} = D_i c_i \frac{da_i}{a_i dz} \quad \text{Eq. 1.13}$$

The thermodynamic activity  $a_i$  of an AI in a dilute solution has been defined by Fagerström et al<sup>1</sup> as the actual concentration of the AI divided by the solubility limit for the AI in that solution.

Looking at diffusion through an inert membrane, the main component affecting the flux is the thermodynamic activity. A responding membrane, like the leaf of plants, can interact with the solute which causes the flux to depend on the diffusion coefficient. Fagerström et al<sup>48</sup> looked at the influence of adjuvant on both non-responding (silicon) and responding membranes (the cuticle of leaves). They could show that adding adjuvant strongly enhanced the diffusion, but only for the responding membrane. They concluded that adding adjuvant affect the diffusion by increasing the diffusion coefficient of the diffusing substance.

The difference in solubility between two phases, one lipophilic and one hydrophilic phase, is called the partition coefficient,  $K$  (Eq. 1.14).

$$K = \frac{\text{Concentration in lipophilic phase}}{\text{Concentration in hydrophilic phase}} \quad \text{Eq. 1.14}$$



The CM represents the lipophilic phase and the water solution containing the AI the hydrophilic phase. For practical reasons the octanol/water partition coefficient,  $K_{o/w}$ , can be used instead of the cuticle/water partition coefficient,  $K_{c/w}$ , since measurements of the  $K_{c/w}$  can be hard to obtain. Good relationships between  $K_{c/w}$  and  $K_{o/w}$  have been found for lipophilic substances<sup>56</sup>. Due to the lipoidal nature of the epicuticular wax and the cuticle, foliar uptake tends to increase with increasing lipophilicity of the chemicals. However, it would be wrong to conclude that all lipophilic compounds are taken up faster by plant foliage than hydrophilic ones<sup>7</sup>. For hydrophilic compounds  $K_{o/w}$  cannot be used as predictors for sorption process into CM, as transport across cuticular wax barrier is not relevant.

Although diffusion is a continuous event, for studying and analysing cuticular penetration it may be viewed as consisting of three-component process, namely sorption into, diffusion through and desorption from the cuticle. The solute diffuses through the cuticle and when molecules reach the surface at the cuticle/cell wall interface, they desorb from the cuticle into the aqueous apoplast. Hence, in simplest terms, one can view cuticular penetration as diffusion of a solute from an aqueous donor (spray solution) across the cuticle (membrane) into an aqueous receiver (apoplast). This system exists under field conditions for only a short time depending on spray volume, additives and environmental factors affecting drying time, but the greatest amount of penetration may take place during this time period. Penetration from spray droplets on plant surfaces is a complex process not well understood. The isolated cuticle as a model system is not intended to simulate field application, but is used primarily to develop a better understanding of the mechanisms of cuticular penetration and to identify and quantify factors that affect the penetration process.

## **1.7 Clivia Miniata Regel as a model cuticle**

In order to illustrate the diffusion experiments *Clivia Miniata Regel* was used, since it has thick cuticles that can easily be isolated. Fagerström et al<sup>57</sup> showed that the different isolating techniques did not significantly affect the permeability of the AI. The barrier properties of the CM change with physiological age of the leaf<sup>58</sup>. At the tip

of the leaf the barrier is stronger than at the base, hence, it is recommended<sup>70</sup> that membranes for diffusion experiments are retrieved mid-leaf.

## 1.8 Tebuconazole as a model compound

Tebuconazole, (Bayer CropScience), is an effective multifunctional fungicide used to protect a number of agricultural crops (wheat, barley, rape, corn, rice, vineyards, etc.) against powder milder, rust, rots, leaf blotches and other spot diseases. Tebuconazole rapidly penetrates into plants through their vegetative organs and roots, inhibits ergosterol synthesis, preventing formation of cell membranes, and disrupts metabolic processes, causing the death of pathogens<sup>59</sup>. As Tebuconazole is potentially phytotoxic, new formulations need to be developed to increase the efficacy of Tebuconazole and minimise its harmful effects on the environment.

Tebuconazole is commercially the most important fungicide of Bayer. Tebuconazole is marketed under a number of brand names and in many mixture formulations both with other specific and contact fungicides, and also with insecticides in the seed treatment market.

The structural and physico-chemical properties are shown in Table 1.1.

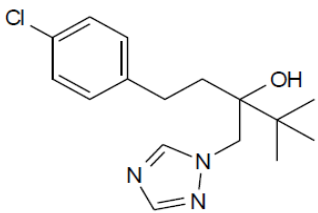
Chemical structure (1-(4-Chlorophenyl)-4,4-dimethyl-3-(1H-1,2,4-triazol-1-ylmethyl)-3-Pentanol)	
Molar mass (g mol <sup>-1</sup> )	307.145
Solubility in water (mg/L, 20 °C)	36
Melting point (°C)	104.7
log <i>K</i> <sub>ow</sub> (20 °C)	3.7

Table 1.1: Structural and physico-chemical properties of Tebuconazole.

Depending on if the AI has a systemic or contact action the formulation also needs to be designed to enhance the penetration into the leaf or increase the wetting of the leaf surface; contact AIs need good wetting in order to work while systemic ones, where the compound redistributes inside the plant, need to penetrate the leaf in order to have an effect, so complete coverage is not necessary for effective performance. Tebuconazole displays a mixture of both behaviours.

# Chapter 2

## 2. Evaporation Dynamics of Sessile Droplets

Studies on evaporation of sessile droplets have been conducted over the past 50 years and have sharply increased over different research areas: life, health and physical sciences. A sessile drop is a drop which is deposited on a solid substrate where the wetted area is limited by a contact line (CL). Upon drying, a droplet of liquid typically leaves a ring of solute on the substrate on which it rested. Sessile drop evaporation processes have important applications in ink-jet printing<sup>60,61</sup>, spraying of pesticides<sup>62</sup>, micro/nano fabrication<sup>63</sup>, thin film coating<sup>64</sup>, biochemical assays<sup>65</sup>, spray cooling<sup>66</sup>, deposition of DNA/RNA micro-arrays<sup>67,68</sup>, and manufacture of novel optical and electronic materials<sup>69</sup> in the last decades.

### 2.1 Wettability of a sessile droplet

The topic of wetting has received tremendous interest from both fundamental and applied points of view. It plays an important role in many industrial processes, such as oil recovery, lubrication, liquid coating and printing<sup>70,71,72</sup>.

Wettability studies usually involve the measurement of contact angles, which indicates the degree of wetting when a solid and liquid interact. Small contact angles ( $\ll 90^\circ$ ) correspond to high wettability, while large contact angles ( $\gg 90^\circ$ ) correspond to low wettability. More specifically, a contact angle less than  $90^\circ$  generally means that wetting of the surface is favourable, and the fluid will spread over a large area on the

surface; while contact angles greater than  $90^\circ$  generally means that the wettability of the surface is unfavourable so the fluid will minimize its contact with the surface and form a compact liquid droplet. Note that the contact angle is always measured inside the liquid phase. For example, complete wetting occurs when the contact angle is  $0^\circ$ , as the droplet turns into a flat puddle.

If the drying is controlled by diffusion in the vapour phase, which is the case in this thesis, the drying time depends only on the radius and the contact angle of the droplet, thus the evaporation of pinned droplets on hydrophilic substrates is faster than on hydrophobic substrates as the first ones have a lower contact angle<sup>73</sup>.

Ideally, the shape of the droplet is determined by the surface tension of the liquid. In a pure liquid, each molecule in the bulk is pulled equally in every direction by neighbouring liquid molecules, resulting in a net force of zero. However, the molecules exposed at the surface do not have neighbouring molecules in all directions to provide a balance net force. Instead, they are pulled inward by the neighbouring molecules creating an internal pressure<sup>74</sup>. As a result, the liquid voluntarily contracts its surface area to maintain the lowest surface free energy. This intermolecular force to contract the surface is called surface tension and it is responsible for the shape of liquid droplets.

Contact angles ( $\theta$ ) of sessile drops on a substrate are used in the calculation of the surface free energy of the solid surfaces. The wettability of a solid surface by a liquid drop can be expressed by the static contact angle ( $\theta$ ) between the gas-liquid and solid-liquid interfaces<sup>75</sup>. The angle  $\theta$  is related to the interfacial tensions of solid–vapour ( $\sigma_{sv}$ ), solid–liquid ( $\sigma_{sl}$ ), and liquid–vapour ( $\sigma_{lv}$ ) by Young’s equation<sup>76</sup>:

$$\cos \theta = (\sigma_{sv} - \sigma_{sl}) / \sigma_{lv} \quad \text{Eq. 2.1}$$

For an ideal flat surface,  $\theta$  is unique and depends on the chemical composition of the substrate. However, on a real (non-ideal) surface,  $\theta$  can exist in a range of angles,  $\theta_r \leq \theta \leq \theta_a$ . Here,  $\theta_a$  is referred to as the advancing contact angle beyond which the drop begins to expand. In contrast,  $\theta_r$  denotes as the receding contact angle below which the

drop starts to withdraw. The difference between  $\theta_a$  and  $\theta_r$  is known as the contact angle hysteresis (*CAH*).

The significance of contact angle hysteresis has been extensively investigated<sup>77,78,79</sup>, and the general conclusion is that it arises from surface roughness and/or heterogeneity. For surfaces that are not homogenous, there exist domains that present barriers to the motion of the contact line. Young's equation can be misleading because the equation fails to consider surface topography. Although roughness and heterogeneity of a solid substrate contribute substantially to the *CAH*, they are not the only reasons. Other sources of hysteresis come from the chemical interaction between the liquid and the solid<sup>31</sup>. If the liquid contains other species (surfactants, etc.), there can be a layer that deposits on the substrate surface. This adsorption can be a source of heterogeneities, leading to a possible modification of the solid surface tension locally. Penetration of liquids in the microporosity of a condensed monolayer can also lead to hysteresis of the contact angle.

As some authors have shown<sup>80,81</sup>, after a short transient in which a droplet deposited onto a substrate rapidly adjusts to a quasi-equilibrium shape with initial contact radius  $R_o$  and initial contact angle ( $\theta$ ), the droplet can evaporate in different modes:

- *Constant contact radius (CCR) mode*, in which the CL is always pinned and the contact angle  $\theta = \theta(t)$  decreases while the contact radius  $R(t) = R_o$  remains constant,
- *Constant contact angle (CCA) mode*, in which the CL does not pin and the contact radius  $R = R(t)$  decreases while the contact angle  $\theta(t) = \theta_o$  remains constant.

Despite the simplicity of the *CCA* and *CCR* modes of evaporation, there are numerous documented cases which do not fit into either description. The simplest of these is a mixed mode in which the contact line undergoes successive jumps between pinning sites, commonly known as stick-slip motion<sup>82</sup>: In the case of liquids which contain particles, the solute deposition at the contact line occurs during the *CCR* stage (stick), followed by sudden depinning (slip) during which  $R$  decreases and  $\theta$  increases before the process repeats in a series of discontinuous steps depositing concentric rings.

## 2.2 Geometry of a sessile droplet

The geometry of the evaporating drop is very important on the rate of drop evaporation. Both surface tension and gravity may determine the shape of a sessile droplet. Surface tension strives to maintain a spherical cap, while gravity acts to flatten the profile. Hence, the droplet shape<sup>83</sup> is controlled by the Bond number,  $B_o = \frac{\rho g R h_0}{\sigma}$ , which accounts for the balance of surface tension and gravitational force on the droplet and the capillary number,  $Ca = \eta \bar{u}_r / \sigma$ , which represents the relative influence of the surface tension and viscous effects. Here,  $\rho$  is the fluid density,  $g$  is the gravitational constant,  $R$  is the CL radius,  $h_0$  is the initial height of the droplet,  $\sigma$  is the air-water surface tension,  $\eta$  is the liquid viscosity and  $\bar{u}_r$  is the average radial velocity induced by droplet evaporation.

For small droplets with slow flows, as it is considered in this thesis, the Bond number and capillary number are small, so the droplets can be regarded as a spherical cap and gravitational forces and viscous can be neglected. In Figure 2.1, a small droplet on a surface with a spherical cap shape is presented. A cylindrical coordinate system is used with radial coordinate  $r$  and axial coordinate  $z$ .

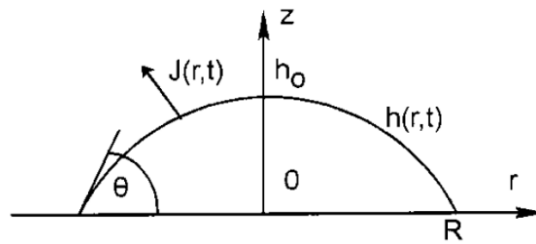


Figure 2.1: Droplet with spherical cap shape rests on a flat surface.

In Figure 2.1,  $\theta$  is the contact angle,  $h(r,t)$  is the local height, and  $J(r,t)$  is the local evaporation flux.  $S = \{h(r, t) | r \leq R\}$  defines the surface of the droplet where  $h(r,t)$  is

$$h(r,t) = \sqrt{\frac{R^2}{\sin^2 \theta} - r^2} - \frac{R}{\tan \theta} \quad \text{Eq. 2.2}$$

where  $R$  is the contact-line radius.

The surface area  $S$  of sessile droplet (i.e. liquid–vapour interface area) can be calculated by

$$S = \frac{2\pi R^2}{1 + \cos \theta} \quad \text{Eq. 2.3}$$

For sessile droplets, the volume of the spherical cap is related to the radius of wetted area and contact angle as follows:

$$V = \pi R^3 \frac{\cos^3 \theta - 3\cos \theta + 2}{3\sin^3 \theta} \quad \text{Eq. 2.4}$$



## 2.3 Evaporation of a sessile droplet: single solvent fluids

The evaporation of liquid droplets is of fundamental importance in a huge variety of practical situations and has been the subject of considerable theoretical and experimental research in recent years<sup>84,85,102</sup>. The evaporation of a liquid drop<sup>86</sup> is basically a simultaneous heat and mass transfer operation in which heat for evaporation is transferred by conduction and convection from warm air to the drop surface from which the vapour is transferred by diffusion and convection back into the air. Drop evaporation also involves the conductive heat transfer into the substrate, the convective heat transfer induced by the surface tension gradients and the natural convection due to the temperature gradients in the liquid drop.

The sessile droplets rest on a flat substrate that is assumed to be impermeable to the liquid. While there is no diffusion through the substrate, depending on the condition of the gas phase, mass transfer between the fluid and gas phases may occur that causes loss (evaporation) or accumulation (condensation) of the droplet volume. At room temperature, if the ratio of liquid vapour pressure in air to the saturated vapour pressure (known as “*RH*” if the liquid is water) is less than 1, the number of liquid molecules leaving the surface of the droplet and diffusing into the ambient air is greater than the number of the vapour molecules diffusing into the droplet. This net transfer of liquid molecules to the air causes the loss of liquid volume.

Accordingly, the evaporation process<sup>87</sup> follows these two separate steps:

1. *Kinetics*: where the liquid molecule at the fluid–gas interface receives the enthalpy of evaporation (latent heat of evaporation), and transforms to a vapour molecule at the surface,
2. *Diffusion*: where the vapour molecule at the surface leaves the surface and goes to the ambient air.

The evaporation happens after the completion of these two steps. If one process is much slower than the other, it controls the evaporation process. Hence the evaporation can be classified to two different types:

1. *Kinetically-controlled evaporation*: where the kinetic transformation happens at a slower rate than the diffusion, and
2. *Diffusion-controlled evaporation*: where the diffusive relaxation of the saturated vapour layer immediately above the drop defines the rate limiting step.

In the former case, the evaporation is uniform over the surface, while in the second case, the evaporation is strongly enhanced near the edge of the droplet (Figure 2.2).

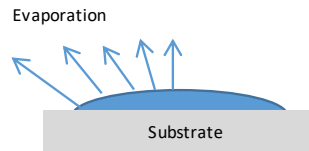


Figure 2.2: Schematic of a sessile droplet drying on a substrate. The evaporation rate at the surface of the surface is enhanced toward the edge of the droplet.

For a small water droplet with a radius less than 1 mm, the time for the diffusion process at the surface of the droplet scales with  $\sim R^2 / D_w$ , where  $R$  is the radius of the droplet and  $D_w$  is the vapour diffusivity of water in air ( $26.1 \text{ mm}^2 \text{ s}^{-1}$ ). The time for the kinetic process,  $t_k$ , is the water molecule transformation time scale and can be calculated from the Hertz-Knudsen equation<sup>88</sup>. For water molecules at room temperature ( $\sim 24 \text{ }^\circ\text{C}$ ),  $t_k$  is of the order of  $10^{-10} \text{ s}$  which is much faster than the diffusion process ( $\sim 10^{-3} \text{ s}$ ). Thus, a diffusion-controlled evaporation is considered. In this case, the vapour close to the droplet is saturated. Far from the droplet, the vapour density approaches an ambient vapour density,  $\rho_\infty = RH \rho_{vap}$ , where  $RH$  is the relative vapour pressure or humidity for water and  $\rho_{vap}$  is the saturation vapour density at the temperature on the droplet surface.

The vapour concentration in the vicinity of the liquid–vapour interface has a time dependence governed by the unsteady diffusion equation

$$\partial c / \partial t = D_w \Delta c \quad \text{Eq. 2.5}$$

where  $c$  is the local water vapour mass concentration and  $D_w$  is the vapour diffusivity.

Hence, the water vapour concentration adjusts rapidly compared to the time required for droplet evaporation and the water evaporation can be considered to be a quasi-steady state. We therefore neglect the transient term in Eq. 2.5 and obtain the Laplace equation for the vapour concentration distribution (Eq. 2.6).

$$\Delta c = 0 \quad \text{Eq. 2.6}$$

The evaporation flux on the droplet surface follows the equation suggested by Deegan et al<sup>100</sup>,

$$J(r, \theta) = J_0(\theta) \left( 1 - \left( \frac{r}{R} \right)^2 \right)^{-\lambda(\theta)} \quad \text{Eq. 2.7}$$

where the exponent  $\lambda$  is a parameter reflecting the uniformity of evaporation flux along the droplet surface and is approximated by  $\lambda(\theta) = 0.5 - \theta / \pi$  with  $\theta$  in radians, and  $J_0(\theta)$  given by<sup>89</sup>

$$J_0(\theta) = \frac{(1 - RH) \rho_{vap}}{R} \left( \frac{(8\pi - 4) \left( \theta - \frac{\pi}{2} \right)^2}{\pi^3} + 1 \right) \quad \text{Eq. 2.8}$$

The average rate of evaporative mass transfer,  $m$ , is given approximately by

$$-m(t) \approx \pi R D_{vap} (1 - RH) \rho_{vap} (0.27 \theta^2 + 1.30) \quad \text{for } 0 < \theta < \frac{\pi}{2} \quad \text{Eq. 2.9}$$

where  $D_{vap}$  is the diffusion coefficient of the vapour and  $\rho_{vap}$  is the vapour density at the surface of the drop.  $\rho_{vap}$  at atmospheric pressure may be calculated from the vapour pressure  $p_{vap}$  using the perfect gas equation of state<sup>90</sup>:

$$p_{vap} = \frac{\rho_{vap} RT}{M} \quad \text{Eq. 2.10}$$

where  $M$  is the molecular molar mass.

It is assumed that the droplet temperature is close enough to the ambient temperature of the surrounding gas that saturation vapour pressure is the value at ambient temperature.

From Eq. 2.9, the average evaporative mass loss per unit area of substrate surface (i.e. the mass flux) is given by,

$$J_{ave} = \frac{-m}{\pi R^2} \approx \frac{D_{vap}(1-RH)\rho_{vap}}{R}(0.27\theta^2 + 1.30) \quad \text{Eq. 2.11}$$

The average rate of heat loss due to latent heat of evaporation is then  $J_{ave} \Delta H_{vap}$ , where  $\Delta H_{vap}$  is the heat of vaporization per unit mass of liquid. If this is balanced by steady-state heat conduction from the substrate, whose rate is around  $k_L \Delta T / h_0$ , where  $k_L$  is the thermal conductivity of the liquid, one can estimate the steady-state temperature change from the bottom to the top of the droplet due to drying as

$$\Delta T = \frac{J_{ave} \Delta H_{vap} h_0}{k_L} = \frac{\Delta H_{vap} h_0 D_{vap} (1-RH)\rho_{vap}}{R k_L} (0.27\theta^2 + 1.30) \quad \text{Eq. 2.12}$$

## 2.4 Particle transport in drying droplets

In this section, the two main causes of particle transport in droplets are described: the “coffee ring effect” (evaporation-driven flow) and Marangoni flow.

### 2.4.1 The “coffee ring effect”

The evaporative flux is not equal over the entire drop surface unless  $\theta = 90^\circ$ . For a drop where  $\theta < 90^\circ$ , the flux is highest at the periphery and in order to maintain the

spherical cap profile imposed by the surface tension, there is a capillary flow to the CL to replenish lost liquid (Figure 2.3).

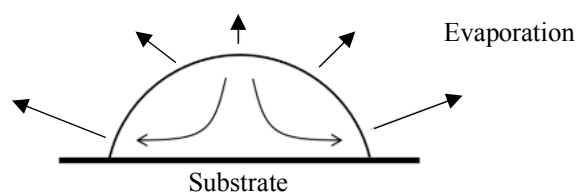


Figure 2.3: Schematic of the “coffee ring effect” in an evaporating sessile droplet with a pinned CL. The evaporative flux is indicated by the blue arrows, and the internal convective flow by the black arrows.

This flow transports particles inside the droplet radially outwards, where a ring stain forms. This phenomenon was first explained by Deegan et al.<sup>91</sup> and is commonly known as the “coffee-ring effect” because the pattern formed on the surface when a droplet is dried is very similar to a coffee droplet dried onto a surface. Understanding the flow within the evaporating droplet is crucial to control the shape and composition of the deposit that has been formed on the substrate. A ring stain is not always an unfavourable outcome. For crop spraying applications, “the coffee-ring effect” can lead to the optimal combination of adjuvant oil and the active particulate ingredient<sup>92</sup>.

The deposit resulting from a dried droplet can be influenced by the droplet wetting behaviour (movement and shape of the CL), particle transport by internal flows, particle interactions with each other or the substrate, particle shape, the particle concentration and by the addition of additives. The addition of additives with different chemical properties has been used as a method to modify the morphology of the deposit of a dried droplet. For example, Anyfantakis et. al,<sup>93</sup> described some patterns after the evaporation of drops containing fumed silica nanoparticles of varying wettabilities for an extended particle concentration range. They showed that the interaction between particles with different hydrophobicities affected the final deposit. Talbot et. al,<sup>94</sup> have shown that an evaporation-driven sol-gel transition in Laponite suspensions can be used to control the morphology of a deposit. Also, paint manufacturers use a variety of additives to ensure that the pigment is evenly dispersed and remains so during drying.

## 2.4.2 Marangoni flows

Marangoni flows were first described in 1855<sup>95</sup> and offer an additional particle transport mechanism to the “coffee-ring effect”. Surface at equilibrium have identical surface tension at all points and, in the absence of external agitation, the fluid remains at rest. However, evaporation can generate temperature variations in the vicinity of the solid surface and along the drop interface. For pure liquid drops, the Marangoni effect, which is thermo-capillary convection, can produce instabilities at the interface. On the other hand, if a drop is placed on a heated substrate, the large temperature difference between the drop and the substrate is the source of these thermo-convective instabilities, induced by both Marangoni and buoyancy forces for this case. In order to balance tangential stresses, the fluid moves from low to high surface tension in accordance with

$$\frac{\delta\sigma}{\delta x} = -\eta \frac{\delta u}{\delta n} \quad \text{Eq. 2. 13}$$

where  $x$  is the tangential coordinate,  $n$  is the normal coordinate,  $\sigma$  is the surface tension,  $\eta$  is the fluid viscosity, and  $u$  is the tangential component of the fluid velocity at the liquid–vapour interface.

The Marangoni flow at the interface causes fluid inside the droplet to recirculate (Figure 2.4).

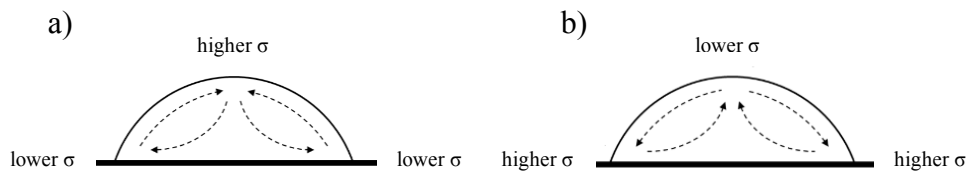


Figure 2.4: Marangoni flow direction along the liquid–vapour interface from a) CL to apex, b) apex to CL.

Modification of the internal flow profile from the radial flow regime can reduce particulate transport to the CL, reducing ring staining.

A surface tension gradient is also induced by adding surfactants or by binary solvent mixtures. The surfactant addition lowers the surface tension and as the evaporation is faster at the CL, the concentration of surfactant rises faster at the CL than at the apex. Accumulation of the additive at the periphery of the droplet causes Marangoni flow directed from CL to apex along the liquid–vapour interface (Figure 2.4). Alternatively, solvent mixtures with differential evaporation of components of different surface tension can introduce solutal Marangoni flows into evaporating droplets<sup>96,97</sup>. For binary solvent mixtures, the Marangoni flow direction is dependent on whether the more volatile components possesses a lower/higher surface tension compared to the less volatile component. If the more volatile component has the higher surface tension, then the Marangoni flow direction is described by Figure 2.4a. In the opposite case, the Marangoni flow direction is described by Figure 2.4b.

## **2.5 Evaporation of complex liquids**

The experimental and theoretical studies carried out so far, have taken into account different physical processes: heat transfer inside droplets, mass diffusion in bi- and multicomponent fluids, thermal conductivity of the solid substrate, Marangoni convection inside the droplets, etc. However, a comprehensive knowledge of the phenomenon is still lacking, especially for complex fluids (surfactant solutions, suspensions, and so on).

### **2.5.1 Influence of aqueous surfactant solutions on droplet evaporation**

Surfactants can influence the evaporation kinetics of water in two different ways. First, the presence of surfactant slows down the evaporation because of i) decrease of molar fraction of water and ii) formation of an adsorbed monolayer. In this thesis, only diluted surfactants solutions were used and neither of these effects are important in reducing evaporation rate.

Another, and the most effective, way the surfactant influences the droplet evaporation rate is indirectly through the change in the droplet geometry. Sefiane<sup>98</sup>, Soboleva and Summ<sup>99</sup>, Gutierrez et al.<sup>100</sup>, Gokhale et al.<sup>101</sup>, and Alexandridis et al.<sup>102</sup> have carried out experiments on the kinetics of evaporation of droplets of surfactant solutions. Their results have led to a conclusion that the surfactants play an important role in the spreading and evaporation of droplets of surfactant solutions: the presence of surfactants favoured higher values of the radius on hydrophobic substrates (due to the decrease of the contact angle) and therefore higher evaporation rates<sup>117</sup> (see Eq. 2.9).

### 2.5.2 Influence of colloidal suspensions on droplet evaporation

Colloidal suspensions are found all around in everyday life events such as paints, milk, coffee, blood etc. This term can be defined as a disperse phase of solid particles (micrometre size) which are homogeneously mixed in a bulk fluid or a continuous medium.

The presence of nano- or microparticles inside a liquid droplet can affect considerably the evaporation kinetics due to molecular interactions. Depending on particles and substrate properties, particles can accumulate at the liquid–air interface and/or liquid–substrate interface. In particular, particles can deposit on the substrate near the three-phase CL (coffee-ring effect) and keep the CL pinned during the evaporation process increasing in this way the evaporation rate. An increase in nanoparticles concentration results in an increase of the pinning time and therefore in a decrease of the droplet lifetime. The pinning of the CL by particles depends on hydrophobicity/hydrophilicity of the substrate. With particles stick-slip motion can occur that give rise to concentric rings.



# Chapter 3

## 3. Experimental methods: instrumentation and procedures

Different techniques have been used to study the chemical and physical properties of the formulations and dried deposits described in this thesis. Nuclear magnetic resonance was used to study the solubility of the AI in the surfactant solutions and also for studying micellar solutions. Also, results from scanning electron microscopy (SEM) combined with electron dispersive X-ray (EDS) and Raman spectroscopy were combined to get a better understanding of the association between the adjuvant and AI on dried deposit. Finally, Franz cell diffusion method determined the penetration of AI through cuticles of real leaves. In this chapter, an introduction of each experimental technique is described and some of their fundamental concepts are explored.

### 3.1 Substrate preparation

The glass substrate was modified to increase its hydrophobicity as the experimental goal is to mimic a leaf surface. Silane coatings were used to achieve contact angles between 70–100°. Glass cover-slips were cleaned by rinsing in 2% Decon 90 in a sonicating bath for 1 h, followed by a rinse in high-purity water. The rinsed substrates were then dried with nitrogen and rinsed again in chromosulfuric acid (composition 5% Na<sub>2</sub>Cr<sub>2</sub>O<sub>7</sub> in 90% H<sub>2</sub>SO<sub>4</sub> abbreviated as BIC) for 2 h followed by a rinse in high-purity water. The rinsed substrates were dried again with nitrogen and left in an oven at 100 °C for 1 h.

Once the substrates were dried at high temperature, they were immersed in a silane solution. 2% Octadecyltrichlorosilane (OTS) + toluene solution was used for the coating treatment on glass substrates for 1 h. Substrates on a wafer holder were put into a beaker with a 2% OTS + toluene solution which was covered with a glass flask to protect the solution from moisture into a desiccator.

Another way to do the silane coating was by vapour phase deposition. A clean wafer holder with glass substrates was put close to a watchglass with 1 mL of the silane selected (Chloro(dimethyl)octylsilane (CDO) or Hexamethyldisilazane (HMDS). They were put into a desiccator connected to a vacuum pump so that the air pressure is reduced and the diffusion coefficient of silane is increased.

After the silanization process by two different ways, the substrates were rinsed with high-purity water or with the solvent used during the silanization process in case of liquid coating, followed by high-purity water and maintained overnight at 30 °C to ensure the complete drying. The substrates were cooled to room temperature and stored before being used.

## **3.2 Fluid preparation**

For the simplest experiment, high purity water (MilliQ) was used. Polystyrene spheres (PS) with a diameter  $d = 1000$  nm were added at a concentration of 0.01% for particle tracking of the internal flows. Polystyrene suspensions were ultra-sonicated for 15 min prior to use to break up any aggregates. For the next experiments, an alkyl ethoxylate and an amidoamine-based surfactant with PS particles were used. PS particles (0.01%) and surfactant solutions at different concentrations (1 g/L and 3 g/L) were mixed for 1 h and ultrasonicated for 20 min.

For the last batch of experiments, the active ingredient (AI), 2.59 g of 25% SC Tebuconazole, was added to surfactants solutions at both concentrations and stirred for 2 h and ultrasonicated for 30 min. For Surf2, the temperature of the sonicator bath was set 80 °C. When the surfactant solutions had the AI in the formulation, these PS

particles were not added because the size of the particles of AI is bigger than the PS ones.

Some additives such as Laponite, silica particles or “Superspreader” surfactants were added to the surfactant + AI solutions in order to modify the final deposit. Details for the preparation of each are described in Section 5.7.1.

### 3.3 Experimental set up for printing system

This section describes the experimental set-ups used for high-speed imaging of drying droplets.

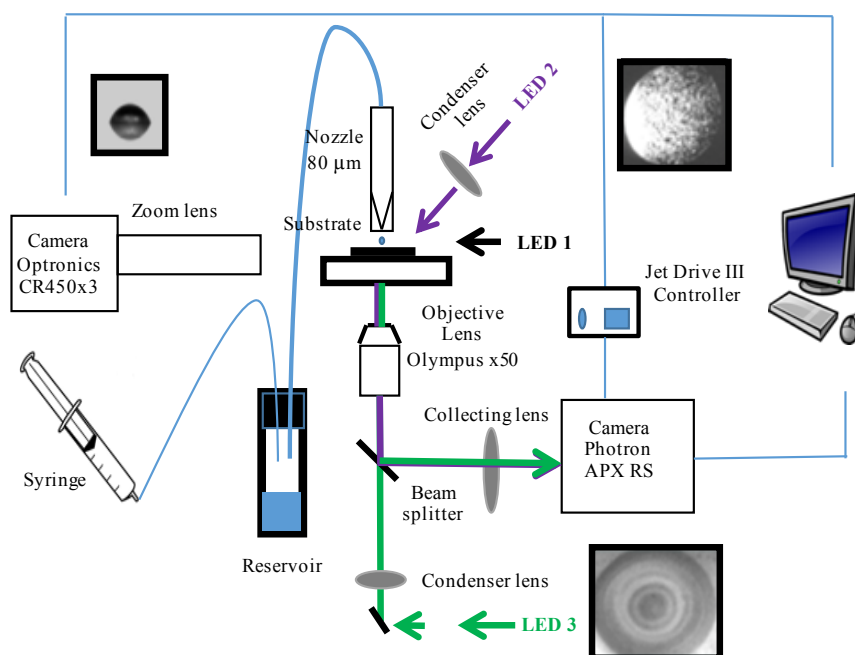


Figure 3.1: Schematic of the experimental set-up for imaging the droplet profile during evaporation and the internal flows.

Figure 3.1 combines a side-profiling and an inverted microscope, allowing both the profile of the droplet and internal flows to be imaged simultaneously to get information about contact angle, diameter and volume of the droplet as well as the shape of the deposit that is formed. A mid-speed camera (Optronics CR450-3), coupled with collimated illumination from a LED 1 (Beaglehole Instruments,  $\lambda = 455$  nm), was used

to image the droplet profile. A zoom lens (LaVision, 12x Zoom Lens) magnified the droplet. For the inverted microscope, a high speed camera (Photron, FASTCAM APX RS) and 50x magnification objective lens (Olympus, NA 0.5, WD 10.6 mm) were used for image capture. To image the internal flows, tracer particles were included within the fluid and imaged using dark field microscopy (a collimated LED 2,  $\lambda = 505$  nm, Thorlabs). This light source is focused onto the substrate from above, at an angle to avoid the nozzle. PS tracer or AI particles were visualized as bright spots (from back-scattered light) on a dark field. Drops were also illuminated by a second collimated LED (Thorlabs,  $\lambda = 505$  nm, LED 3). Light from the source was passed through the rear aperture of the objective lens and onto the underside of the sample. This light was suited to the tracking of phase changes within the droplet. The illumination with LED 2 and 3 are complementary and when both were employed simultaneously, complex drying dynamics were effectively visualised. LED 2 highlighted the shape of the drop footprint.

Nanoliter droplets were ejected from a Microfab piezoelectric (MJ-ABP-01, Horizon instruments) with an 80- $\mu\text{m}$  orifice. The device was connected to a fluid reservoir pressurised by a syringe. DOD printing was controlled using a Microfab driver unit (Microfab CT-M3-02 JetDrive III Controller) that was controlled by software (Microfab, JetServer v1.03.05) on the computer. The driver can induce the printing of a single drop on demand or a continuous stream of drops at a specified frequency. Single droplet emission was initiated by the electronic pulse sent to the piezoelectric device contained within the nozzle. The drop volume was about 1.5 nL. All experiments were done a room temperature,  $T = 22 \pm 1$  °C and a relative humidity of  $40 \pm 3\%$ .

The voltage of the waveform was adjusted in order to allow emission of single droplets with impact velocities of approximately 1–2  $\text{m s}^{-1}$ . The typical voltage range to emit a single water droplet from a new nozzle was 30–40 V for water droplets or 70–80 V either for surfactant solutions or surfactant and AI solutions. The nozzle–substrate separation was  $\sim 2$  mm. A stage was used to move a clean section of substrate under the nozzle before the next droplet was deposited. The nozzle must be clean before

printing because the formation of a dried particulate film across the nozzle orifice would stop jetting.

For some of the experiments, parameters such as temperature of the substrate and humidity were controlled in order to study the effect of them on the morphology of the final deposit on the substrate. A humidity control cell was used to regulate the relative humidity in the vicinity of the droplet between a  $RH$  of  $23-80 \pm 4$ . To raise the  $RH$  inside the cell, compressed air was pumped in through a miniature bubbler (containing water). To lower the  $RH$ , compressed air was instead pumped through tubing filled with silica gel. The compressed air was then turned off once the desired relative humidity was reached, ensuring that no air currents affected the droplet during image acquisition. The  $RH$  and temperature inside the humidity control cell were measured using a thermohygrometer (Extech) with a probe inside the cell.

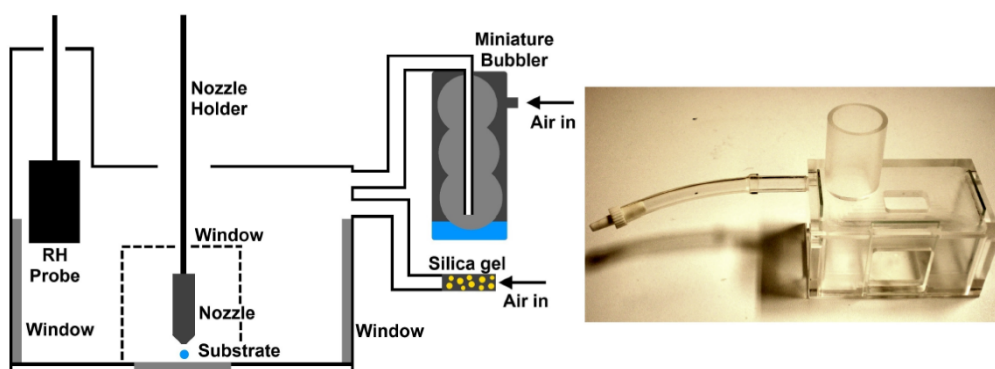


Figure 3.2: Humidity control cell schematic diagram (left) and photograph of cell (right).

A heated stage was used to control the temperature of the drying drop (Figure 3.2). The temperature of the stage was controlled using a pair of Peltier elements mounted between an aluminium plate and a heat sink. The Peltier elements were controlled using a microprocessor employing a PID algorithm. A high precision digital temperature sensor (absolute accuracy of  $\pm 0.13$  °C between 20 and 70 °C) was used to give real time information on the temperature of the stage. The temperature could be varied between 15.0 and 45.0 °C with a long term stability of  $\pm 0.02$  °C. The substrate was left at the set temperature for 5 min before any measurements were taken.

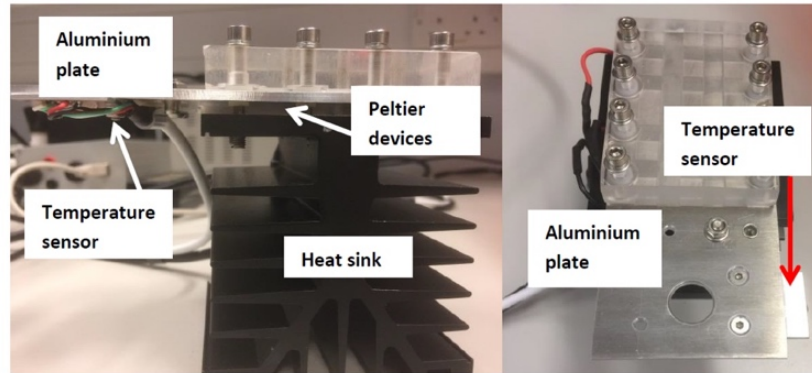


Figure 3.3: A labelled image of the heated stage used in some experiments from the side (left) and above (right).

Silane-coated glass substrates (OTS, CDO and HMDS) were used as evaporation substrates. The evaporation process was recorded with a video camera (1024 pixels x 1024 pixels) and the resolution was 50 frames per second (fps). Total evaporation times ranged between 5–18 s. At all concentrations, the experiment was repeated 5 times, showing consistent behaviour. Photographs of the entire deposit, obtained after evaporation was completed, were taken.

Images were collected at a shutter speed between 166  $\mu$ s and 500  $\mu$ s to allow enough light to image the particles, while still enabling the distinct particle positions to be resolved. Frame rate varied between 50 and 125 fps (depending on the droplet characteristics). Particles inside the droplet were imaged from below (through the substrate), requiring both the fluid and substrate to be adequately transparent.

### 3.4 Pendant drop tensiometry and contact angle measurements

The instrument used to measure interfacial tensions and contact angles (First Ten Ångstroms, FTÅ200) is schematically displayed in Figure 3.4.

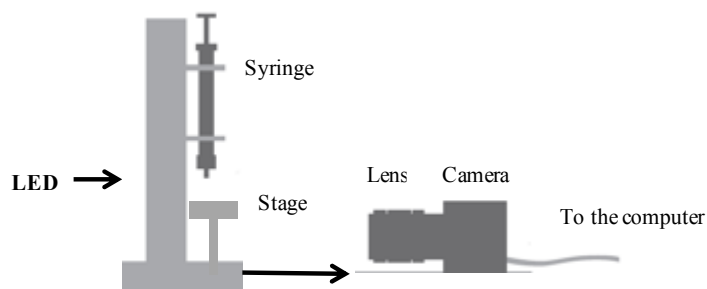


Figure 3.4: Schematic diagram of the instrument used to measure contact angles and interfacial tensions.

A highly accurate syringe pump driven by a stepper motor to dispense the drops is controlled through a computer that is also connected to a camera (Watec, Wat-902B) that allows us to capture the image to analyse the sample. The pump may also be run in reverse to aspirate a drop. Images were calibrated in situ using a 3 mm sphere.

#### 3.4.1 Surface tensiometry

The glassware, syringe, needle and cuvettes were bath-sonicated in dilute alkaline detergent solution for > 30 min (Decon Laboratories, Decon90), rinsed with water (MilliQ) and dried in an oven.

The surface tension of different solutions was measured by pendant drop tensiometry. Pendant drops were dispensed with Hamilton gas tight syringes. Interfacial tension measurements were carried out at room temperature ( $20 \pm 2^\circ\text{C}$ ). The interfacial tension of MilliQ water was measured at the beginning of each series of measurements. The variation of interfacial tension with the temperature variation experienced in the lab was neglected.

Data was extracted from captured images using the Fta32 v2.0 software that solves the Laplace-Young equation<sup>103</sup>. The software runs an edge detection routine and then solves the Young-Laplace equation numerically. The Laplace pressure is defined according to

$$\Delta p = \sigma \left( \frac{1}{R_1} + \frac{1}{R_2} \right) \quad \text{Eq. 3.1}$$

where  $\sigma$  is the surface or interfacial tension and  $R_1$  and  $R_2$  are the radii of curvature.

A pendant drop can be assumed axisymmetric and thus the hydrostatic pressure can be written as

$$\Delta p = \Delta \rho g h \quad \text{Eq. 3.2}$$

where  $\Delta \rho$  is the difference in density between the drop or bubble and the surrounding media,  $g$  is the acceleration due to gravity and  $h$  is the height of the drop.

The combination of Eq. 3.1 and 3.2 gives the Laplace-Young equation:

$$\Delta \rho g h = \sigma \left( \frac{1}{R_1} + \frac{1}{R_2} \right) \quad \text{Eq. 3.3}$$

Gravitational and interfacial forces must be of the same order of magnitude to have stable pendant drops and measure their interfacial tensions by drop-shape analysis, i.e. the Bond number (see Eq. 3.4) must be close to 1.

$$B_0 = \frac{\rho g r_0 h_0}{\sigma} \quad \text{Eq. 3.4}$$

where  $h_0$  is the distance between the needle and the drop/bubble apex,  $r_0$  is the equatorial radius and  $\sigma$  is the surface/interfacial tension.

For lower concentrations of surfactant ( $< 0.01$  g/L) very long times to equilibrate are needed (at least one hour). For this type of measurements, samples were decanted into cuvettes and an air bubble was formed at the tip of a J-shaped needle fitted onto an air-



filled syringe mounted in the mechanical dispenser. Concentrations below 0.001 g/L are not practical for any of the methods.

### 3.4.2 Contact angle measurements

Contact angles for either millimeter or micrometre diameter water droplets were measured on each substrate in order to compare the influence of the volume on the contact angle value using a video capture system. A needle with an internal diameter of 0.84 mm was used to obtain mm diameter water droplets (Section 3.4.2.2).

Silane solution	Coating	Time (h)	Initial contact angle (°) (mm diameter drop)	Initial contact angle (°) ( $\mu$ m diameter drop)
2% OTS + toluene	Liquid	1	101 $\pm$ 2	95 $\pm$ 2
1 mL CDO	Vapour	1	85 $\pm$ 1	86 $\pm$ 2
1 m HMDS	Vapour	2	74 $\pm$ 2	74 $\pm$ 2

Table 3.1: Different silane solutions used for the hydrophobic coating on glass substrates. OTS: Octadecyltrichlorosilane ( $C_{18}H_{37}Cl_3Si$ ), CDO: Chloro(dimethyl)octylsilane ( $C_{20}H_{43}ClSi$ ), HMDS: Hexamethyldisilazane ( $(CH_3)_3SiNHSi(CH_3)_3$ ).

#### 3.4.2.1 Contact angle of mm droplets

Contact angle measurements for sessile drops of different solutions were carried out using the FTÅ200 instrument. Solutions were deposited from a syringe equipped with a straight blunt needle onto hydrophobic substrates prepared as Section 3.4. Liquid sample and glassware preparation was conducted in the manner above in Section 3.2. The contact angles for 3  $\mu$ L pure water droplets were measured as a reference before each experiment.

In all cases, the syringe-substrate assembly was positioned on the tensiometer translation stage in front of the LED backlight and in view of the camera and zoom lens. Sessile drops were created by pressing a small amount of fluid out of the syringe needle and then raising the substrate using the translation stage to extract the pendant

drop. Video footage of the sessile drop formation was typically carried out at 10 fps for 5 s after transfer in order to track the contact angle over time. Contact angles were extracted using the Fta32 software. The user is able to define the drop baseline using the corners that show the points at which the drop and its reflection meet. The program can then fit a circular arc across the whole drop surface or, if the drop is distorted, it can perform a non-spherical fit to both contact points in turn. The equations that describe the drop edge and the baseline are then solved for their intersections and the equation for the drop edge is differentiated at the intersection to find the gradient<sup>103</sup>. The contact angle is given by the angle between the calculated drop shape function and the sample surface, the projection of which in the drop image is referred to as the baseline.

#### 3.4.2.1.1 Advancing and receding contact angle

If the needle keeps dispensing the solution while images are captured, advancing contact angle measurements are taken and contact angle versus drop width data is obtained. Figure 3.5 shows the measurement of advancing contact angle. Non-spherical analysis is used to avoid the top of the drop which is distorted by the dispensing needle.

Figure 3.5 also illustrates the case in which the pump is reversed and fluid is removed from the drop. The receding mode contact angle will normally be significantly lower than the advancing contact angle.

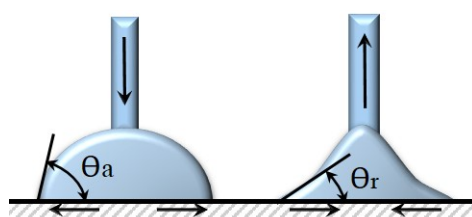


Figure 3.5: Advancing contact angle (left) and receding contact angle (right).

Contact angle obtained from a combination of measuring advancing and receding angles are sometimes plotted as shown in Figure 3.5. The difference between the advancing and receding contact angle is known as the “hysteresis”.

### 3.4.2.2 Contact angle of $\mu\text{m}$ droplets: MATLAB Image processing

The MATLAB script used to extract the drop geometry from side-view video footage was written by Dr. L. Yang. The core function of the program is to detect the edge of drops, fit a circular arc and extract the drop height, radius and contact angle. Edge detection is performed by importing a greyscale image as a matrix and using a Sobel operator to detect the rate of change of pixel greyscale along each image row and column.

The circular arc that best fits the edge is found using the equation for a circle:

$$x = a \pm \sqrt{(y-b)^2 - R^2} \quad \text{Eq. 3.5}$$

A calibration was made using a glass sphere of known diameter in order to convert dimensions from pixels to  $\mu\text{m}$ . Next, the video recording of a drying drop is imported. The camera is triggered before the drop arrives on the substrate so that the first frame is empty and can be considered a background and subtracted from all subsequent images. The removal of the background simplifies the images so that the only pixels that do not appear white are those that correspond to the drop. The other user inputs are the noise threshold and the frame rate. The drop baseline is manually identified which is where the drop and its reflection meet. The drop contact angle as a function of time is calculated from the tangent to the fitted circular arc at the baseline. The drop height  $h$  and  $r$  are calculated from the arc relative to the baseline, and assuming the drop is axisymmetric, its volume  $V$  then can be calculated using the spherical cap relationship.

$$V = \frac{1}{6}\pi h(3r^2 + h^2) \quad \text{Eq. 3.6}$$

### 3.5 Raman spectroscopy

Raman scattering was first observed by C. V. Raman in 1928<sup>104</sup> although it had been predicted in 1923 by A. Smekal<sup>105</sup>. Raman spectroscopy is a scattering technique. It is based on Raman Effect, i.e., frequency of a small fraction of scattered radiation is different from frequency of monochromatic incident radiation. It is based on the inelastic scattering of incident radiation through its interaction with vibrating molecules.

In Raman spectroscopy, sample is illuminated with a monochromatic laser beam which interacts with the molecules of sample and originates a scattered light. The scattered light having a frequency different from that of incident light (inelastic scattering) is used to construct a Raman spectrum. Raman spectra arise due to inelastic collision between incident monochromatic radiation and molecules of sample. When a monochromatic radiation strikes a sample, it scatters in all directions after its interaction with sample molecules. Much of this scattered radiation has a frequency which is equal to frequency of incident radiation and constitutes Rayleigh scattering. Only a small fraction of scattered radiation has a frequency different from frequency of incident radiation and constitutes Raman scattering. When the frequency of incident radiation is higher than frequency of scattered radiation, Stokes lines appear in Raman spectrum. But when the frequency of incident radiation is lower than frequency of scattered radiation, anti-Stokes lines appear in Raman spectrum (Figure 3.6).

Stokes shifted Raman bands involve the transitions from lower to higher energy vibrational levels and therefore, Stokes bands are more intense than anti-Stokes bands and hence are measured in conventional Raman spectroscopy while anti-Stokes bands are measured with fluorescing samples because fluorescence causes interference with Stokes bands. The magnitude of Raman shifts does not depend on wavelength of incident radiation. Raman scattering depends on wavelength of incident radiation<sup>106</sup>. A change in polarizability during molecular vibration is an essential requirement to obtain Raman spectrum of sample. A Raman spectrum is presented as an intensity-

versus-wavelength shift<sup>128</sup>. Raman spectra can be recorded over a range of 4000–10 cm<sup>-1</sup>. The details of the set-up are summarized in Section 6.3.

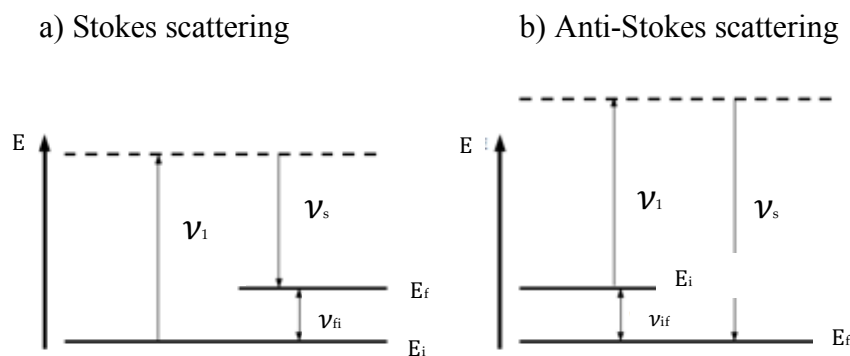


Figure 3.6: Different types of Raman Scattering.  $\nu_s$  is the frequency of the scattered light, and is given by  $\nu_s = \nu_1 - \nu_{fi}$  or  $\nu_s = \nu_1 + \nu_{if}$  depending on the type of scattering. The height of a level represents the amount of energy held by the scattering molecule when in that state.

The gross selection rule for Raman transitions is that the polarizability of the molecule should change as the molecule vibrates and the specific selection rule is  $\Delta v = \pm 1$ . The dipole moment,  $P$ , induced in a molecule by an external electric field,  $E$ , is proportional to the field

$$P = \alpha E \quad \text{Eq. 3.7}$$

The proportionality constant  $\alpha$  is the polarizability of the molecule. The polarizability measures the ease with which the electron cloud around a molecule can be distorted. The induced dipole emits or scatters light at the optical frequency of the incident light wave.

If a vibration does not greatly change the polarizability, then the polarizability derivative will be near zero, and the intensity of the Raman band will be low. The vibrations of a highly polar moiety, such as the O-H bond, are usually weak.

Raman spectroscopy is a reliable and non-destructive technique for the qualitative and quantitative analysis of trace particles. It is capable of analyzing solid and liquid samples very rapidly.

### 3.6 Proton nuclear magnetic resonance ( $^1\text{H}$ NMR) and Diffusion-ordered NMR spectroscopy (DOSY NMR)

Nuclear magnetic resonance spectroscopy (NMR) is an analytical method for determining the molecular structure and composition of chemical substances. Two-dimensional techniques are able to reveal more precise information about substances and are becoming more popular as NMR instruments become more advanced. NMR diffusometry (DOSY NMR) can be used for studying micellar solutions. This is performed by observing the diffusion properties of surfactants, inside and outside of micellar aggregates. The surfactants which are inside the micellar aggregates possess a lower diffusion since they are bigger than monomers outside the micelles.<sup>107</sup>.

In DOSY NMR, a pulse sequence of magnetic field with increasing gradient strength is applied to the sample. As the gradient amplitude of the pulse becomes more intense, peak intensities decrease exponentially. Different peaks may decrease at different rates. Diffusion coefficients can be inferred from the decay of the peak intensities with increasing gradient strength. The faster a peak decays, the larger its diffusion coefficient. For each peak, the measured apparent diffusion coefficient  $D_{app}$  is a weighted sum of the mobilities of the free analyte, of the analyte within larger entities (analyte in clusters/micelles) and of the mobility of the entity itself, if species exchange between environments on a time rate which is fast compared to the diffusion time in the pulse sequence.

The Stokes-Einstein equation relates the diffusion coefficient,  $D$ , of a particle to its hydrodynamic radius,  $r$ , in a solution of a given temperature,  $T$ , and dynamic viscosity,  $\eta$ :

$$D = \frac{k_B T}{6\pi\eta r} \quad \text{Eq. 3.8}$$

The advantage of DOSY is that it can be used as a non-invasive method to obtain both physical and chemical information. The spectrum also provides NMR information that can be used for assignment of individual components.

### 3.6.1 Sample preparation

Samples were measured at 25 °C on a 600 MHz Agilent spectrometer equipped with a probe with a z-gradient coil. The Oneshot45 pulse was used to acquire datasets in 2 h 38 min with twenty gradient amplitudes ranging from 2 to 29 G.cm<sup>-1</sup> in equal steps of gradient squared, using 64 transients, 32768 complex data points, a total diffusion-encoding gradient duration of 2 ms, and a diffusion time of 150 ms.

### **3.7 Scanning electron microscopy (SEM) and Energy-Dispersive X-Ray Spectroscopy (EDS)**

SEM with Energy Dispersive X-Ray (EDS) is ideally suited for the chemical and physical characterization of particulate matter. The Scanning Electron Microscope (SEM) was developed by Dr. Charles Oatlev in the 1950s. Electron microscopes utilize the same basic principles as light microscopes, but focus beams of energetic electrons rather than photons, to magnify an object. SEM produces images by scanning the sample with a high-energy beam of electrons.

An electron gun, located at the top of the device, shoots out an incident beam of highly concentrated electrons. There are two main types of electron guns used by SEMs. The first, thermionic guns heat a filament until electrons stream away and Field emission guns (the one used in this thesis), rip electrons away from their atoms by generating a strong electrical field.

The microscope is composed of a series of lenses within a vacuum chamber. These lenses focus the electrons on the sample. SEM requires a vacuum chamber to prevent oxidation of the filament and scattering of the electrons by residual gas.

When a sample is hit with the incident beam, it penetrates the sample to a depth of a few microns, depending on the accelerating voltage and the density of the sample. It emits X-rays and three kinds of electrons: primary backscattered electrons, secondary electrons and Auger electrons. The energy of the primary electrons determines the quantity of secondary electrons collected. The emission of secondary electrons from the sample increases as the energy of the primary electron beam increases, until a certain limit is reached. Beyond this limit, the collected secondary electrons diminish as the energy of the primary beam is increased, because the primary beam is already activating electrons deep below the surface of the sample. Electrons from such depths usually recombine before reaching the surface for emission.

A hole in an inner shell (here: K shell) of the specimen atom is generated by an incident high energy electron that loses the corresponding energy transferred to the ejected electron. The hole in the K shell is subsequently filled by an electron from an outer



shell (here: L3). The energy is emitted as a characteristic X-ray quantum. The energy of the X-ray is characteristic of the specimen atomic number from which it is derived.

The SEM uses Energy-Dispersive X-Ray Spectroscopy (EDS) in the production of spectra and elemental maps, which accurately represent the distribution of elements within samples.

### 3.7.1 Sample preparation

Silicon samples with dried droplets of agrochemical solutions must be electrically conductive at least at the surface, and electrically grounded to prevent the accumulation of electrostatic charge at the surface. Thus, the samples had been covered with 10 nm gold layer in an evaporation chamber.

### 3.8 Liquid Chromatography-Mass Spectroscopy (LC-MS)

LC-MS is an analytical technique that combines the separation capabilities of liquid chromatography with the mass analysis capabilities of mass spectrometry. This technique has a high sensitivity and selectivity and is useful in many applications.

The liquid sample is injected onto a column (LC), where the complex mixture is separated according to its interactions with the stationary and mobile phase. As the sample leaves the column it is introduced into the mass spectrometer by means of either electrospray ionization (ESI, liquid - based soft ionization technique) or atmospheric pressure chemical ionization (APCI). ESI method is sensitive to amines and gives accurate results when the solution contains only water and tebuconazole. However, when the solution that is analysed also contains surfactants, it is preferred to use APCI due to possible matrix effects such as ion suppression (caused by coelution in the LC of surfactant with tebuconazole).

The ESI mechanism forms charged droplets which carry a single or multiple charges. The mass-to-charge ( $m/z$ ) of the ions is detected by the MS. In brief, a liquid sample is sprayed through a capillary needle which is held at a high electrical potential with respect to the entrance of the mass spectrometer. This electric field induces a charge accumulation at the liquid surface, located at the end of the capillary, to form a Taylor cone. At a critical point the liquid breaks away, from the tip of the Taylor cone, to form highly charged droplets. The creation of a Taylor cone reduces the charge-to-surface ratio of the newly formed droplet. The release of the droplet is facilitated by a nebulizing gas which flows around the outside of the capillary and directs the droplet to the MS. Once airborne, the droplet reduces in size by means of solvent evaporation and Coulombic explosions caused by charge repulsion forces. This process is repeated until a single, multiply-charged analyte ion is produced.

The main advantage of the use of ESI for quantitative LC-MS is the formation of protonated or de-protonated molecules with little fragmentation. It is applicable to

polar, ionic and large analyte molecules. The primary disadvantage of ESI is the possibility of ion suppression or enhancement, caused by competition between ions for ejection from the droplet during desolvation.

The way to produce ionized analyte with APCI is very different. In APCI, the LC eluent is sprayed through a heated (typically 300–500 °C) capillary vaporizer. The resulting gas-phase solvent molecules are ionized by electrons discharged from a corona needle. The gas-phase solvent molecules form stable reactant ions. Proton transfer occurs between these reactant ions and sample molecules (ion–molecule reaction), and the sample molecules either add or lose protons to become ions. This ion–molecule reaction is known to occur in a variety of patterns, such as proton shift reactions, electrophilic addition reactions, etc. The resulting sample ions then pass through an orifice into the mass analyzer. Typically APCI is less prone to ion suppression than Electrospray.

Regardless of the type of ionization, voltages applied in the mass analyzer then focus the formed ions through the optic path of the mass analyzer. For maximum sensitivity and selectivity the Tebuconazole samples were analysed in MRM (multiple reaction monitoring) mode after Electrospray/APCI ionization. MRM is a tandem mass spectrometric technique that allows the monitoring of specific Collision Induced Dissociation (CID) reactions. The first quadrupole selects and transmits a parent ion with a specific  $m/z$  to a collision cell. This ion is then fragmented in the collision cell, and a specific daughter ion with a defined  $m/z$  is selected and transmitted by the second quadrupole to the detector. The combination of a specific parent mass and a unique daughter ion is generally an unambiguous and sensitive method to selectively monitor and quantify a compound of interest.

# Chapter 4

## 4. Determination of physico-chemical properties

### 4.1 Introduction

The critical micelle concentration (CMC) is defined as the concentration above which micelles form. The formation of micelles from the constituent monomers involves a rapid, dynamic, association-dissociation equilibrium. The concentration at which the micelles become first detectable depends on the sensitivity of the experimental probe used.

This situation is directly analogous to the solubility limit of a dissolved material, which, once exceeded, would normally result in crystallisation of a solute, with a constant amount of dissolved material. The CMC represents the solubility limit for the monomer (or slightly aggregated e.g. dimer) surfactant, and above this concentration the excess surfactant is displaced from true contact with the bulk liquid into the micelle.

CMC can be determined by many different methods including the use of surface tension measurements (which will fall until the system reaches the CMC, and then should plateau), solubilisation methods, conductivity changes, light scattering experiments (as the micelles are larger structures which can scatter laser light), etc. NMR is a rich source of information about molecular structure and dynamics. NMR has been used to characterize molecules ranging in size from small organics to large macromolecules and proteins. NMR has also been used to determine the size/shape of the self-assembled systems by diffusion-ordered spectroscopy (DOSY). Landry et al<sup>108</sup>

studied the micellization process of sodium 8-phenyloctanoate in a deuterated aqueous solution, using  $^1\text{H-NMR}$  spectroscopy.  $^1\text{H-NMR}$  spectra, acquired for the sodium 8-phenyloctanoate before and after the critical micelle concentration (CMC) value, showed that large chemical-shift changes were observed for both the aromatic proton peaks and the peaks for the methylene protons near the terminal phenyl group. Kjellin et al<sup>109</sup> investigated several physico-chemical properties of three non-ionic surfactants. They used the Wilhelmy plate and NMR methods to determine the CMC of the different formulations. They noted that NMR measurements is a method which is less sensitive toward highly surface-active impurities that may affect surface tension measurements.

## 4.2 Formulations

The two different surfactants used: 2-Propylheptanol ethoxylate (Surf1, non-ionic) and Coco amidopropyldimethylamine (Surf2, cationic) were synthesized at AkzoNobel Surface Chemistry. Surf2 is made of four components: 80% Coco amidopropyldimethylamine, 7% propylene glycol, polydimethylsiloxane (defoamer) and 13% water. The active ingredient used was Tebuconazole.

The physico-chemical properties of the different formulations can be seen in Table 4.1. They were diluted with deionized water to a concentration of 1 g/L and 3 g/L, which is a common concentration of spray adjuvants.

A 25% SC Tebuconazole solution was made as follows: 1.14 g of Morwet D-425 (sodium salt of naphthalene sulfonate condensate) was dissolved in 150.28 g of water. Then, 48.57 g of Tebuconazole powder was added to it and homogenized for 90 s with Ultra Turrax and milled by the Mini mill up to a particle size distribution  $d(v0.5) < 3 \mu\text{m}$ . In this experiment, 35 min were needed to get  $d(v0.1) = 0.95 \mu\text{m}$ ,  $d(v0.5) = 2.49 \mu\text{m}$  and  $d(v0.9) < 6.88 \mu\text{m}$ .

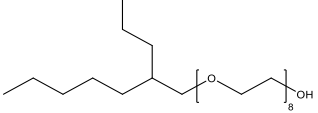
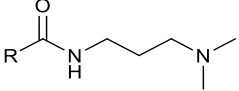
Formulation	Solubility in water (mg/L)	Density (kg m <sup>-3</sup> ) at 20°C	Viscosity dynamic (mPa s) at 20 °C	Water content (%)	Structure
Surf1	soluble	1021	70	< 1	
Surf2	dispersible	920	135	13	

Table 4.1: Physico-chemical properties of Surf1 and Surf2. R chain in Surf2 varies from C12–C18.

The tensiometer used to measure the surface tension of the solutions was described in Section 3.4. The experiments were repeated 5 times for each formulation. The time required to reach static surface tension is shorter for solutions at higher concentrations. This is simply because with more surfactants inside of the drop, the formed fresh air–liquid interface is covered by surfactants more quickly.

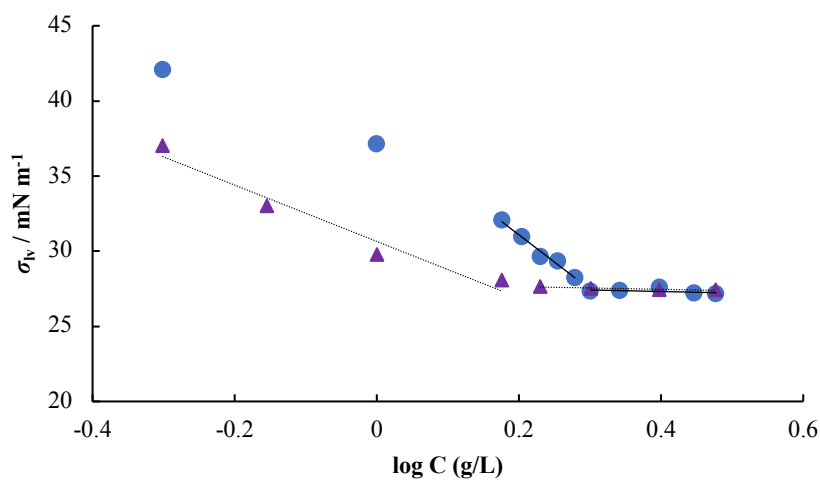
The properties of Surf1 and Surf2 in aqueous solutions were studied by <sup>1</sup>H-NMR (chemical shift and line shape) and NMR self-diffusion experiments. Samples for NMR measurements were made by increasing the concentration of surfactant solutions in D<sub>2</sub>O. The samples were equilibrated for at least 4 h. <sup>1</sup>H-NMR was also used to study the solubility of AI in surfactant solutions.

### 4.3 Surface tension

The slope of surface tension vs  $\ln C$  is proportional to the surface excess. The surface excess increases with concentration, but close to the CMC this increase is slow and the slope can be considered a straight line. The way the CMC is found is by drawing straight lines through the data above and below the kink in the  $\sigma$  vs  $\ln C$  plot and measuring the intersection of the two linear lines. Above CMC, the surface tension no longer

underwent significant change. For impure systems surface tension is not a very good way to calculate the CMC value. A plot of surface tension with respect to Surf1 and Surf2 concentration in deionized water is provided in Figure 4.1. The shape of the surface tension/log concentration plot can reveal information about surfactant purity, e.g. through curvature in the plot near the CMC or even a minimum in the surface tension.

a) Surf1



b) Surf2

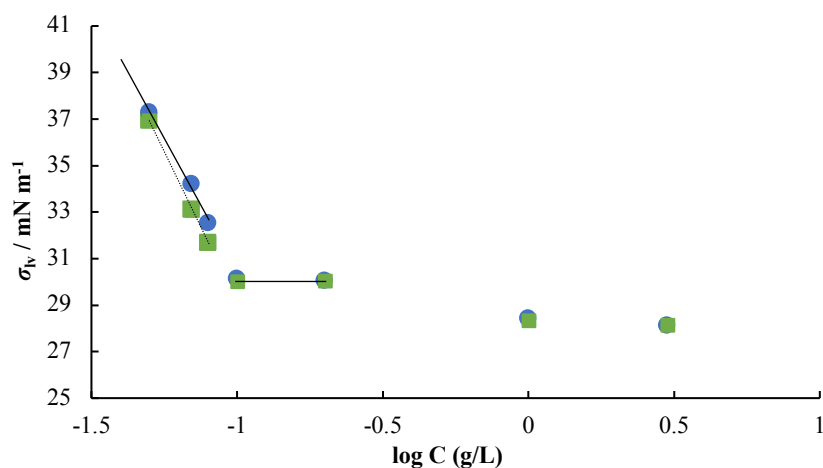


Figure 4.1: Surface tension at different concentrations for Surf1 (a) with (purple triangles) and without (blue circles) AI and Surf2 (b) with (green squares) and without (blue circles) AI.

Figure 4.1 shows the variation of the surface tension with increasing concentration of the surfactant solution. For both surfactants, the surface tension decreases as the concentration of the surfactant increases until it reaches a value where the surface tension is constant. The kink can be either due to the formation of micelles or because the surfactant reaches the solubility limit. The value of the kink is 2 g/L and 1.6 g/L for Surf1 without AI and with AI respectively and 0.1 g/L for Surf2 without AI and with AI indistinctly. The addition of AI to Surf1 decreased the values of the surface tension at concentrations below the kink and the value of CMC. This effect is caused by adsorption of the AI at the interface in the presence of the surfactant. The AI has only a small effect on the surface tension of Surf2. A further study of the presence of micelles in these two formulations will be described in Section 4.4.

#### 4.4 $^1\text{H-NMR}$ and Diffusion resolution in DOSY

$^1\text{H-NMR}$  spectra of Surf1 at various concentrations in  $\text{D}_2\text{O}$  at 25 °C are shown in Figure 4.2.

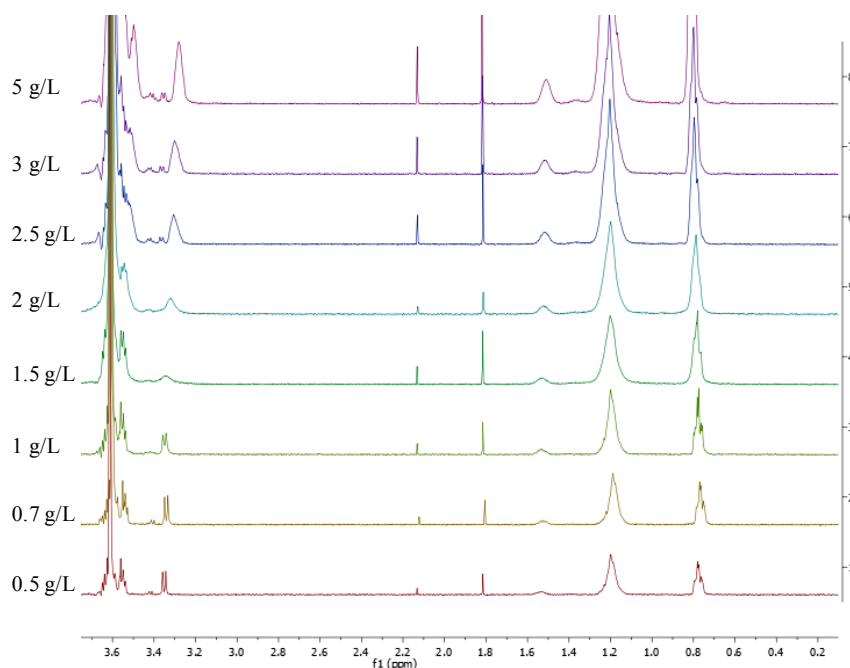


Figure 4.2:  $^1\text{H-NMR}$  spectra of Surf1 at various concentrations in  $\text{D}_2\text{O}$  at 25 °C.



The  $^1\text{H}$ -NMR spectra at concentrations below 1.5 g/L show a doublet at  $\delta = 3.31$  and a singlet at higher concentrations. This peak is assigned to the  $\text{CH}_2$  protons next to the ethoxylate chain. The merging and broadening of these two peaks results from aggregation of monomers and exchange of monomers between micelles and in bulk solution. Thus,  $^1\text{H}$ -NMR spectra give strong evidence about the formation of micelles for the non-ionic Surf1.

$^1\text{H}$ -NMR spectra of the cationic surfactant, Surf2, at various concentrations in  $\text{D}_2\text{O}$  at 25 °C are shown in Figure 4.3.

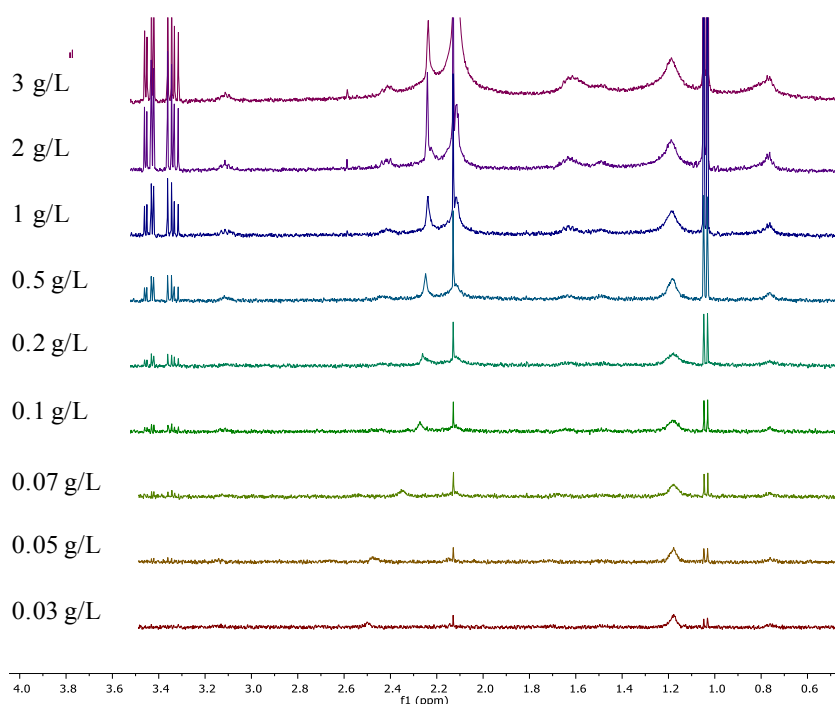


Figure 4.3:  $^1\text{H}$ -NMR spectra of Surf2 at various concentrations in  $\text{D}_2\text{O}$  at 25 °C.

$^1\text{H}$ -NMR spectra in Figure 4.3 do not show any change among all the concentrations of Surf2 other than changes in intensity. The formation of micelles cannot be determined for this formulation.

For surfactants of fast exchange between monomers and micelles in bulk solution, the observed chemical shift ( $\delta_{\text{obsd}}$ ) of the resonance peak can be expressed as the weighted mean of chemical shifts of the micelles and monomers at concentrations above their CMC's according to the pseudophase transition model<sup>110,111,112</sup> by the following equation:

$$\delta_{\text{obsd}} = (C_{\text{mon}} / C_{\text{T}})\delta_{\text{mon}} + (C_{\text{mic}} / C_{\text{T}})\delta_{\text{mic}} \quad \text{Eq. 4.1}$$

where  $\delta_{\text{mon}}$  and  $\delta_{\text{mic}}$  represent the chemical shifts related to the free monomers and to the monomers in micelles, respectively;  $C_{\text{mon}}$  and  $C_{\text{mic}}$  are the free surfactant concentration and surfactant concentration in micelles, respectively; and  $C_{\text{T}} = C_{\text{mon}} + C_{\text{mic}}$  is the total surfactant concentration. Below the CMC, the pseudophase transition model<sup>136</sup> predicts that  $\delta_{\text{mon}}$  remains constant and equal to  $\delta_{\text{obsd}}$ . Above the CMC, it is supposed that the free monomer concentration remains constant at the CMC, so Eq. 4.1 can be rewritten as

$$\delta_{\text{obsd}} = (CMC / C_{\text{T}})(\delta_{\text{mon}} - \delta_{\text{mic}}) + \delta_{\text{mic}} \quad C_{\text{T}} > \text{CMC} \quad \text{Eq. 4.2}$$

According to Eq. 4.2, a plot of  $\delta_{\text{obsd}}$  vs  $1/C$  at concentrations above and below the CMC should form two straight lines, and the point of intersection of these two lines is the CMC (Figure 4.4).

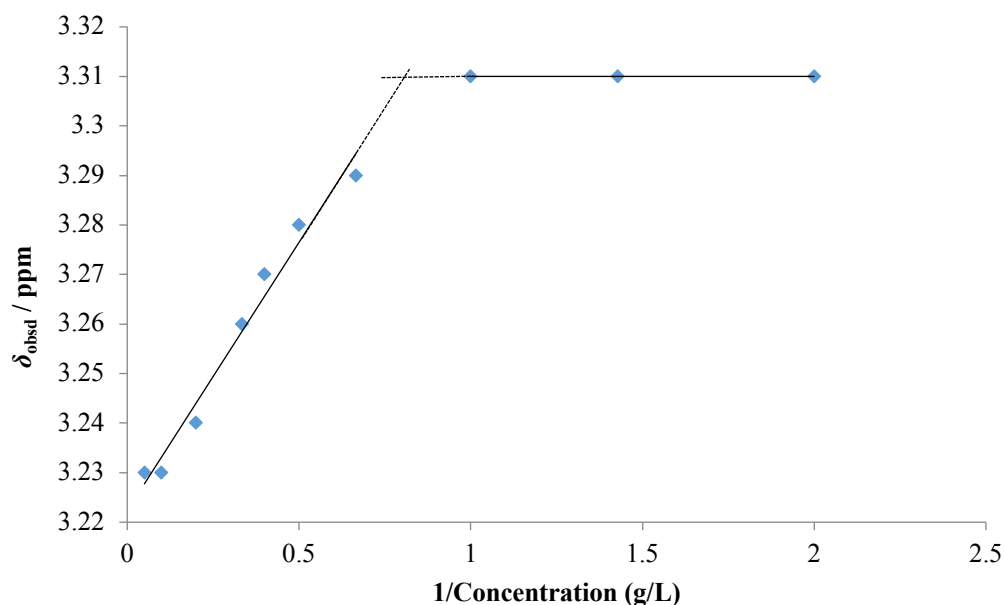


Figure 4.4: Variation of the  $\delta_{\text{obsd}}$  as a function of reciprocals of concentration in D<sub>2</sub>O at 25 °C.

According to Figure 4.4, the CMC for Surf1 is approx. 1.3 g/L. There is a variation of the CMC value when the two techniques are compared. There are always slight differences between different methods. Moreover, the formulations are blends and contain impurities.

The aggregation of surfactant monomers to form micelles produces marked changes in the environment and the dynamics of these molecules, which are revealed by changes in a number of NMR parameters, such as chemical shifts, relaxation rates, and diffusion coefficients of the system. The large intrinsic difference between the diffusion coefficients of surfactant monomers and micelles makes self-diffusion measurement a convenient and direct way for the determination of micellization. Figure 4.5 shows a DOSY spectrum containing Surf1 at 3 g/L.

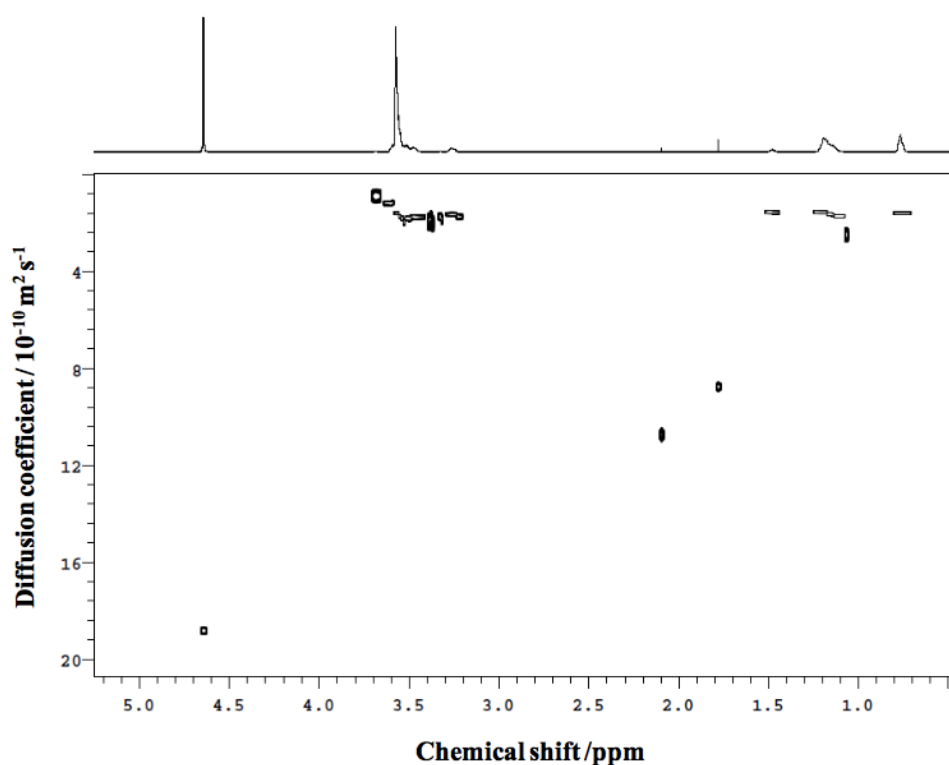


Figure 4.5:  $^1\text{H}$  DOSY spectrum of Surf1 at a concentration of 3 g/L.

Figure 4.5 shows 4 different distinct species. Each set of peaks with the same diffusion coefficient correspond to a different molecule. It is not clear if the signal of the species with the lowest diffusion coefficient belongs to one or two species or if the variations in  $D$  between peaks is due to the error of the measurement. The water content of the surfactant is shown as the biggest molecule with an average diffusion coefficient of  $18.69 \times 10^{-10} \text{ m}^2 \text{ s}^{-1}$ . It is likely that the other species in the sample come from unreacted raw materials, i.e. branched C10 alcohol and ethylene oxide.

The diffusion coefficient for Surf1 at each concentration is shown in Figure 4.6.

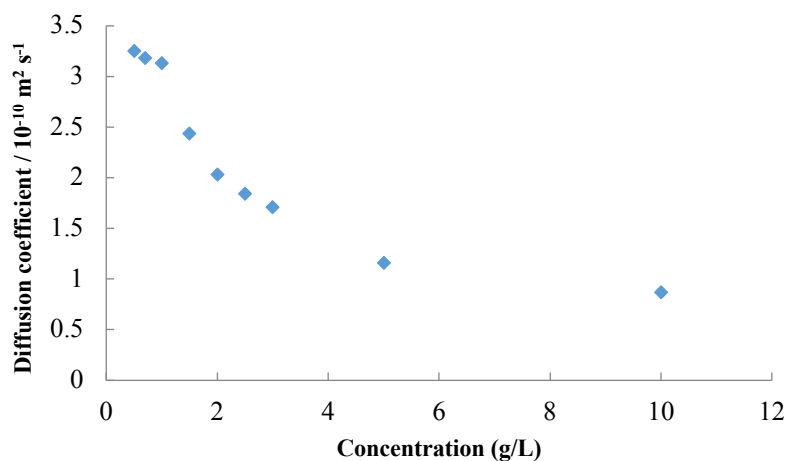


Figure 4.6: Variation of the diffusion coefficient of Surf1 molecules as a function of different concentrations in D<sub>2</sub>O at 25 °C.

The fact that the diffusion coefficient for the Surf1 decreases as the concentration increases, is very strong evidence that there are micelles. The diffusion coefficient decreases because there is a mixture of monomers and micelles and micelles diffuse more slowly and they are larger than monomers.

The diffusion coefficient for the molecules of Surf2 at different concentrations is shown in Figure 4.7.

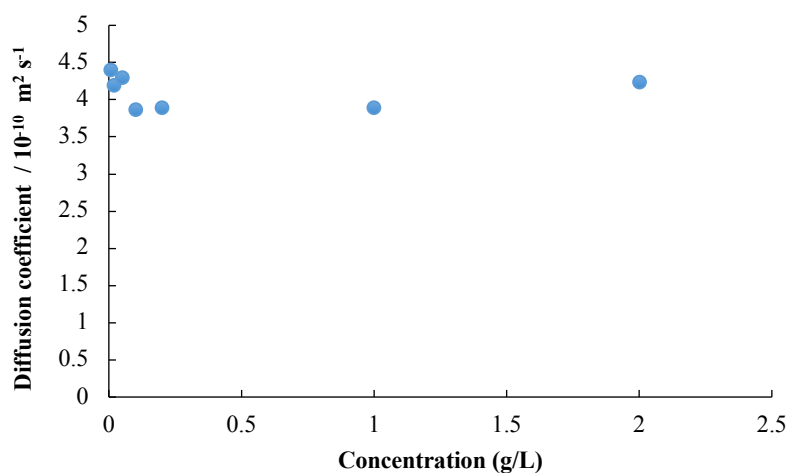


Figure 4.7: Variation of the diffusion coefficient of Surf2 molecules as a function of different concentrations in D<sub>2</sub>O at 25 °C.

The diffusion coefficient of Surf2 does not change with concentration. The diffusion coefficient for a 50 g/L solution was measured in order to see any change and the value

was very similar. A diffusion coefficient of  $4 \times 10^{-10} \text{ m}^2 \text{ s}^{-1}$  it is characteristic of small molecules, so the presence of micelles cannot be detected.

## 4.5 Solubility of AI in nonionic surfactant solutions

Surfactants spontaneously associate with each other in the process of micellization to form organized, dynamic chemical structures having such geometrical configurations as spheres or spheroids<sup>113</sup>. The hydrophobic portion of each molecule in the micelle is directed inward, toward the centre of the aggregate, forming with the other hydrophobic moieties a liquid core. The central region of the micelle thus constitutes a hydrophobic pseudophase that is distinct in its properties from the polar solvent<sup>114</sup>.

Increasing the solubility of an insoluble or poorly soluble organic substance in a surfactant solution has been widely studied for many decades. According to Rosen<sup>115</sup>, micellar solubilization can be defined as the spontaneous dissolution of a substance by reversible interaction with the micelles of a surfactant in water to form a thermodynamically stable isotropic solution.

A measure of effectiveness of a particular surfactant in solubilizing a given solubilize can be defined as the number of moles of organic compound solubilized per mole of surfactant added to the solution<sup>116</sup>. Micellar solubilization studies were conducted with Surf1 and AI. Solutions were made up containing different dilutions of surfactant while maintaining a constant amount of AI to allow a quantitative analysis to be performed. This analysis monitored the solubility of AI when the surfactant concentration was increased. In each experiment, the surfactant solutions were diluted with water in a 100 mL volumetric flask, the AI was added, and more water added up to the volume line. The solutions were mixed using a magnetic stirrer bar for 66 h. At this point the solutions were filtered to remove undissolved AI particles by 1) filter paper (100  $\mu\text{m}$ ) and 2) syringe filter (0.45  $\mu\text{m}$ ). The solution was transferred to a round-bottomed flask and the water was then removed by rotary evaporation to leave a

viscous liquid residue. This solution was dissolved in dimethyl sulfoxide-d6 (DMSO) and analysed by  $^1\text{H}$  NMR.

For each concentration, the peak areas were integrated and normalised using a surfactant peak to obtain a constant relative surfactant concentration (Figure 4.8).

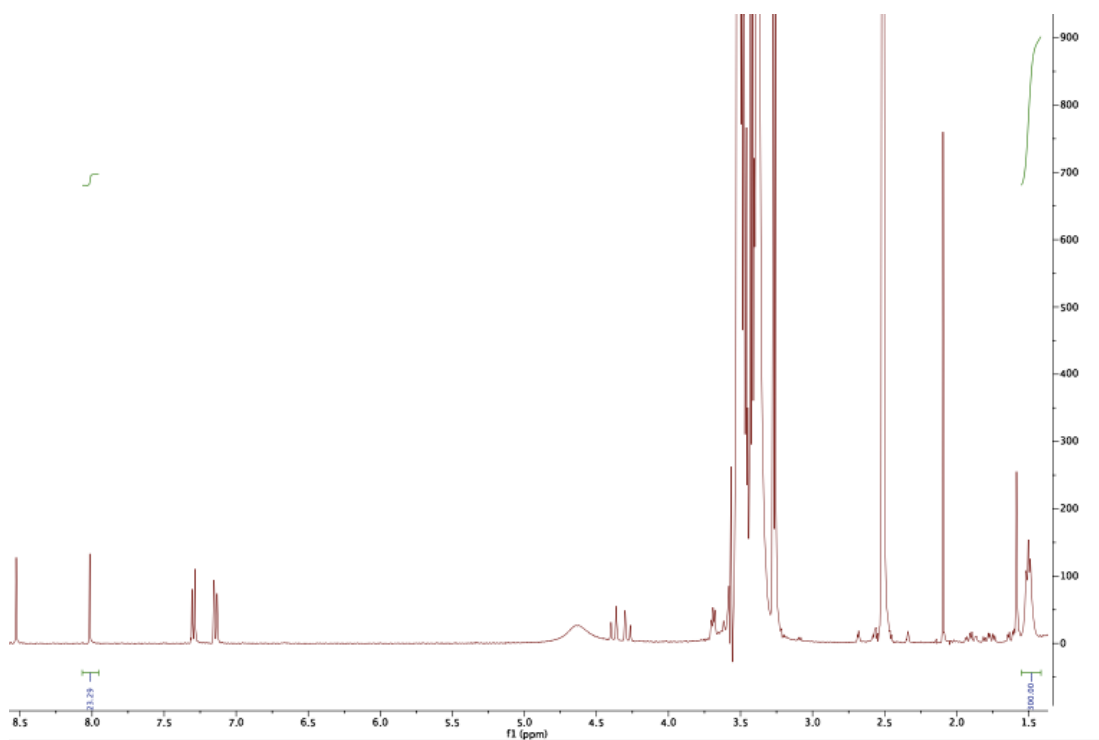


Figure 4.8:  $^1\text{H}$  NMR spectrum of Surf1 3 g/L + AI. Area surfactant peak ( $\delta = 1.50$ ) = 300 and area AI peak ( $\delta = 8.01$ ) = 23.29.

Figure 4.8 shows the  $^1\text{H}$  NMR spectrum of Surf1 3 g/L + AI, where normalized peaks of both compounds were compared. This could be done using the known surfactant concentrations and comparing the peaks that correspond to the same number of hydrogens. The surfactant (septet,  $\delta = 1.50$ ) was then compared to the area of an AI peak (singlet,  $\delta = 8.01$ ) to obtain a series of data points allowing the quantitative determination of AI concentration in each solution (Figure 4.10). Figure 4.9 shows the hydrogens selected for the quantitative analysis in both surfactant and AI.

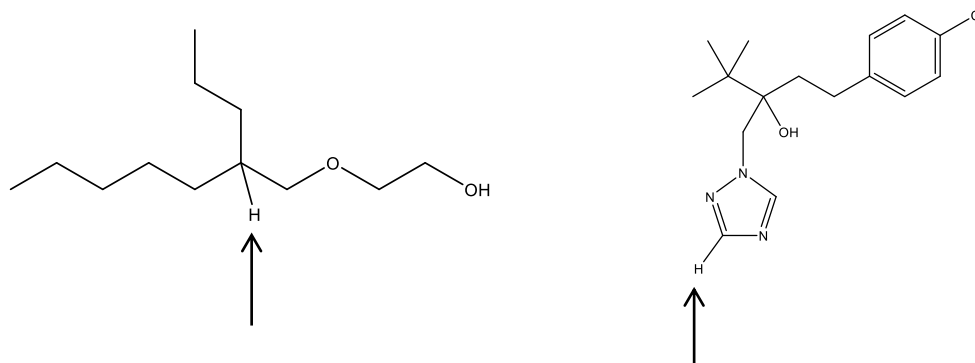


Figure 4.9: Selected hydrogens for the NMR quantitative analysis

In the presence of excess AI, the molar solubilisation ratio may be obtained from the slope of the curve.

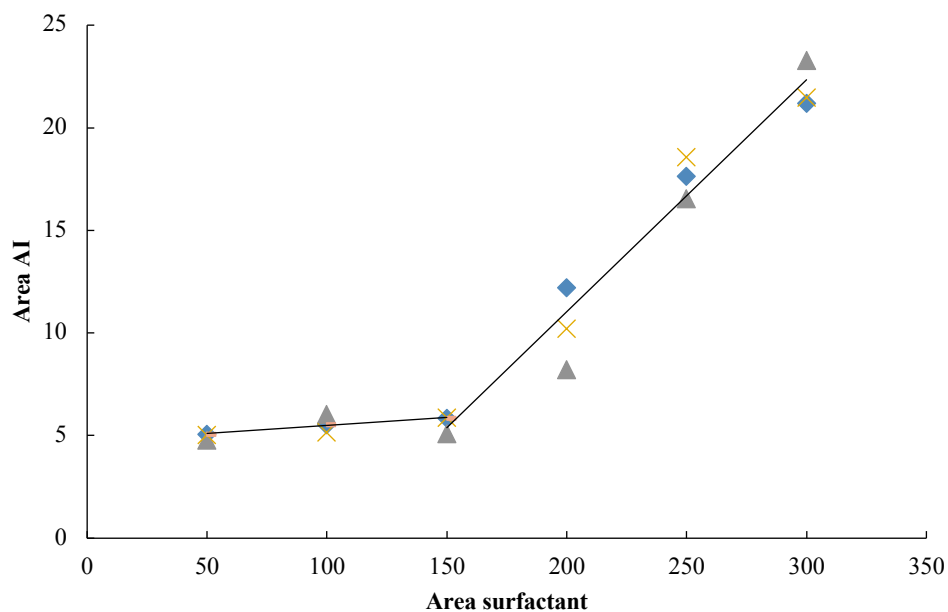


Figure 4.10: Peak area in  $^1\text{H-NMR}$  for selected peaks for the AI over the peaks of the surfactant.

Figure 4.10 shows three measurements for the quantitative determination of AI concentration in Surf1 solutions. The concentrations tested are above and below the CMC. The interception of both lines is the CMC. Below CMC, the constant solubility of AI is due to the limited solubility of the AI in water while for concentrations above the CMC the solubility of AI increases with the concentration of the surfactant. The

slope of the graphs can be used to calculate  $[AI] / [surfactant]$  in micelles, so it can be approximated that 1 moles of AI are soluble in 10 moles of Surf1.

In Surf2, there is no presence of micelles, so this kind of experiments would show the solubility of the AI in the emulsion droplets. Moreover, the filtration step would remove the emulsion as well as the excess of AI.

Once the droplet is dried on the leaf, just surfactant and AI are left on the deposit and Tebuconazole has to diffuse through the surfactant in order to get through the leaf. Solubility of AI in neat surfactant was also tested. 2 g of neat Surf1 was added to a 2 g of solid AI. Samples were centrifuged for 1 h at 25 °C. An aliquot of the supernatant was mixed with DMSO before running the  $^1H$ -NMR spectrum (Figure 4.11).

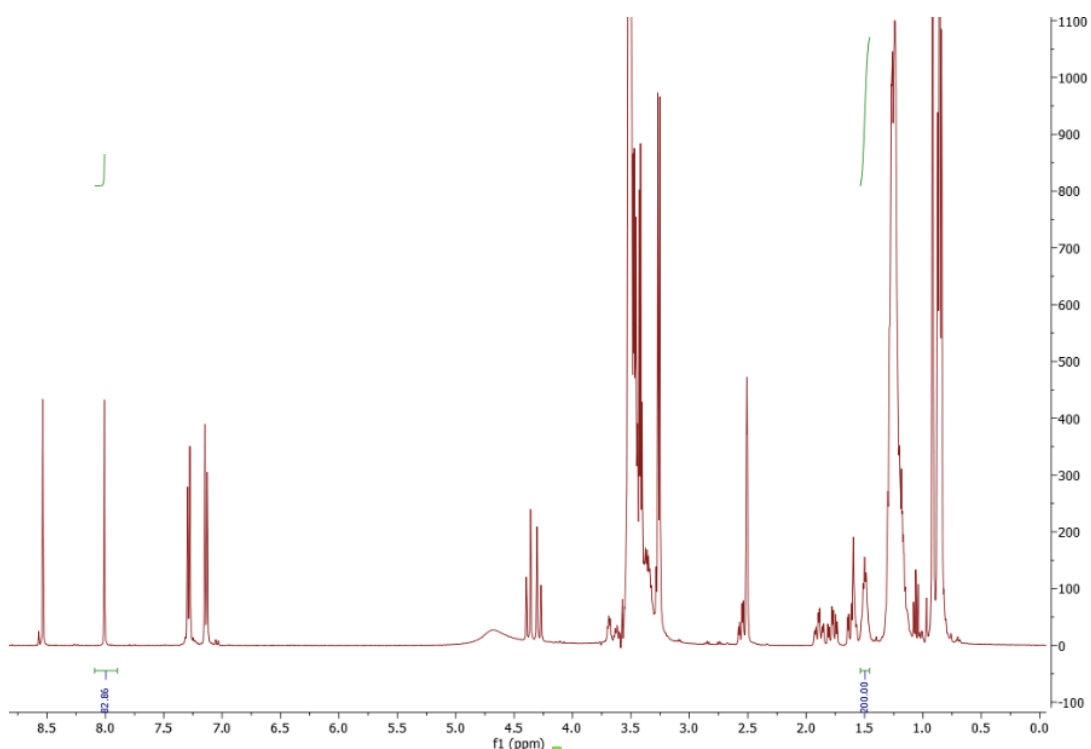


Figure 4.11:  $^1H$  NMR spectrum of neat Surf1 + excess amount of solid AI. Area surfactant peak ( $\delta = 1.50$ ) = 200 and area AI peak ( $\delta = 8.01$ ) = 82.86.

The  $^1H$ -NMR spectrum of 2 g of solid Tebuconazole in 2 g of neat surfactant showed a ratio of AI/surfactant peak of 83:200. This peak ratio is higher than in Figure 4.10, where the peak ratio is 1:10. This means that the solubility of Tebuconazole is higher in the neat surfactant than the micelles, and this is favourable for the application.



## 4.6 Summary

Surface tension and NMR experiments were combined in order to study the physico-chemical properties of two formulations described in this thesis. The tensiometer measured the surface tension of Surf1 and Surf2 at different concentrations with and without the addition of AI. In some cases, this technique can be used to estimate when micelles are formed. Also, the surface tension of a solution provides information about the evaporation mode since surface tension and spreading are correlated as it will be shown in Chapter 5. The addition of particles to the solution can also affect the surface tension. In Surf1, the addition of AI decreased the surface tension compared to the case where there was no addition. There might have been some interaction of the AI at the air-liquid interface. Surface tension measurements are used as an approximation for the determination of the CMC, but these formulations are mixtures so the use of the other methods were required to calculate a more accurate number. By studying the variation of the chemical shift obtained by  $^1\text{H-NMR}$  at different concentrations, the CMC can also be evaluated.

DOSY was used to study the diffusion of molecules as the concentration of the solution was increased. It can be interpreted that, for solutions in which as the concentration increases, the diffusion coefficient is slower, this is due to the assembly of monomers forming micelles. It can be also seen that the  $^1\text{H-NMR}$  spectra for Surf1 at concentrations 0.5–1 g/L showed a doublet at the same frequency ( $\delta = 3.31$ ). However, at higher concentrations the split doublet resonance peaks begin to merge together because of the possible formation of micelles. There was no difference in the diffusion coefficient for Surf2 even at very high concentrations, so it can be concluded that there are not micelles.

Micellar solutions can be used to solubilize hydrophobic substances in their hydrophobic core. In this thesis, the capacity of Surf1 to dissolve AI was studied. It has been shown that 10 moles of this particular formulation is capable to dissolve 1 mole of AI. AI molecules in agrochemical solutions are desired as they will penetrate the cuticle of the leaf after the deposition of the droplets on the surfaces of leaves.

When droplets dry on the leaf, just surfactant and AI remain on the deposit so the diffusion of Tebuconazole will be through the surfactant film. It has been shown that the solubility of Tebuconazole is higher in neat surfactant than in micelles and this is favourable for the application.

# Chapter 5

## 5. Residual droplet patterns on substrates with different wettabilities and evaporation modes

### 5.1 Introduction

The formation of a pattern during the drying of drops on surfaces is a phenomenon that is currently attracting much attention. It is well known that different formulations can give very different deposits on the same surface and also the final deposit changes on different surfaces when the same formulation is applied. In agrochemical applications, one of the assumptions for a good uptake of the AI is related to the way the surfactant and the AI are associated on the surface when the droplet dries out<sup>5</sup>. Surfactants are added to agrochemical formulations in order to enhance the passage of the AI through the cuticle of the leaf since the surface of the leaf is an almost impenetrable barrier for the AI alone. It is believed that to be effective, AI and adjuvant have to end up in the same position when the droplet dries out on the surface of the leaf, though firm evidence is lacking.

The action of a drop hitting a surface is a complex process that includes droplet impact, rebound or retention and spreading and is influenced by interactions among many controllable and uncontrollable variables. These variables include the physical and chemical properties of the spray solutions, the droplet size and velocity, the sprayer travel speed, the droplet trajectory before impact, the leaf surface characteristics, the ambient air temperature, the relative humidity, the wind velocity and the local microclimate turbulence.

Droplet size is always used as one of the most important parameters influencing pest control. Droplets should be large enough to deposit on the target after some evaporation during transportation, but should also be small enough to provide sufficient pesticide coverage on the target. Using large droplets can reduce drift potential but it can reduce the control efficiency, resulting in excessive pesticide use. The droplet volume was fixed to 1.5 nL for all the experiments.

The physical parameters that determine the outcome of an impacting drop are the inertial, viscous and capillary forces acting on the drop as it collides with the surface. The inertial forces result from the kinetic energy of the drop, and are determined by the size of the drop, density and speed. Meanwhile, the fluid viscosity of a drop governs viscous dissipation, and the capillary force (i.e. surface tension) establishes the energy that is required to deform the drop. The dimensionless Reynolds,  $Re$ , and Weber,  $We$ , numbers are constructed from the physical parameters of the system, and are used to characterize drop impact by gauging the competition between the inertial forces, relative to the viscous dissipation and drop deformation. For drop impact these numbers are defined in the following way:

$$Re = \frac{\textit{inertial}}{\textit{viscous}} = \frac{D_f \rho v_d}{\eta} \quad \text{Eq. 5.1}$$

$$We = \frac{\textit{inertial}}{\textit{capillary}} = \frac{D_f \rho v_d^2}{\sigma} \quad \text{Eq. 5.2}$$

where  $D_f$  is the diameter of the droplet in flight,  $v_d$  the drop impact velocity,  $\sigma$  the fluid surface tension,  $\rho$ , the fluid density and  $\eta$  the solution viscosity.

When droplets are delivered to targets, they will experience the process of spreading and evaporation. The process will vary with droplet size, leaf surface fine structure, physical properties of formulation, and weather conditions. Wettability control of evaporating sessile droplets through the employment of surfactants can be realized simply and effectively based on their surface-active nature. The use of surfactants improves chemical coverage on leaves, removes air films between spray and leaf surface and reduces surface tension on leaves. Droplet adhesion, spreading area and

retention on leaf surfaces can also be increased in pesticide droplets containing the surfactant. Understanding the evaporation and spreading process of pesticide droplets could be used for a better utilization of the pesticides to increase the foliar application efficiency.

The single constituents of a mixture of substances that have distinct physico-chemical properties, such as agrochemical solutions, might have a specific distribution pattern inside the spread area. The least soluble compounds might separate from the solution first, whereby the characteristics of the final deposit depend on the solubility of the components, their affinity for the leaf surface and the other materials in the spray mixture<sup>117</sup>. Thus, association between the AI and the adjuvant is not always ensured. The concentration of the adjuvant may influence its association with the AI.

The possible separation between the AI and the adjuvants was hypothesized several years ago, mainly based on visual observations of images using SEM<sup>118,119</sup>. The final proof was sought using radiolabelled or bromide-labelled adjuvants<sup>120</sup>, although this was disregarded as manipulation of the molecules was cost-intensive and it risked changing their characteristic properties and behaviour on surfaces. Very recently, fluorescent dyes have been used as substitutes for active ingredients to elucidate the spatial separation between two compounds within the spread area of the droplet<sup>5,121,122</sup>.

One of the most common obstacles for some applications is the suppression of the CRE that might be useful to get a more uniform deposit where, for example in agrochemical solutions, the concentration of the surfactant and AI would be more evenly spread-out on the surface. CRE can be suppressed through three different physical strategies: i) preventing the pinning of the CL by minimizing the hysteresis that will facilitate smooth receding of the CL, ii) disturbing the capillary flow towards the CL for example by surface tension gradients or iii) preventing the particles being transported to the droplet edge by the capillary flows by particle-particle interactions and/or the interaction of particles with the solid-liquid interface and liquid-gas interface.

The evaporation of sessile droplets depends on the properties of the fluid and on the ambient atmosphere (e.g. temperature and relative humidity), but is also influenced by the characteristics of the substrate such as its chemical composition and physical structure. The first part of this chapter focuses on the effect of the wetting properties of the substrate on the evaporation of water sessile droplets. The evaporation characteristics of a droplet on the hydrophilic surface are classified with respect to the phenomenon of self-pinning and on the hydrophobic surface case that has three different stages: constant contact area stage, constant contact angle stage, and mixed stage. Later on, evaporation characteristic for surfactant solutions at different concentrations with and without the addition of AI are described. The last part of the chapter studied the effect of relative humidity and the temperature of the substrate, the possibilities of suppressing the CRE and obtaining more uniform deposits and the modification of the deposit by adding what are called “Superspreaders”.

## 5.2 Experimental

Droplets with a fixed volume, 1.5 nL, of high purity water (MilliQ), surfactant solutions or surfactants + AI solutions were deposited onto the substrate as described in the experimental section (Chapter 3, Section 3.3). Glass microscope slides were prepared by silane treatment in order to increase the hydrophobicity of the substrates with a range of wettabilities. Advancing and receding angles for water and different formulations are listed in Table 5.1 and 5.2 respectively. The experiments were performed at room relative humidity (38–40%) and at room temperature. However, for some of them, the temperature of the substrate and *RH* was varied in order to study their effect on the evaporation mode and morphology of the final deposit.

The variables used in this thesis were: four different surfaces, three surfactant solutions (Table 5.2), the use of AI crystals, three *RH* conditions (23, 50, 80%) and three different temperatures of the substrate (10, 20 and 30 °C), two additives (Laponite and silica particles) and two “Superspreaders” – Silwet Gold and Capstone® FS30.

Although six surfactants were studied, primary attention in this thesis is on two different formulations: an alkyl ethoxylated surfactant (Surf1) and an amidoamine-based surfactant (Surf2). A third formulation, a tallow amine ethoxylate, is also briefly discussed. The contact angle of a water droplet on a surface was always used to determine the wettability of the substrate at the beginning of each experiment to confirm the homogeneity on the substrate surface.

### 5.3 Water droplets on hydrophilic and hydrophobic substrates

Figure 5.1 shows the residual deposit for a water droplet on a hydrophilic glass substrate and on three different hydrophobic silane-modified glass substrates. PS particles were used as tracer particles to image the internal flows and visualize the deposit.

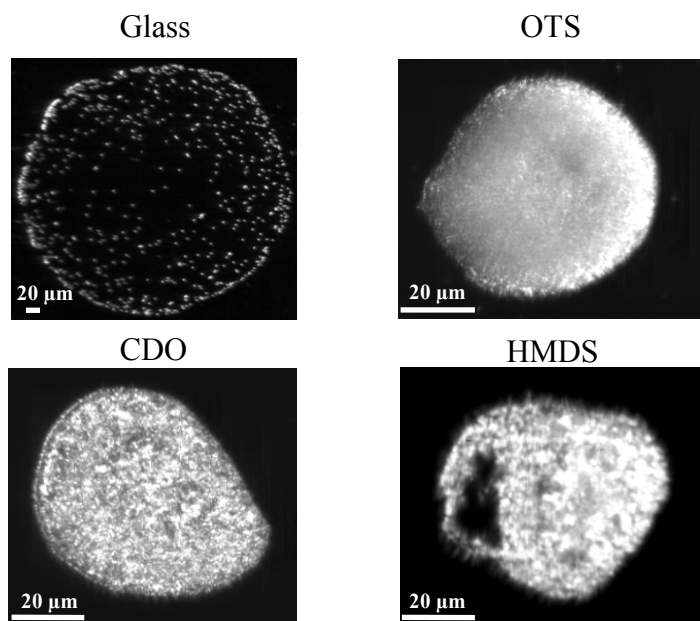


Figure 5.1: Deposition patterns of water droplets with PS particles on different substrates: glass, OTS, CDO and HMDS.

Depending on the hydrophobicity of the surface, two different types of behavior of the CL can be observed. For water droplets on a glass substrate, which is hydrophilic, the initial contact angle is  $36^\circ$  and pinning of the CL is observed during the droplet lifetime. Most of the tracer particles are deposited near the CL and very few particles occupy the centre of the drop. However, when the substrate is changed to a more hydrophobic one the result is completely different. The initial contact angles for water droplets were  $95^\circ$  for OTS,  $88^\circ$  for CDO and  $73^\circ$  for HMDS. In all cases the CL starts to recede at the beginning of the evaporation process and ring stain is not seen, with most of the particles deposited in the center of the droplet.

The evaporation process for a water droplet on hydrophobic substrates is composed of three main stages (Figure 5.2):

- (1) The initial contact angle  $\theta$  decreases where the diameter of the droplet,  $D$ , remains constant.
- (2) The contact angle  $\theta$  remains constant while the diameter of the droplet,  $D$ , decreases.
- (3) Both  $\theta$  and  $D$  decrease until the droplet completely disappears.

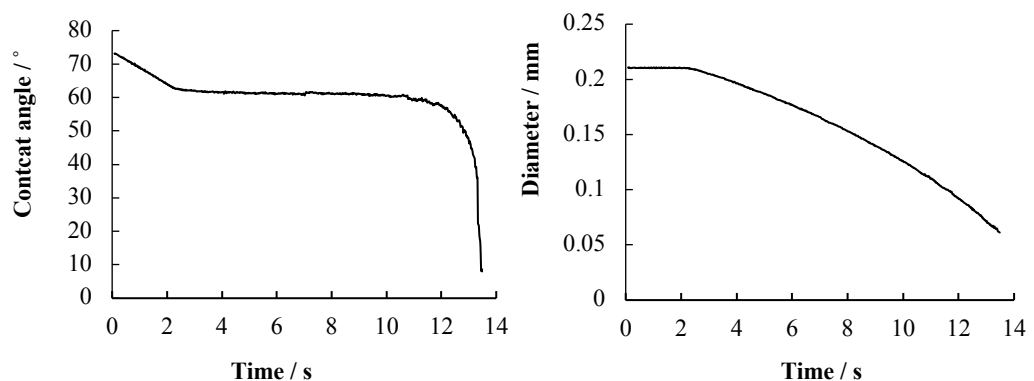


Figure 5.2: Stages of the evaporation process for a water droplet on HMDS.

As can be seen in Figure 5.2, when a droplet of water is deposited on a silane-modified glass substrate, HMDS, the initial contact angle is  $73^\circ$ . During almost the first three seconds of the evaporation, the droplet evaporates and the CL remains pinned and the contact angle decreases from the  $\theta_a$  to the  $\theta_r$  due to hysteresis. After that, the contact angle is constant while the diameter decreases for ten more seconds and at the end both



parameters decrease until a residual pattern is left on the surface. For all the hydrophobic surfaces used in this thesis the behavior is similar. Table 5.1 shows that the higher the contact angle, the less the *CAH*.

Water	$\theta_a$	$\theta_r$	<i>CAH</i>
OTS	95	89	6
CDO	88	79	9
HMDS	75	63	12

Table 5.1: Advancing and receding contact angles for 3- $\mu$ L droplets of water. *CAH* = Contact angle hysteresis =  $\theta_a - \theta_r$ .

The results obtained for the hydrophilic surface show that the CL remains pinned during the whole process of evaporation since  $\theta_r = 0$ . In agreement with previous studies<sup>123</sup>, this pinning regime leads to a linear evolution of volume or mass in time, hence a constant evaporation rate. However, on the hydrophobic substrates, the CL recedes steadily. These results for hydrophobic surfaces resemble the expected evaporative behavior of droplets on ideal surfaces where hysteresis effects are important for ca. 3 s. The diameter receded during most of the droplet lifetime.

The evaporation time for water on glass is 7 s, so it is worth noting that the evaporation time for hydrophilic surfaces is less than hydrophobic surfaces for the same initial volume. As mentioned in Eq. 2.9, for a given fixed volume, the rate of evaporation ( $dm/dt$ ) is proportional to the radius; the larger the radius is, the shorter the drying time.

## 5.4 Aqueous surfactant solutions on hydrophobic substrates

Different surfactant solutions at two different concentrations: a tallow amine ethoxylate, an alkyl ethoxylate (Surf1) and an amidoamine-based (Surf2) surfactant solutions at 1 g/L and 3 g/L, were tested to study the different modes of evaporation on three different hydrophobic surfaces. For the tallow amine ethoxylate, optical images of the final deposit are shown. For Surf1 and Surf2, SEM was used to look at the morphology of the final deposit.

### a) Tallow amine ethoxylate

The addition of the tallow amine ethoxylate surfactant solution at a concentration of 1 g/L (Figure 5.3, upper images) changed the resulting deposition. At 1 g/L on OTS, the CL depinned for several seconds before total evaporation, leaving a ring stain. For CDO and HMDS substrates, the CL was pinned for the majority of the evaporation but the CL only started to recede slightly in the moments before the total evaporation. The final deposit was also considered a ring stain as the particles were drawn to the outside by capillary flows.

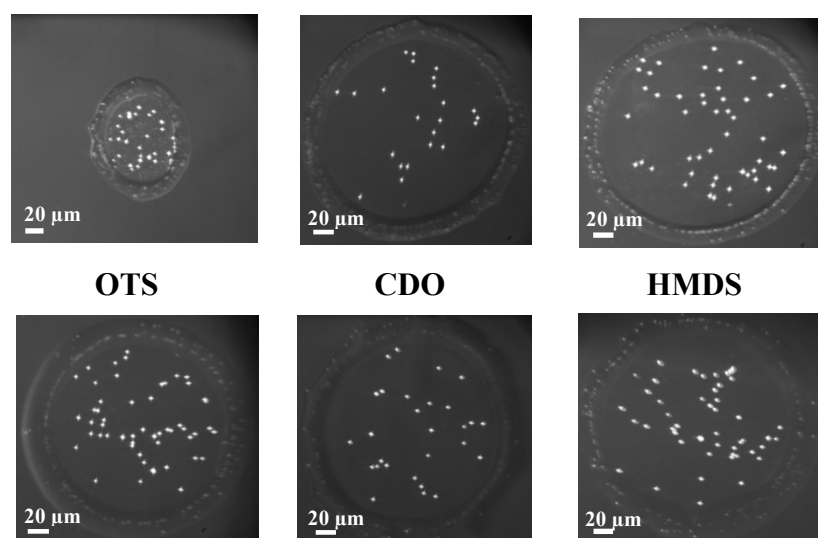


Figure 5.3: Deposition patterns of tallow amine ethoxylate at two different concentrations on different substrates OTS (left), CDO (middle) and HMDS (right): 1 g/L (upper images) and 3 g/L (lower images).

At higher concentration of the tallow amine ethoxylate surfactant solution (3 g/L) (Figure 5.3, lower images), the deposition pattern changed again. All three substrates showed a ring stain. The CL on CDO receded slightly whereas HMDS and OTS appeared pinned throughout. It is interesting to note that for OTS substrate that CL pinning was only seen for the higher concentration of surfactant, whereas for a lower concentration the droplet shrunk and a smaller deposit was formed at the end (Figure 5.4). The other two substrates showed the same ring stain for each concentration. For all of the substrates, surfactant left was observed around the deposit.

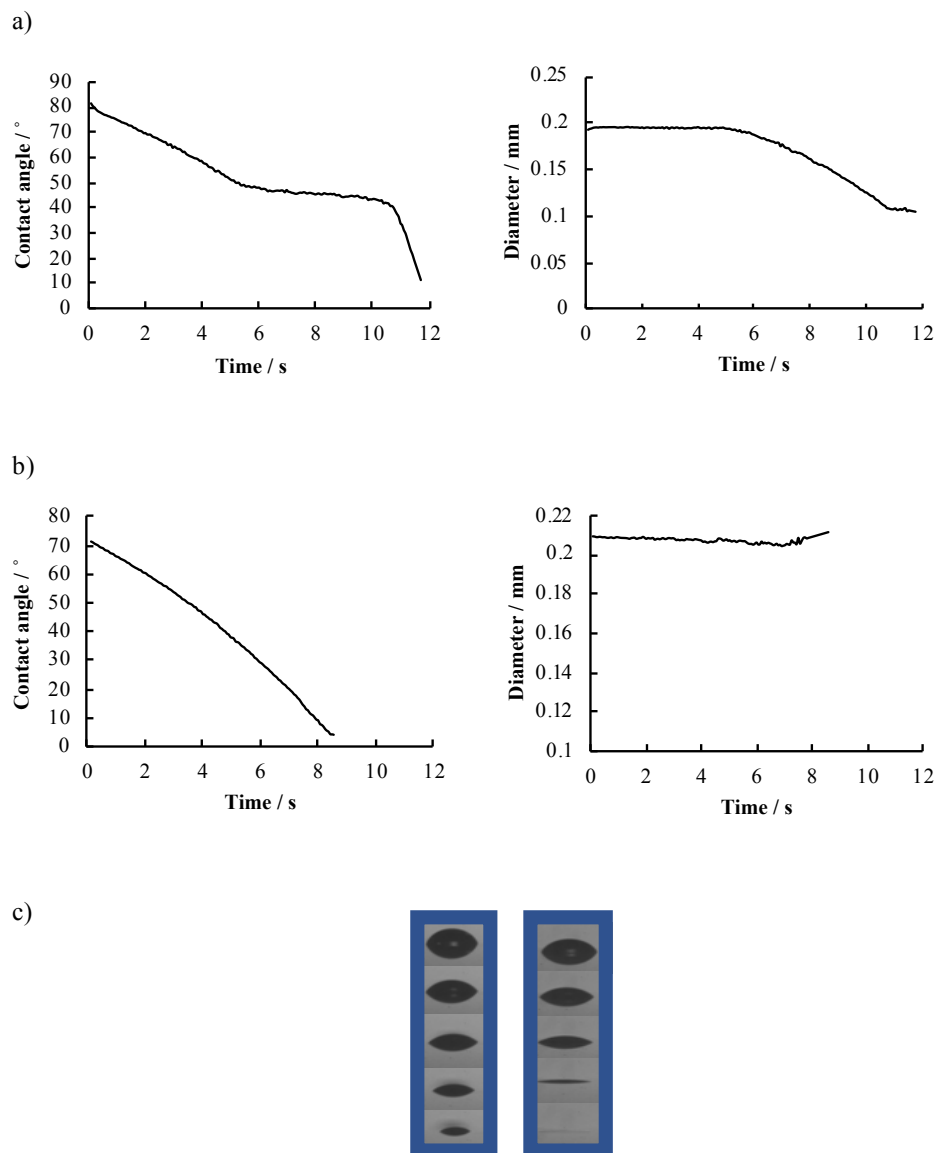


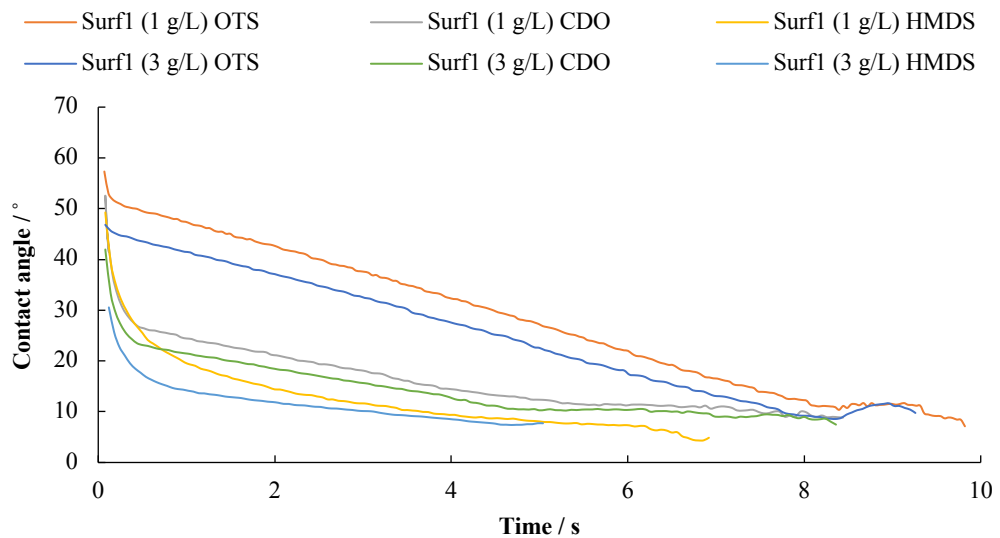
Figure 5.4: Evaporation process for a tallow amine ethoxylate surfactant solution on OTS substrate at two different concentrations: a) 1 g/L , b) 3 g/L and c) images of the drop side profile for a tallow amine ethoxylate solution: 1 g/L (left) and 3 g/L (right).

b) Alkyl ethoxylate surfactant (Surf1)

For the alkyl ethoxylate surfactant at 1 g/L on OTS the CL was pinned but it started to dewet within the droplet (Figure 5.5). At the end of the evaporation some of the particles moved very fast to form a semicircular deposit. For CDO and HMDS, after the spreading was completed, a pinned CL was observed. However, at the end of the evaporation, the particles at the center of the droplet started moving very fast to one of the edges of the droplet.

For the alkyl ethoxylate surfactant at 3 g/L on OTS the particles in the middle of the droplet moved faster to one side of the droplet forming a semicircular deposit. For CDO and HMDS, similar behavior was observed at both concentrations. The spreading continued longer on HMDS than on OTS or CDO.

At both concentrations the spreading continued for longer on HMDS than on OTS or CDO.



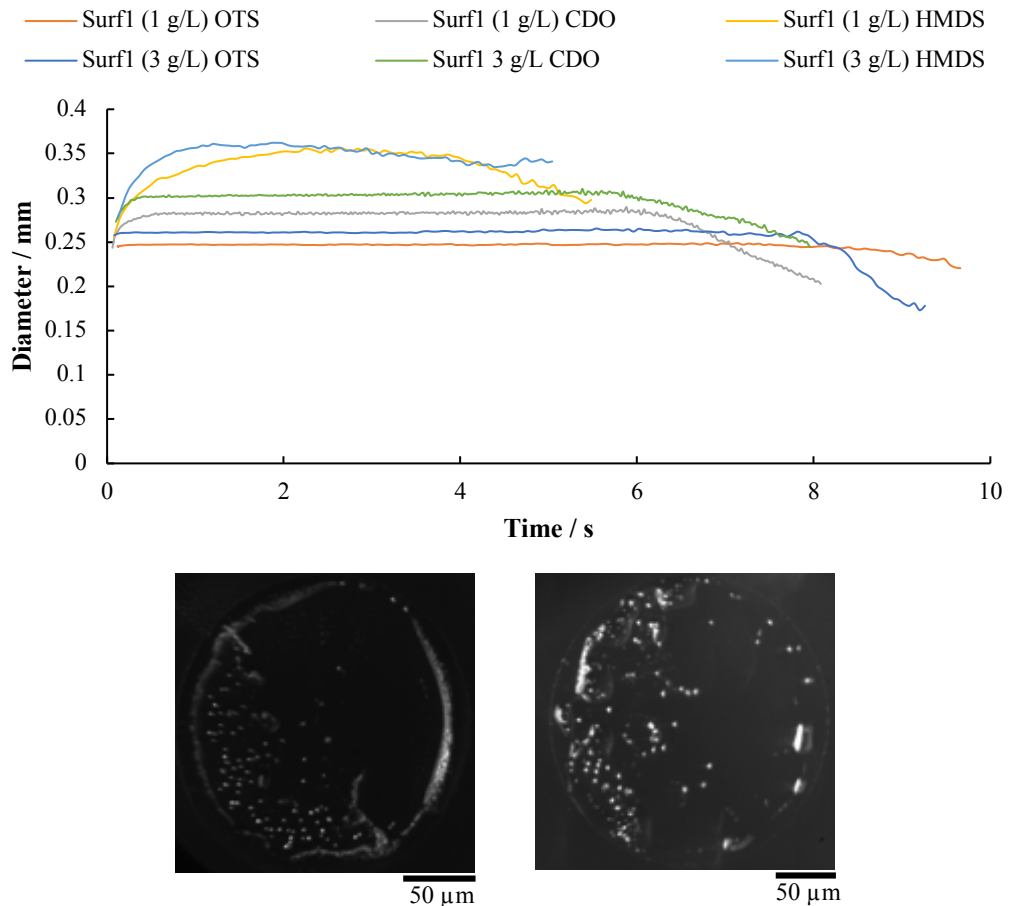


Figure 5.5: Progression of contact angle and diameter of Surf1 at 1 g/L and 3 g/L on three substrates with different wettabilities. Optical images for Surf1 at 1 g/L (left) and 3 g/L (right) on OTS.

### c) Amidoamine-based surfactant (Surf2)

For the amidoamine-based surfactant at 1 g/L, on OTS most of the particles moved to the edge, showing a pinned CL from start to the end of the evaporation. On CDO and HMDS, the same behavior was seen as for OTS but a higher spreading was seen. A slight depinning of the CL was seen at the end of the evaporation (Figure 5.6).

For the amidoamine-based surfactant at 3 g/L on OTS and CDO the same behavior was seen as with the lower concentration of the surfactant. However, on HMDS no shrinking was observed and a pinned CL was seen during the evaporation process after spreading.

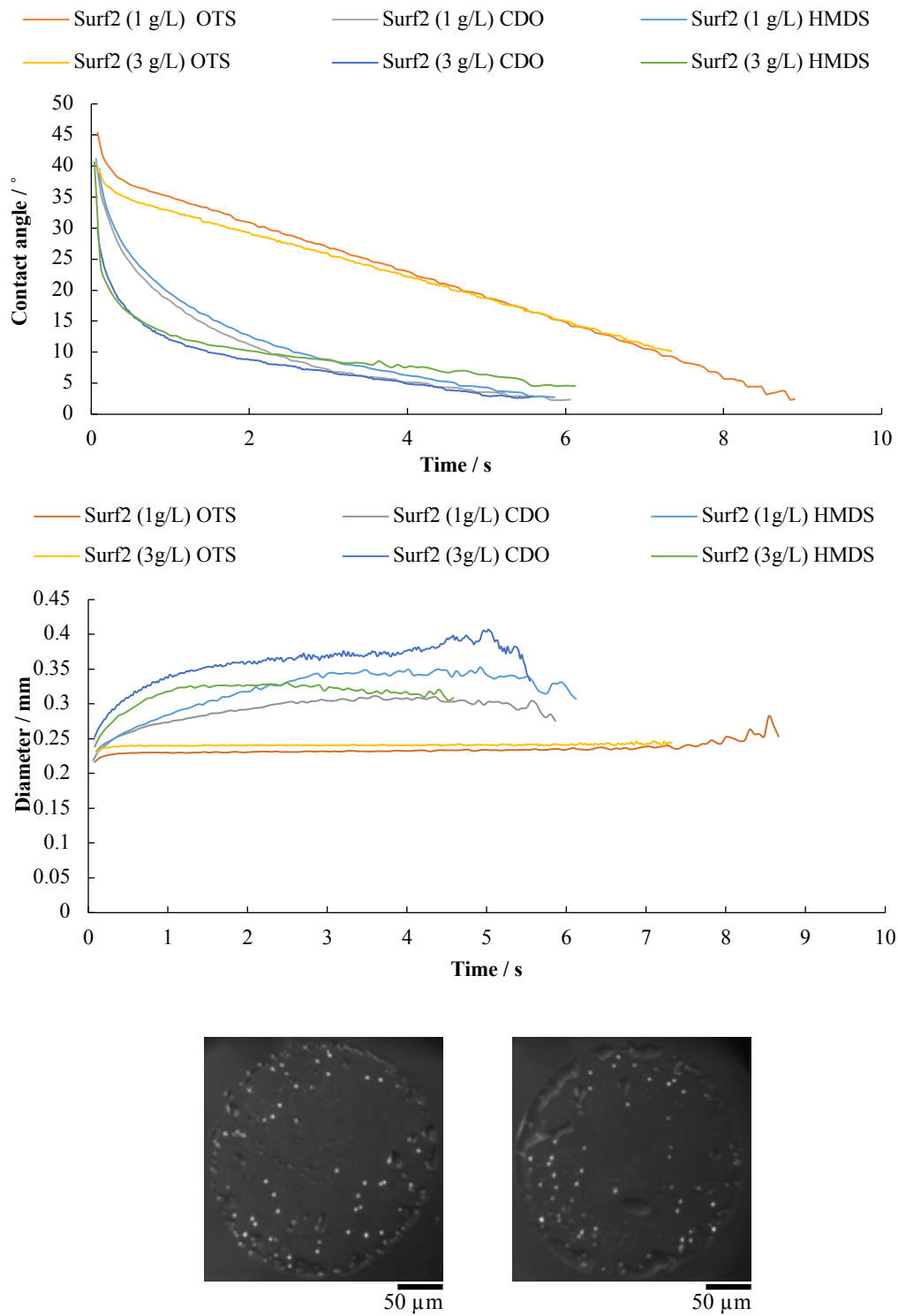


Figure 5.6: Progression of contact angle and diameter of Surf 2 at 1 g/L and 3 g/L on three substrates with different wettabilities. Optical images for Surf2 at 1 g/L (left) and 3 g/L (right) on OTS.

Figure 5.5 and 5.6 show the evaporation profile of Surf1 and Surf2 on substrates with different wettabilities and the typical morphology of the deposits at the end of the evaporation on OTS. The data were analyzed until the errors in measurements became unreasonably high due to the small volume. During the spreading stage immediately after deposition, both the contact angle and diameter changed simultaneously, finally reaching the values of advancing contact angle  $\theta_a$  and initial diameters listed in Table 5.2. A constant decreasing of the contact angle was observed as well as a constant diameter, suggesting a pinned CL during the evaporation process for some cases.

As advancing contact angle depends on the liquid–air and solid–liquid interfacial tensions, in case of surfactant solutions the duration of the spreading stage can be determined by the adsorption kinetics of the surfactant and therefore it can be much longer than in case of simple liquids. The stage of spreading can overlap considerably with the first stage of evaporation. In order to determine the advancing and receding contact angle of aqueous surfactant solutions at low and high concentration and neat surfactant contact angle measurements for mL droplets were taken (Table 5.2). Advancing and receding contact angles on the same drop were measured by keeping the needle in contact with the drop through-out the experiment while adding and removing liquid. The contact angle value from drop to drop and for different solid samples had a standard deviation of  $2^\circ$ . The initial volume of the droplet was fixed at  $3 \mu\text{L}$  and the advancing/receding contact angles were measured at three different positions on each substrate.

Tallow amine ethoxylate 1 g/L	$\theta_a$	$\theta_r$	CAH	Tallow amine ethoxylate 3 g/L	$\theta_a$	$\theta_r$	CAH	Tallow amine ethoxylate neat	$\theta_a$	$\theta_r$	
OTS	75	49	26	OTS	74	47	27	OTS	-	-	
CDO	64	32	32	CDO	63	31	32	CDO	-	-	
HMDS	57	27	30	HMDS	56	25	31	HMDS	-	-	
Surf1 1g/L	$\theta_a$	$\theta_r$	CAH	Surf1 3g/L	$\theta_a$	$\theta_r$	CAH	Surf1 neat	$\theta_a$	$\theta_r$	CAH
OTS	57	16	41	OTS	38	12	26	OTS	53	10	43
CDO	46	16	30	CDO	23	8	15	CDO	29	14	15
HMDS	48	10	38	HMDS	14	5	9	HMDS	25	6	19
Surf2 1g/L	$\theta_a$	$\theta_r$	CAH	Surf2 3g/L	$\theta_a$	$\theta_r$	CAH	Surf2 neat	$\theta_a$	$\theta_r$	CAH
OTS	66	20	46	OTS	38	12	26	OTS	50	11	39
CDO	42	12	30	CDO	17	5	12	CDO	19	2	17
HMDS	38	7	31	HMDS	13	6	7	HMDS	20	1	19

- The neat surfactant is too viscous to measure the contact angle.

Table 5.2: Advancing and receding contact angles for for 3- $\mu$ L droplets of aqueous surfactant solutions. CAH = Contact angle hysteresis =  $\theta_a - \theta_r$ .

Table 5.2 shows that for all the aqueous solutions of the surfactants, both advancing and receding contact angles decrease when the concentration of surfactant in water increases. According to the data obtained during the static evaporation (Table 5.2), only the CDO substrate were used for the rest of experiments.  $\theta_a$  and  $\theta_r$  values matched in a similar way for both CDO and *Clivia* leaves (Table 5.3).

	1 g/L	3 g/L
Tallow amine ethoxylate	65	64
Surf1	38	22
Surf2	24	22

Table 5.3: Contact angles for 3- $\mu$ L droplets of aqueous surfactant solutions on *Clivia* leaves.



## **5.5 Aqueous surfactant solutions + Active ingredient: Colloidal suspensions**

Annular deposits formed from drying drops containing particles have received much attention in the scientific literature since Deegan et al<sup>139</sup> showed the role of particle pinning at the deposit periphery.

The deposit form is an important factor for the biodelivery and biological performance, especially when surfactants are combined with particulate, systemic AIs. In such cases, the distribution of both the AI particles, and adjuvant is important along with the degree of association between these two components and the drop size that produces different doses on an area basis. Despite the complexity surrounding formation of deposits, the deposit form is governed by the physical, colloidal and surface forces. CL pinning is enhanced by surface roughness, chemical heterogeneities or particles inside the droplet.

This section describes two surfactants: Surf1 and Surf2 with Tebuconazole as an AI. The formulations used are described in Chapter 4. In order to study the morphology of the deposit and the spatial distribution of the AI crystals throughout the deposit, SEM is used. Figure 5.7 shows characteristic images of spread area and the surfactant distribution for both formulations. AI particle distribution is also seen for Surf1.

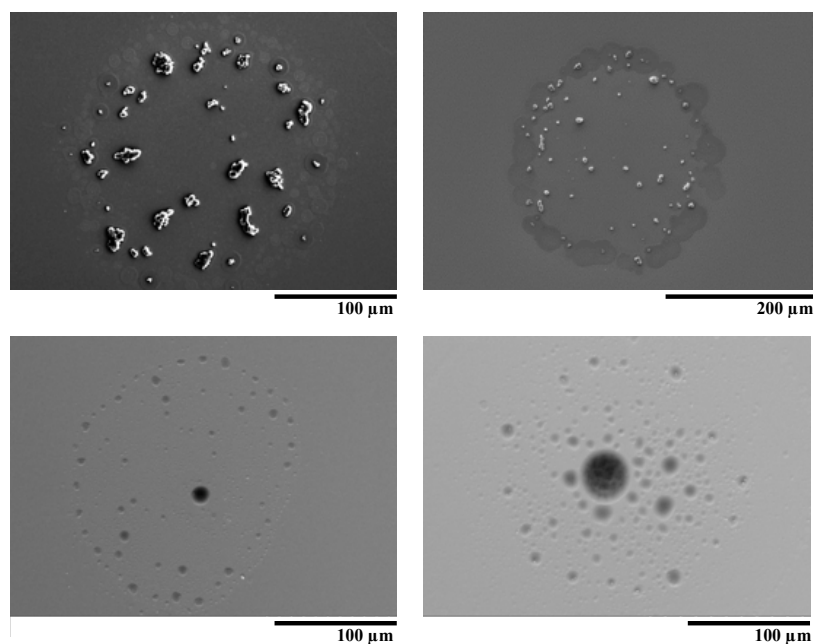


Figure 5.7: SEM images of dried deposits from 1.5 nL drops on CDO, a hydrophobic surface, containing Surf1 (upper images) and Surf2 (lower images) solutions at 1 g/L (left) and 3 g/L (right) concentration with AI (2.58 g of 25% SC Tebuconazole which contains 0.625 g of Tebuconazole).

In Surf1, all the deposits formed an annular deposit, in which the residue of surfactant remained as a thin band at the edge of the original droplet. This deposit pattern is more frequently seen when the AI is solid and formulated as a suspension. The AI is partitioning between the solution, the micelles and particles. For Surf1 at 1 g/L, the amount of crystals on the surface is higher than in 3 g/L because at concentrations above the CMC, the crystals are dissolved in the micelles. In Surf2 all the AI is dissolved in the droplet forming an emulsion.

Figure 5.8a shows a zoom-in image of Surf1 3 g/L + AI deposit (Figure 5.7). As a comparison, Figure 5.8b shows a deposit of a droplet of 25% SC Tebuconazole in water printed on a hydrophobic surface in order to see the shape and size of the AI crystals in the absence of surfactant.

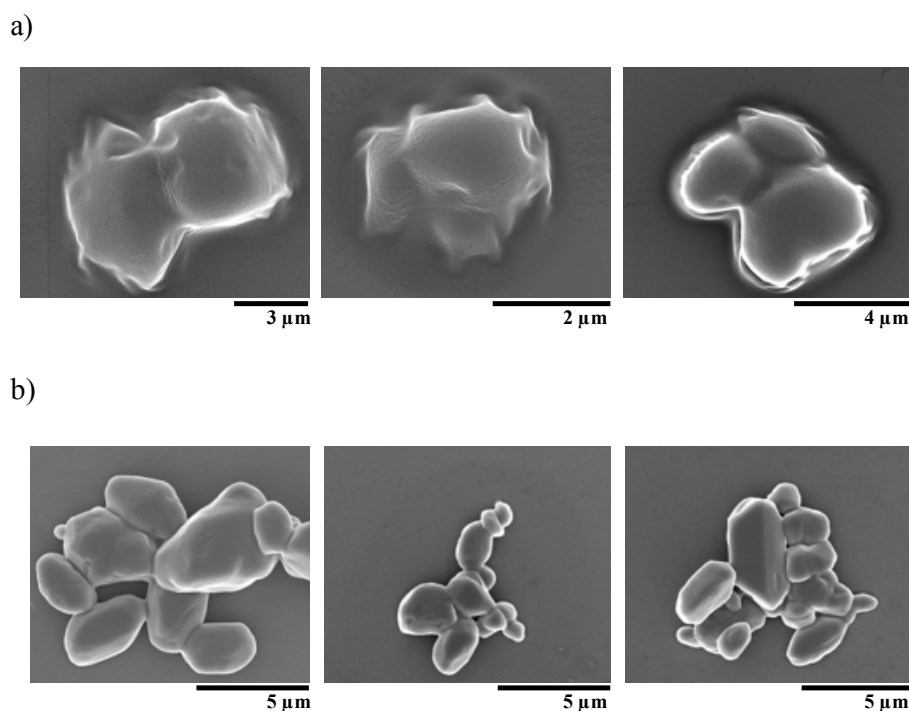


Figure 5.8: a) SEM images of Tebuconazole crystals on a dried deposit covered by Surf1 solution, b) SEM images of a 25% SC Tebuconazole in water droplet printed on a hydrophobic surface.

Figure 5.8a shows three different AI crystals from the interior and edge of the droplet. In all positions the crystals are totally covered by a surfactant layer. The AI crystals at the edge of the deposit are covered with a higher amount of surfactant at higher concentrations.

Surf2 + AI surfactant solution at a concentration of 1 g/L (Figure 5.7 bottom left) formed deposits with differently sized liquid droplets in which the crystals were completely dissolved. In this case, the ratio surfactant–AI is 60%–40% and it can be considered as a supersaturated solution because some of the AI crystals crystallized out of solution over time (Figure 5.9). In supersaturated solution, the chemical potential of the AI increases, which should enhance the transport of the AI through the leaf.

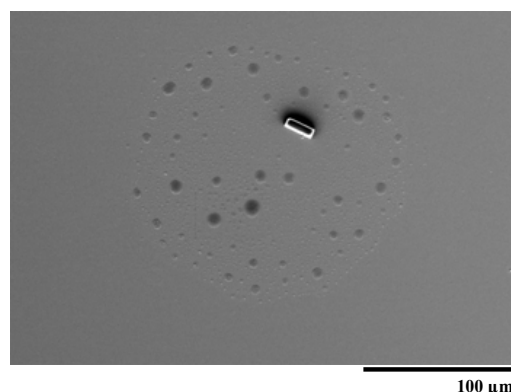


Figure 5.9: Recrystallization of AI in the amidoamine based surfactant + AI at 1g/L concentration over time.

However, when the concentration of the surfactant solution was 3 g/L all the AI crystals were dissolved and did not crystallize out, also forming small droplets with different sizes over the whole deposit (Figure 5.7 lower right).

#### 5.5.1 Variation of the contact angle and diameter during the different modes of evaporation for agrochemical solutions with and without AI.

The coverage area of a water droplet on substrates with different wettabilities varied greatly (shown in Section 5.3). Figure 5.10 and Figure 5.11 show variation of the contact angle and the diameter of two different formulations on a hydrophobic surface. PS particles were not added in the following experiments as there are AI crystals or droplets present already to visualise the internal flows within the droplet.

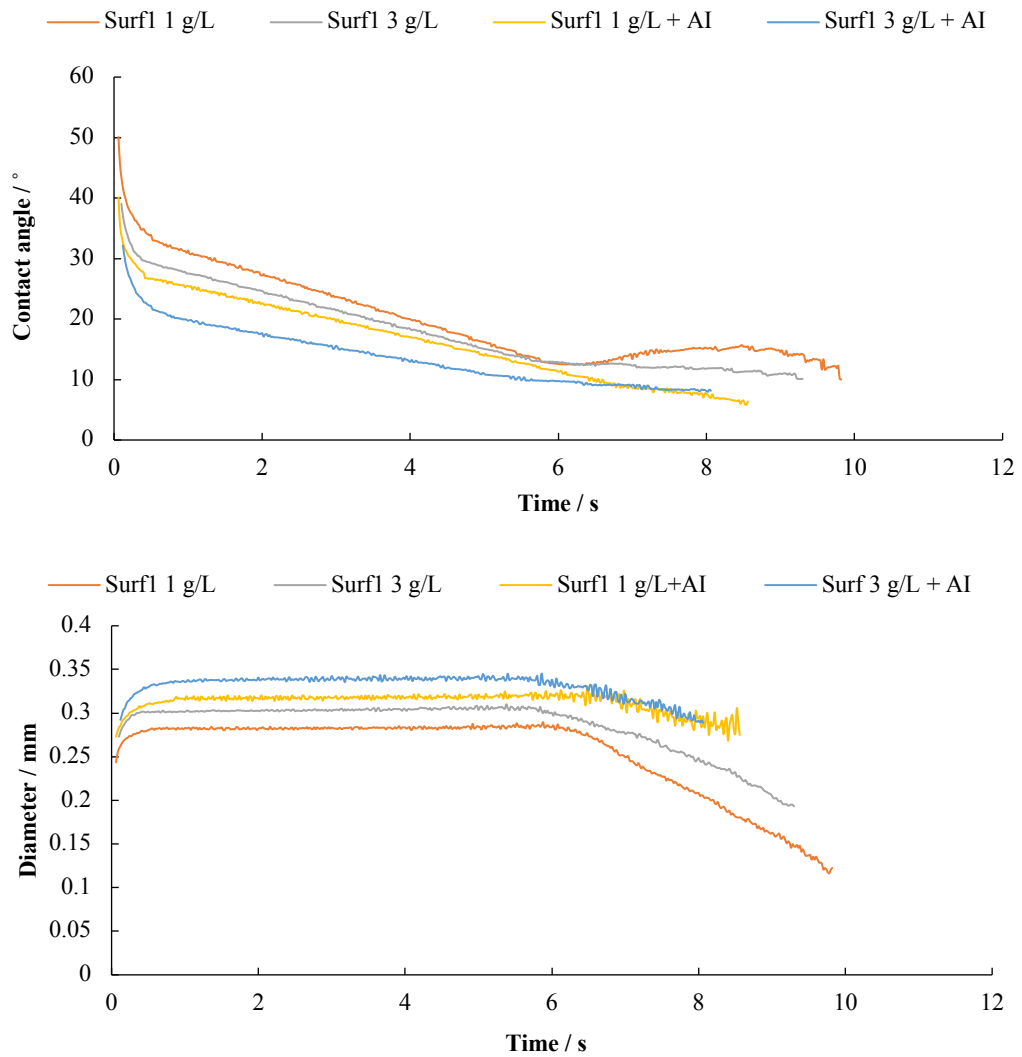


Figure 5.10: Profile of the a Surf1 droplet on CDO: a) Contact angle and b) Diameter.

For droplets containing surfactant at different concentration and also AI particles, the evaporation process and the coverage pattern formation with time performed differently on the same hydrophobic substrate. This variation might be related to the surface tension of the solutions (Figure 4.1). For Surf1, the CMC is approx. 1.5 g/L and Figure 5.10 shows the variation of the contact angle and diameter below and above this value (1 g/L and 3 g/L respectively). A lower surface tension in the formulation will form droplets with a lower contact angle, and thus a larger radius with a faster evaporation (Eq. 2.9). The addition of particles also decreased the surface tension of the solution giving at the end droplets with a higher diameter.

Figure 5.11 shows the evaporation mode for Surf2 with and without AI as in the previous case. However, for Surf2 solutions, neither the contact angle nor diameter of the droplets was affected by the concentration of the surfactant or the presence of AI. The main reason of this behavior is because the surface tension of the different solutions is not changing.

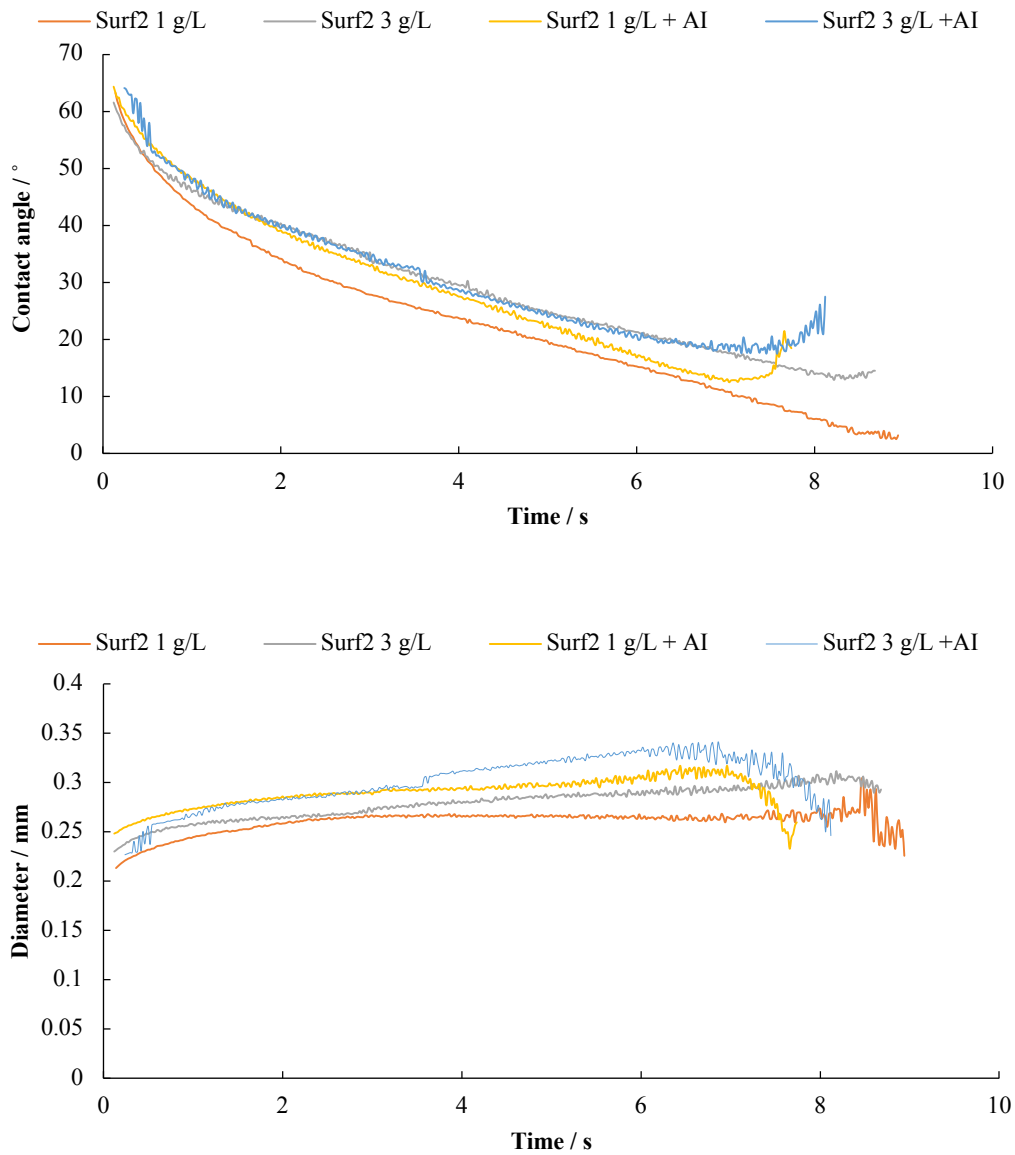


Figure 5.11: Profile of a Surf2 droplet on CDO: a) contact angle and b) diameter.

## **5.6 Effect of variations in temperature of the substrate and relative humidity**

The effect of substrate temperature and *RH* on the evaporation mode of agrochemical droplets is of fundamental interest to the agrochemical industry. Temperature of the substrate and *RH* greatly affect how quickly these droplets evaporate. The leaf cuticle responds to *RH* becoming more permeable under high humidity conditions. While it is clear that environmental variables have a profound effect on the uptake and efficacy of foliar-applied herbicides, there is relatively little information on the exact mechanisms involved in the influence of humidity and temperature on herbicide and surfactant performance<sup>124</sup>. One reason for this problem is the daunting number of herbicide/species/humidity/temperature combinations used in field and laboratory experiments, making development of broad conclusions difficult<sup>125</sup>.

Evaporation mode of droplets under three different temperatures of the substrate (10, 20 and 30 °C) and three *RH* conditions (23, 50 and 80%) were studied in order to see the influence of these two parameters on the morphology of the deposit. The agrochemical solution shown in this section is Surf1, an alkyl ethoxylate surfactant at two different concentrations with AI particles. Two other formulations were tested: Surf2, an amidoamine-based surfactant and the use of a humectant, however the effect of temperature and *RH* on these results formulations are not shown in this thesis as the behavior was very similar to Surf1.

### 5.6.1 Temperature of the substrate

The effect of the substrate temperature on the contact line behavior is shown for Surf1 at two different concentrations with AI particles in Figure 5.12, at an ambient temperature of 22 °C and a relative humidity of 40%.

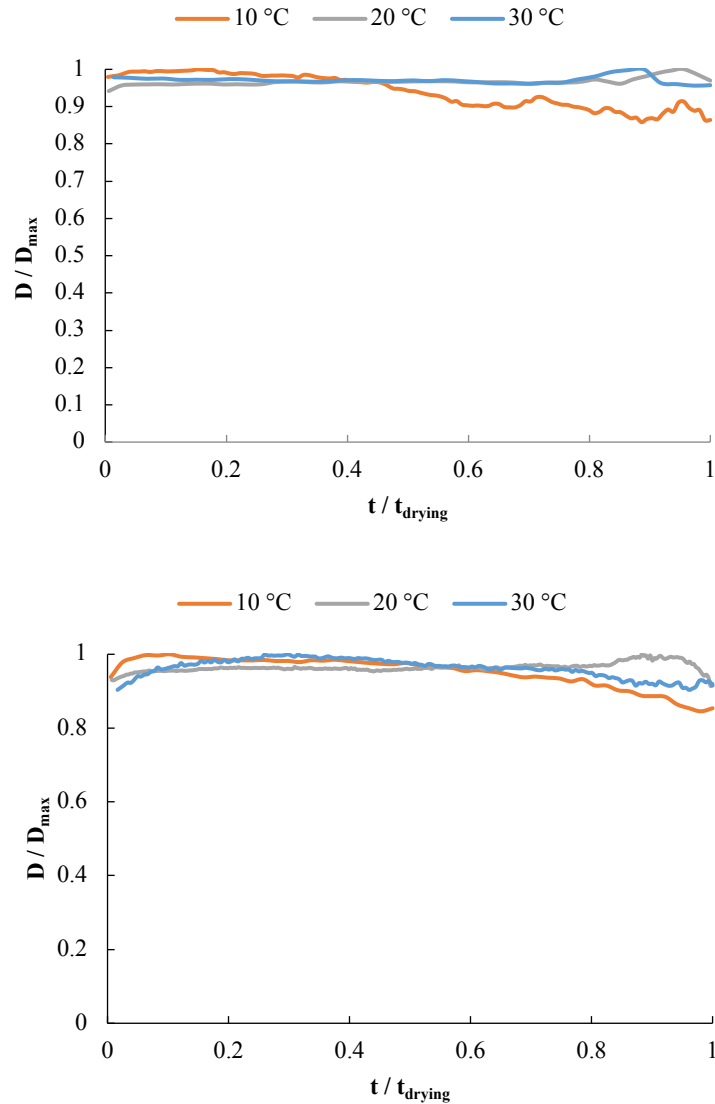


Figure 5.12: Effect of the substrate temperature on the behavior of the normalized diameter line for Surf1 solution and AI particles at different concentrations of 1 g/L (upper image) and 3 g/L (lower image). Drying times for 1 and 3 g/L at three different temperatures: 10, 20 and 30 °C are 4, 6 and 14 s and 4, 7, 16 s respectively.  $D_{max}$  is the maximum diameter.

The total evaporation time is longer at lower substrate temperatures in both cases. There is no difference in the mode of evaporation at these three temperatures and the size of the final deposit is very similar for both Surf1 concentrations tested. However,



at lower substrate temperature the depinned stage leads to a small effect ( $\sim 10\%$ ) on the final droplet diameter as shown in Figure 5.12. This is mainly because of the surface tension, that is the main force of depinning, is higher near the contact line when the substrate temperature is lower<sup>126</sup>.

Figure 5.13 show the optical images of the morphology deposits for Surf1 at 1 and 3 g/L and at three different substrate temperatures (10, 20 and 30 °C).

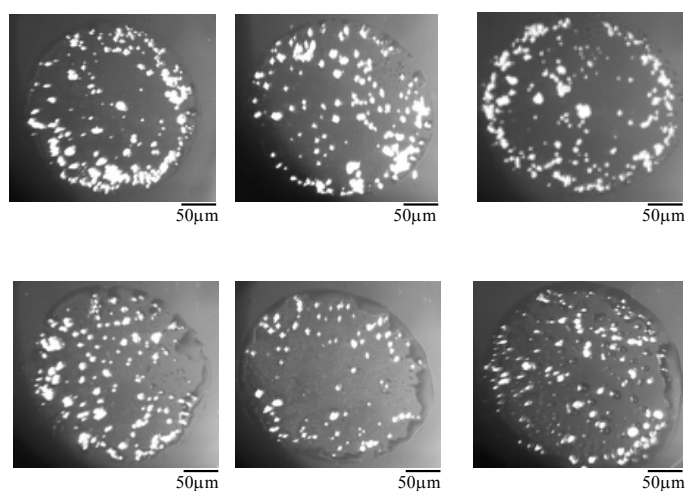


Figure 5.13: Effect of the substrate temperature on the morphology of a dried deposit of Surf1 + AI particles at 1 g/L (upper images) and 3 g/L (lower images): a) 10 °C, b) 20 °C and c) 30 °C.

### 5.6.2 Humidity variation

Some authors have shown the influence of  $RH$  variation on the dried deposits. Hunsche et al<sup>127</sup> mentioned that for glyphosate-AI association is lower at low  $RH$  indicating that the evaporation rate is important for the position of the single compounds. Zhu et al<sup>128</sup> have published that the droplet coverage area was not influenced by the changes in  $RH$ . Cook et al<sup>129</sup> suggested that one of the benefits of high humidity was the prevention of herbicide crystallization, which depletes the concentration of AI in solution, thereby decreasing penetration.

The evaporation time of droplets greatly increased as  $RH$  increased for the droplets on hydrophobic surfaces. For example, when  $RH$  increased from 23 to 80% the evaporation time of water and Surf1 at 1 g/L increased from 11 to 33 s and from 4 to 16 s respectively. However, the variation in  $RH$  conditions has no considerable effect

on the mode of evaporation for any of the cases and the morphology of the dried deposit. The  $RH$  did not influence the coverage areas of the final deposit.

Figure 5.14 shows an example of the morphology of a dried deposit of Surf1 with AI particles at three different  $RH$  conditions.

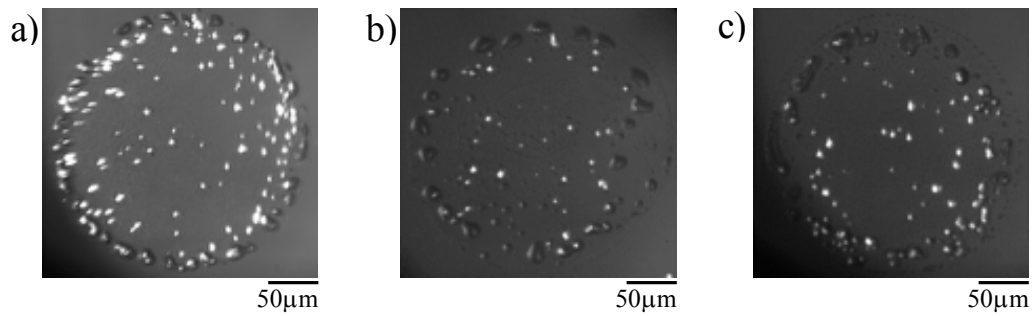


Figure 5.14: Effect of the  $RH$  on the morphology of a dried deposit of Surf1 + AI particles: a) 23%, b) 50% and c) 80%.

## 5.7 Control of the deposit morphology through an evaporation-driven sol-gel transition

Many parameters, including the drying conditions (such as the substrate temperature or the relative humidity), the wettability of the substrate, and the properties of the dispersed particles, have been shown to affect the morphology of the deposit<sup>130</sup>.

Another way to control the morphology of the deposit is to suppress the CRE by increasing the viscosity of the droplet during drying. Very high viscosity liquids are not good for printing applications, so viscous liquids with tailored rheological properties must be used. However, unless the increase in viscosity overcomes the capillary flow a ring stain will still stay. The Capillary number,  $Ca$ , describes the ratio of viscous effects to surface tension effects,

$$Ca = \eta u / \sigma \quad \text{Eq. 5.3}$$

where  $\sigma$  is the surface tension,  $\eta$  is the viscosity and  $u$  is the fluid velocity.

The Capillary number must approach one in order for viscous effects to become significant. For water,  $Ca = 10^{-3} \text{ Pa s} \times 10^{-5} \text{ m s}^{-1} / 10^{-2} \text{ N m}^{-1} \sim 10^{-6}$ ; a  $10^{-6}$ -fold increase in viscosity during drying is required to get a  $Ca \sim 1$ . If  $Ca \geq 1$ , then the droplet can deform from a spherical cap.

An alternative strategy for suppressing the ring stain is to exploit the elastic (rather than the viscous) properties of complex fluids. In order to overcome the capillary flow and prevent particle motion, the elastic modulus of a viscoelastic fluid must exceed the capillary pressure (estimated by Laplace pressure).

The dimensionless number

$$\varepsilon = (G' r_c) / 2\sigma \quad \text{Eq. 5.4}$$

$\varepsilon$  is defined as the ratio of the elastic modulus,  $G'$ , to the Laplace pressure  $P = 2\sigma / r_c$  inside the droplet, where  $r_c$  is the radius of curvature of the droplet. In order to resist deformation,  $\varepsilon$  must be at least of the order 1. For a water-based droplet with a radius of  $250 \mu\text{m}$  achieving a  $\varepsilon = 1$  corresponds to an elastic modulus of  $G' \sim 10^2 \text{ Pa}$ . This is more likely to be achievable than a viscosity increase of the order of  $10^6$ .

There are different ways how elasticity can be achieved. One method is by using Laponite. Laponite (hydrous sodium lithium magnesium silicate) has a density of  $2.53 \times 10^{-3} \text{ kg m}^{-3}$  and a single Laponite crystal is disc shaped and nearly uniform, typically  $25 \text{ nm}$  in diameter by  $0.92 \text{ nm}$  thick, much smaller than natural clays<sup>131</sup>. Laponite structure is shown in Figure 5.15, within a single crystal, each sheet of octahedrally coordinated aluminium or magnesium oxide is sandwiched between two layers of tetrahedrally coordinated silica. The crystal faces have negative charge that is balanced by interlayer cations which are predominantly  $\text{Na}^+$ . The structure of individual Laponite particles and a schematic drawing of the proposed 'house of cards' soft-solid phase are illustrated in Figure 5.15.

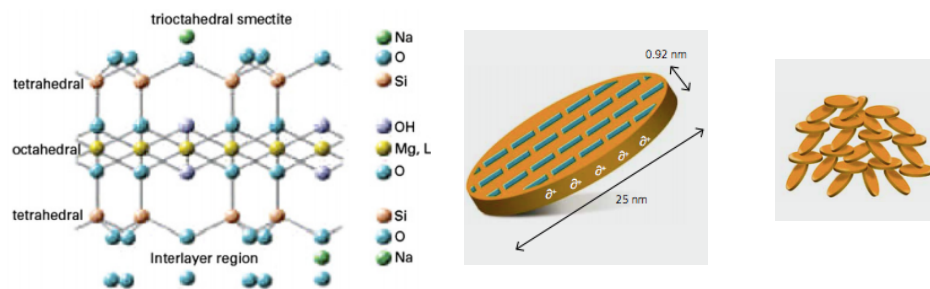


Figure 5.15: Structure of individual Laponite particles and schematic house of card structure of Laponite gel stabilized by electrostatic interaction between the negatively charged faces and positively charged edges of the disc-shaped colloidal particles (from Southern Clay Products product information website<sup>132</sup>)

Laponite might not produce CRE because they swell to form a gel when dispersed in water due to the sol-gel transition of them during the evaporation. A sol is a stable suspension of colloidal particles in a fluid. A gel is a complex fluid/soft solid that has elastic properties at rest but flows under shear. As the droplet evaporates, Laponite concentration within the droplet increases, but this increase is not uniform and in the absence of convection, the concentration is highest at the CL where the evaporation is faster, thus so gelation starts at the contact line. The formation of gel resists the capillary stresses and the resulting flow of the particles. The concentrations used in our experiments are below the sol-gel transition and gelation is only expected to occur with evaporation.

Another way to modify the elasticity is by adding silica particles. Interactions of fumed silica particles are dominated by the surface siloxane bonds of the oxide backbone and the surface silanol groups. Owing to its surface silanol groups and its oxide nature, fumed silica is hydrophilic and exhibits a high surface energy. Deactivation of the surface silanol groups by silylation with alkylchlorosilanes or alkylsilazanes strongly decreases the surface energy of the oxide, and its surface becomes hydrophobic. In this thesis, a synthetic, hydrophobic, amorphous silica produced via flame hydrolysis is used. The relative silanol content in relation to the hydrophilic silica is approximately 50%. The rheological effectiveness of fumed silica results from an interplay of space-filling particle structures and strong particle-particle interactions. Among particle-

particle surface interactions, hydrogen bonds have been discussed as one of the main driving forces for the attachment of fumed silica particles<sup>133</sup>.

In this chapter the effect of the addition of Laponite and silica particles on the morphology of the final deposit is reported when an alkyl ethoxylate surfactant at 1 and 3 g/L + AI is used.

### 5.7.1 Preparation of the Laponite and silica suspension:

Different amounts of Laponite powder were added slowly to the Surf1 + AI and stirred for 24 h before they were printed.

The fumed silica NPs used in this study were provided by Wacker Chemie (Germany HDK® H20)) and were used as received. The diameter of individual NPs is 20–30 nm. Silica particles with 50% SiOH were dissolved in EtOH and added to Surf1 + AI in order to get different concentrations of silica particles added.

### 5.7.2 Surface tension measurements of the solutions

The surface tension of the new solutions were measured in order to understand the effect of the addition of either Laponite or silica particles on the evaporation mode of the droplets. Figure 5.16 shows the variation of the surface tension when the hydrophobic Laponite or silica particles are added to Surf1 at 1 and 3 g/L + AI.

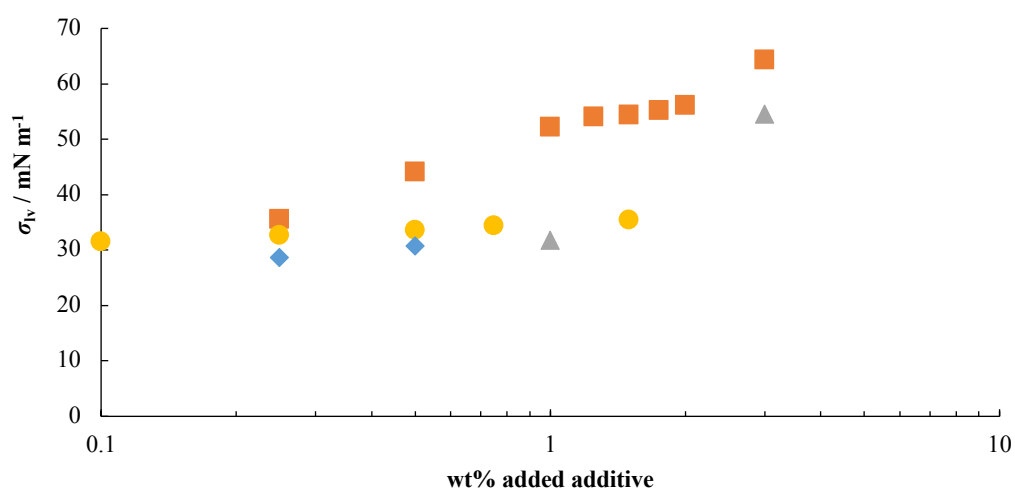


Figure 5.16: Surface tension of the Surf1 1 g/L + AI and Surf1 3 g/L + AI with the additives: Laponite (orange squares and grey triangles) and silica particles (yellow circles and blue diamonds).

Figure 5.16 shows that as the concentration of the additives is increased, the surface tension increases. This might be possible because of interactions between the surfactant and the particles that decrease the chemical potential of the surfactant (i.e. decreases monomer concentration). It seems that the Laponite absorbs the surfactant like it is shown in Figure 5.17.

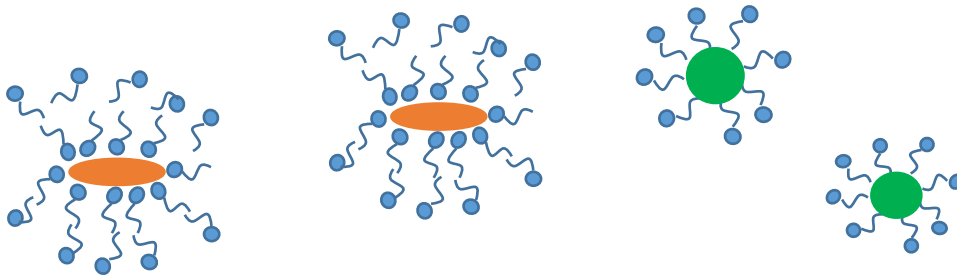


Figure 5.17: Sketch of the interaction between both the hydrophilic Laponite (orange disks) and hydrophobic silica particles (green circles) with the surfactant (blue).

Below the CMC there are no micelles and the amount of free surfactant is lower which is why the surface tension value is higher. The silica also absorbs the surfactant but the increase in surface tension is lower than with Laponite.

### 5.7.3 Morphology of the dried deposit after the addition of additives

Since the annular deposits are formed by liquid flows within the evaporating drops then modification of the rheology of the dispersion should have an effect on the deposit structure.

Figure 5.18 shows the morphology of the deposits with Surf1 at 1 g/L and 3 g/L + AI and the addition of 50% hydrophobic silica particles at different concentrations.

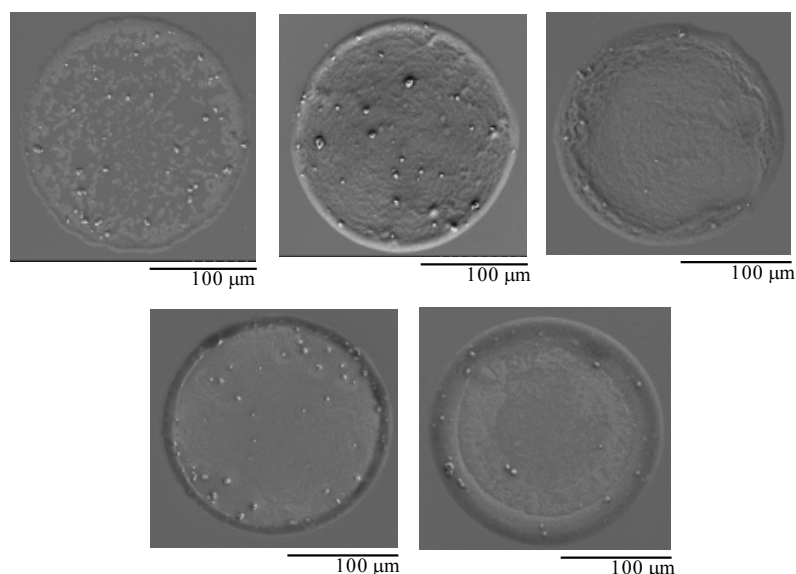


Figure 5.18: Effect of 50% hydrophobic silica particles on the morphology of dry deposits at 300x zoom with Surf1 1g/L + AI at different concentrations: a) 0.10 wt%, b) 0.50 wt% and c) 0.75 wt% (upper images) and also Surf1 3g/L at 0.25 wt% and 0.50 wt% (lower images).

The addition of hydrophobic silica particles to the surfactant solution + AI showed a different pattern of the dried deposit on the substrate. CRE was not suppressed at any concentration of silica particles. The videos showed how the PS particles moved during the whole drying process going to the edge of the droplet. As the water evaporated, the movement of these particles were slower due to the viscosity of the remaining liquid. Because of the increase in surface tension and the lack of suppression of the CRE, hydrophobic silica was not used in subsequent experiments.

Talbot et al<sup>112</sup> presented the steady-state shear viscosity of Laponite suspensions over a range of shear rates. The Laponite suspensions were shear-thinning when the Laponite concentration exceeded about 2.5 wt%. Above 3 wt% Laponite, there was no Newtonian plateau, indicating yield-stress behaviour.

In order to produce uniform deposits, Laponite gel was added to the suspension formulation and a homogenous distribution of AI crystal was visible. For an alkyl ethoxylate surfactant at 1 g/L + AI, the initial contact angle increased dramatically after the addition of Laponite at any of the concentrations reaching a value around  $85^\circ \pm 2^\circ$ . It seems that the Laponite absorbs the surfactant decreasing the amount of

free monomers. Figure 5.19 shows scanning electron micrographs of the dried deposits from various formulations containing 1–1.75 wt% of Laponite.

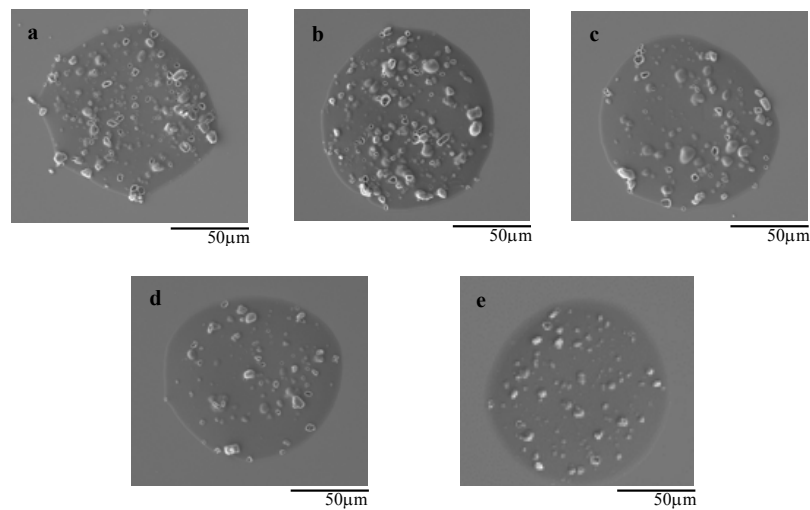


Figure 5.19: SEM images of the whole deposits at 500x zoom of Surf1 at 1g/L + AI containing a) 1 wt% Laponite, b) 1.25 wt% Laponite, c) 1.5 wt% Laponite, d) 1.75 wt% and e) 2 wt% Laponite.

For the Laponite, uniformly dispersed deposits are formed because the CL is receding, which is not desirable because the covered area of the surface is smaller. For all the concentrations of Laponite, the droplets started to shrink leaving a small deposit of around 100μm.

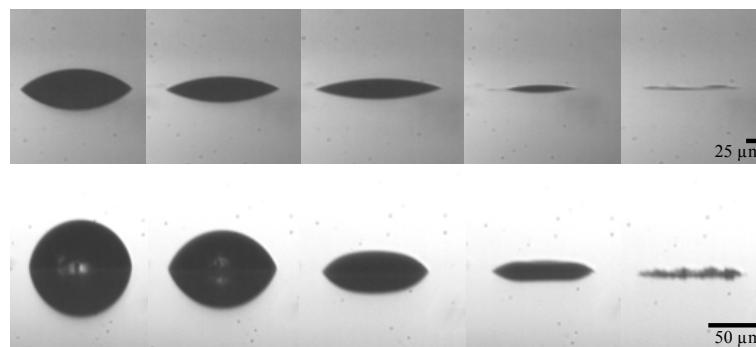


Figure 5.20: Profile images during the drying process of a) Surf1 1 g/L + AI and b) Surf 1 1 g/L + AI + 1 wt% Laponite. The images with Laponite show the progression of the gelled ‘disk’.



The higher value of the surface tension created droplets with a higher contact angle generating less spreading of the droplets. This effect is not desirable for agrochemical applications, so Laponite was not used in later experiments.

## 5.8 Addition of “Superspreaders”

Superspreading surfactants are those which form, at a concentration of 0.1 wt% or less in aqueous solutions, a thin film on hydrophobic surfaces within seconds<sup>134</sup>. Hydrophobic surfaces can be parafilm, polypropylene foliages or waxy surfaces of plant leaves. Such surfactants are trisiloxane polyethers, silane polyethers and also fluorosurfactants. “Superspreaders” are added to aqueous solutions of pesticides to promote adhesion to targets via surface tension reduction and to engender droplet spreading to maximize surface contact area. Ever since the discovery of their utility by Jensen<sup>135</sup> to provide outstanding spray coverage of the weeds has been cited as the reason for their exceptional efficacy. Fluorosurfactants are the most effective compounds to lower the surface tension of aqueous solutions. Because of low polarizability of fluorine the van der Waals interactions between fluorinated chains are weak, resulting in low cohesive energy of fluorocarbons and as a consequence low surface tension and low CMC. Fluorosurfactants as well as trisiloxanes are capable of lowering the surface tension of aqueous solutions to 18–25 mN m<sup>-1</sup>.

In this thesis, two different “Superspreaders” have been used: a trisiloxane, Silwet Gold, and a non-ionic fluorosurfactant, Capstone® FS30. Both chemical structures are shown in Figure 5.21. The addition of “Superspreaders” in my experiments was not to control the spreading of the drop; the idea was to reduce the contact angle of the small emulsion droplets of Surf2 by reducing the air–liquid surface tension and thus, increase the contact area between the formulation and the leaves.

a)

b)

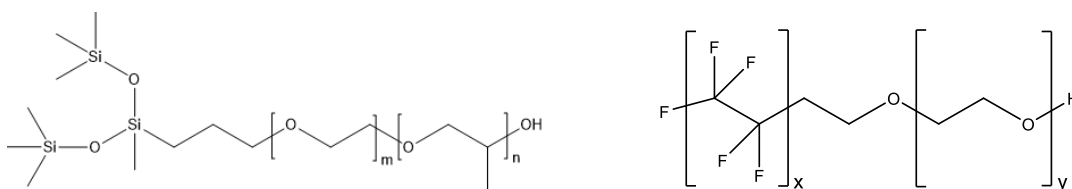


Figure 5.21: Chemical structures of two “Superspreaders”: a) Silwet Gold and b) Capstone® FS30.

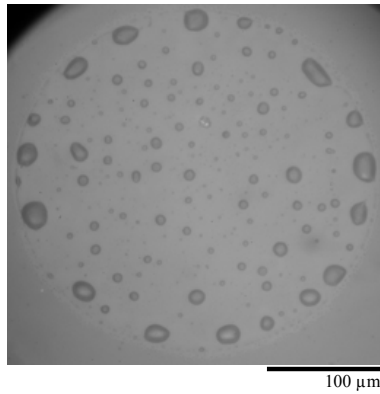
The “Superspreader” concentrations used were 0.01, 0.02, 0.03 wt%. and were added to the amidoamine-based surfactant solutions. Also surface tension measurements of the new solution have been measured (Table 5.4).

Formulation	Surface tension $\pm 0.1 \text{ mN m}^{-1}$
Surf2 + AI	28.1
Surf2 + AI + 0.01 wt% Silwet Gold	27.9
Surf2 + AI + 0.02 wt% Silwet Gold	27.8
Surf2 + AI + 0.03 wt% Silwet Gold	27.0
Surf2 + AI + 0.01 wt% Capstone® FS30	27.5
Surf2 + AI + 0.02 wt% Capstone® FS30	27.5
Surf2 + AI + 0.03 wt% Capstone® FS30	27.0

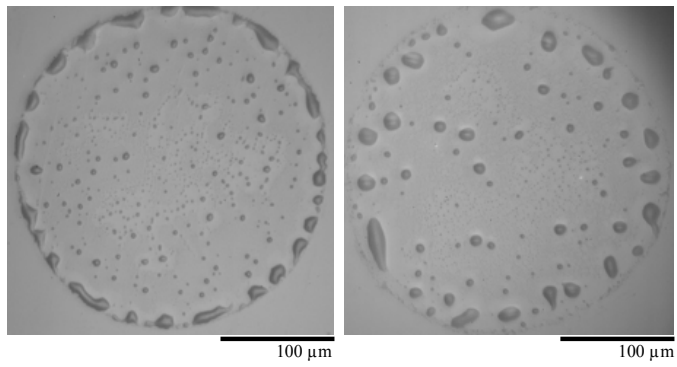
Table 5.4: Surface tension measurements of Surf2 with Silwet Gold and Capstone® FS30 at different concentrations added.

The surface tension of these formulations does not show a significant effect on the wetting of the water droplet at any of the “Superspreader” concentrations but they might have an effect on the wetting of the oil droplets (Figure 5.22). Figure 5.22 shows the optical images of Surf2 +AI and Surf2 + AI + 0.01 and 0.02 wt% Silwet Gold and Capstone® FS30 deposits.

Amidoamine-based surfactant + AI



+ Silwet Gold



+ Capstone® FS30

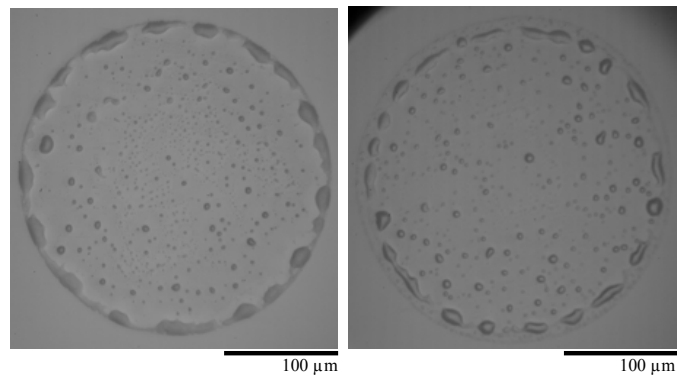


Figure 5.22: Optical images of Surf2 + AI, Surf2 + AI + Silwet Gold and Surf2 + AI + Capstone® FS30 deposits at two different concentrations: 0.01 and 0.02 wt%.

Figure 5.23 show the SEM images of Surf2 and Surf2 + either Silwet Gold or Capstone® FS30 deposits at 0.03 wt%. Zoomed images are also shown in order to get a more specific information of the deposit.

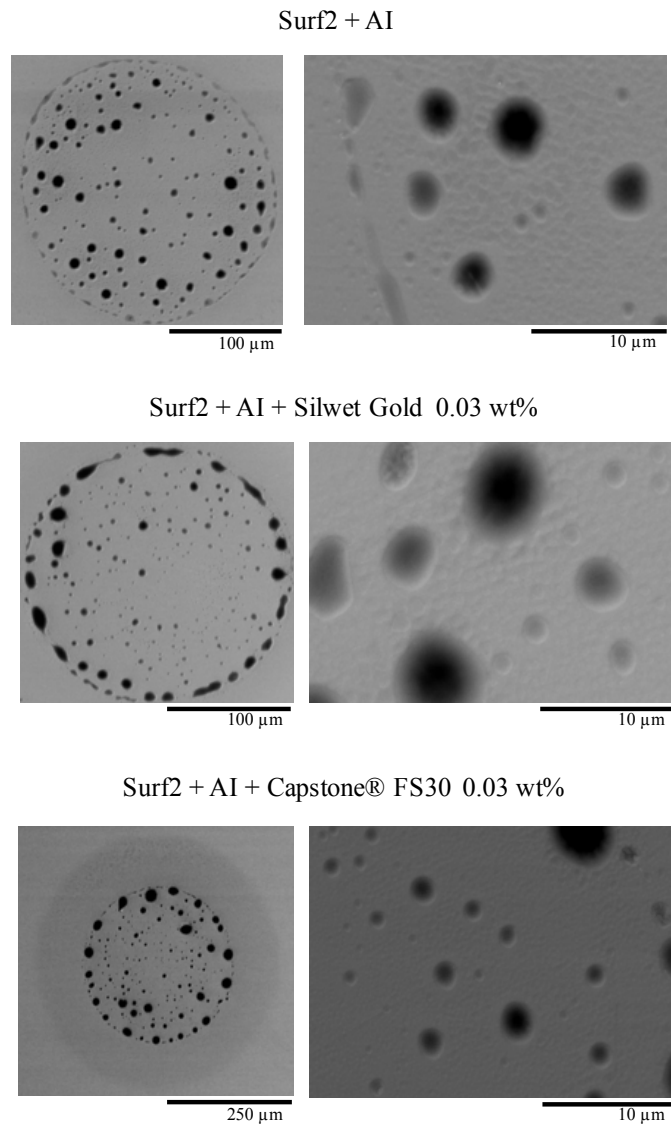


Figure 5.23: SEM images of the whole deposits at 300x zoom of Surf2 at 3 g/L + AI containing a) just Surf2, b) Surf2 + Silwet Gold 0.03 wt% and c) Surf2 + Capstone® FS30 0.03 wt%.

It can be seen in Figures 5.22 and 5.23, that morphology and diameter of the deposits of the amidoamine-based surfactant are mostly/completely covered by small liquid droplets of the mixture of surfactant and AI. Only when Capstone® FS30 was used at 0.03 wt%, a halo was seen around the deposit (Figure 5.23), however, AI was not detected by EDS in this area. In order to be able to compare the results, all the experiments were done in the same day and on the same substrates. Droplets with no addition of “Superspreaders” are also shown to be able compare any changes on the morphology of the deposit.

Chapter 3 mentioned that the use of interference fringes and illumination from below was useful in determining the changing profile of the drying drop. The set up for this experiment was the same as before but differed in the illumination; a bandpass filter (Thorlabs, CWL 470 nm) was added after the LED in order to increase the coherence length of the light reaching the camera. The substrate–drop and drop–air interface provided two different reflective surfaces, giving two reflected beams from the illumination light which recombine before reaching the camera to give an interference pattern in the final images. As reflection from the substrate is constant, any change in the interferometry images during drying can be attributed to changes in the drop profile (i. e. film thickness at varied position of the drop).

The difference between film thickness that is associated with two neighbouring bright (or dark) fringes is given by<sup>136</sup>

$$D_{fr} = \frac{\lambda}{2n} \tag{Eq. 5.5}$$

where  $D_{fr}$  is the distance between fringes and  $n$  is the refractive index. As the wavelength used was 470 nm and the refractive index of Surf2 and AI was approx. 1.50, the distance between bright fringes was 157 nm. An example of an image for the calculation of the distance between fringes is shown in Figure 5.24.

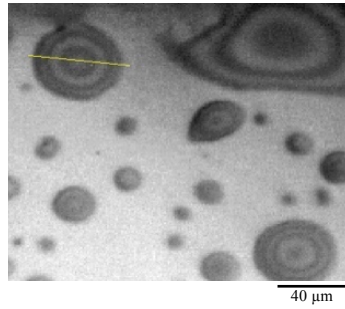


Figure 5.24: Interferometry measurements of Surf2 + AI + Silwet Gold 0.03 wt%.

MATLAB was used to build up a picture of the changing film thickness of the droplet on the dried deposit (code written by Dr. L. Yang). From the position of the fringes, the film thickness at the deposit position and then, the estimated drop height (maximum thickness) and the contact diameter (maximum length) can be calculated. By assuming that the droplet is a spherical cap and knowing the estimated height and diameter (Eq. 5.6) on the dried deposit (derived from the drop profile) one can figure out the contact angle of the small droplets in the deposit in order to be able to see the effect of it after the addition of the “Superspreaders”.

$$\theta = 2\text{tan}^{-1}(h/R) \quad \text{for small } \theta \quad \text{Eq. 5.6}$$

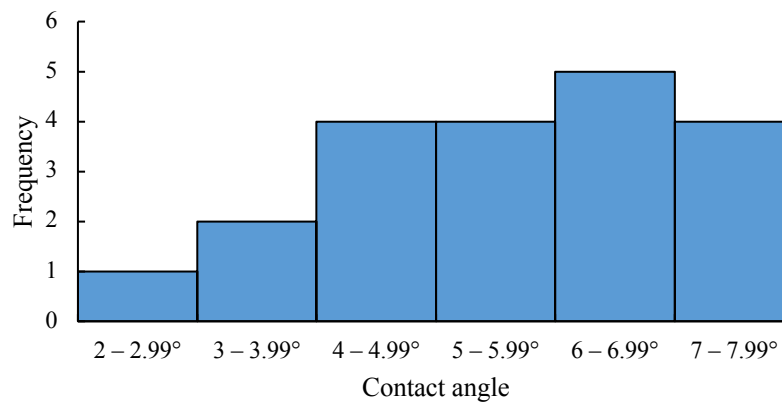
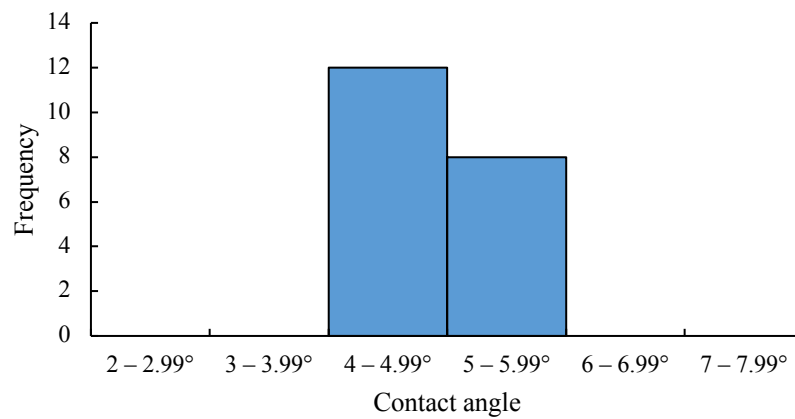
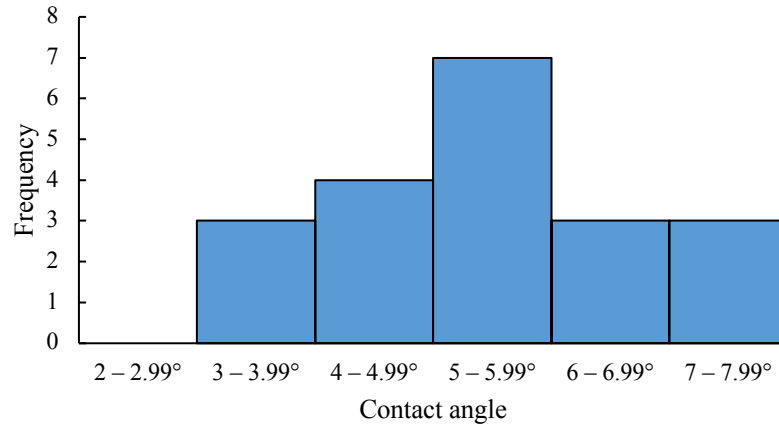


Figure 5.24: Histograms from interferometry measurements of different solutions: Surf2 + AI (upper image), Surf2 + AI + Silwet Gold 0.03 wt% (middle image) and Surf2 + AI + Capstone® FS30 0.03 wt% (bottom image).

As can be seen in Figure 5.24, there are droplets with different sizes for the three cases, having an average of diameter and height approx. 21 and 0.5  $\mu\text{m}$  and giving rise to contact angles between 2–8°. When Silwet Gold was added, more uniform droplets were formed. However, when Capstone® FS30 was used, different sizes were seen

varying from 2–7°. The addition of “Superspreaders” did not have an effect on the whole morphology of the deposit, but the average contact angle of the small oil droplets inside the deposit was lower for Silwet Gold meaning that there was a larger area of contact between the surface of the leaf and the deposit, which is good for penetration (Table 5.5).

	Average contact angle (°)	Standard deviation
Surf2 + AI	5.4	0.3
Surf2 + AI + Silwet Gold	4.8	0.1
Surf2 + AI + Capstone® FS30	5.7	0.3

Table 5.5: Average contact angle of different solutions: Surf2 + AI, Surf2 + AI + Silwet Gold 0.03 wt% and Surf2 + AI + Capstone® FS30 0.03 wt% . Standard deviation is calculated in the mean. The range of droplets diameter: 14–62 µm.



## 5.9 Summary

It has been shown that many factors are involved in the evaporation of the droplets: chemical composition of the droplet, properties of the substrates, the ambient environment (e.g. temperature and relative humidity), etc. In combination with flows, the interactions between the components of particle-laden drops (particles and interfaces) define the characteristics of the deposition pattern after drying. The spreading of droplets was studied in the presence of water and surfactant on substrates with different wettabilities. Surface tension and spreading are correlated since the surface tension of a solution provides information about the evaporation mode. The drying time was dependent on both the substrate hydrophobicity and the drying mode. Pinned droplets dried faster than those with a moving contact line and evaporation on hydrophilic substrates is faster than on hydrophobic substrates (Eq. 2.9). Droplets had the smallest coverage on hydrophobic surfaces. With the addition of AI particles the lifetime of the droplets decreased because the surface tension is lower and the area is bigger for Surf1.

Agrochemical solutions are diluted around 1000 times with water and it is widely assumed that the bulk properties of water differ little from those of agrochemical solutions. However, a very low concentration of surfactants improved the performance of agrochemical applications by reducing the surface tension of the spray droplets and increasing the wetting area of the deposits. Some authors<sup>137</sup> have said that the more uniformly the plant surfaces are covered, the higher the percentage of pests in contact with the surface and the more efficient the agrochemical solution. However, others said<sup>138</sup> that a more uniform coverage area rather reduced its bio-efficacy because an increased in the droplet spread reduces the AI per unit area, reducing the concentration gradient of the AI through the cuticle of the leaf. Moreover, droplets with a bigger spread area evaporate faster and the AI has less time to penetrate. Thus, the spread area of the droplet might not be as relevant for its uptake as expected. Rather, its concentrated form at the edge of the droplet (high association between surfactant and AI) or AI dissolved within the surfactant droplets might have a bigger effect.

It is believed that the association between adjuvant and AI when the droplet dries in agrochemical solutions enhance the passage of the AI through the cuticle of the leaf<sup>5</sup>. But, what does a good association between these two compounds mean? It is well known, that in a droplet with a contact angle less than 90°, the radial flow takes the particles in the droplet to the edge forming a CRE. In this thesis, two main agrochemical formulations are described: a suspension, where adjuvant and AI are mainly at the edge, and an emulsion, where the AI is dissolved in the oil droplets.

Environmental conditions have an important influence on herbicide efficacy. In particular, the effect of humidity on herbicide uptake has been attributed to changes in cuticle hydration and droplet drying. Herbicide uptaking slows or stops when herbicide droplets dry. The temperature of the substrate and the *RH* variation tested in this thesis did not have a big effect on the coverage area of the final deposit but it did influence the evaporation time; the total evaporation time is higher at lower substrate temperature and higher *RH*.

Different strategies have been used to modify the morphology of the deposit: evaporation-driven sol-gel transitions and addition of “Superspreaders”. In the first case, Laponite and silica particles were added to the suspension formulation, Surf1 + AI. Laponite formed even deposits but the high contact angle of the droplets was higher compared to the case without Laponite, and thus the wetted area was smaller. It seems that the Laponite absorbs the surfactant decreasing the amount of free monomers. In the case of the silica particles it can be seen that annular structures are formed at all concentrations and there is no evidence for gelation of the silica. The addition of “Superspreaders” did not have an effect on the whole morphology of the deposit, but the contact angle of the small droplets inside the deposit was lower and more uniform when Silwet Gold was added to Surf2 + AI at 0.03 wt%.

# Chapter 6

## 6. Chemical characterization of the residual droplet patterns

### 6.1 Introduction

Knowledge of the composition and structure of the external surfaces of plants is vital to an interpretation of (or a prediction of) their response to typically applied substances. The surface properties of leaves not only influence the rate of penetration of a surface-applied compound but can profoundly affect the amount of that compound which is retained by the surface following its application as a spray. However, biological surfaces provide a large diversity of structures and capabilities. In foliar application, there are a number of steps in the process which are not well understood: one is the mechanism of the transport through the cuticle of the leaf and another one is the deposit formation and its impact on availability of AI. After the droplet is deposited on a leaf surface, spreading and drying of the droplet with associated changes in both AI and surfactants leads to an initial spray deposit that can be formed in different patterns. The scanning electron microscope (SEM) is an effective instrument for studying the physical formulated surfaces, but it will be shown later that is not the best technique to measure chemical distribution. As previous studies have shown<sup>46,145</sup>, neither the leaf surface structure nor contact area of deposit alone show correlations with uptake efficacy, although it is reported that deposit distribution can affect uptake<sup>139</sup>, or is even thought to be crucial for penetration<sup>140</sup>. Therefore, deposit structure is a key element in the physical transfer process, as it affects the interface between pesticide and leaf surface.

SEM images are supported by energy dispersive X-ray spectroscopy (EDS) to provide direct evidence for the existence and distribution of specific elements in a solid sample at the microscale level. Although EDS does not detect organic molecules, it gives information about the elemental constitution. A major disadvantage of this technique is the lack of any chemical sensitivity to detect what components remain at the leaf surface.

On the other hand, Raman spectroscopy is a well-established technique for the qualitative and quantitative investigation of chemical products including Raman mapping. Because the intensity of the Raman scattered light is proportional to  $1/\lambda^4$ , the most common lasers used in Raman spectroscopy are in the visible range of electromagnetic domain (400–660 nm). Most commercial Raman systems generally acquire data from a point, but in this chapter it is shown how to collect data from a larger area.

## **6.2 Experimental**

For the experiments shown in this thesis, agrochemical droplets were deposited on silane-coated glass substrates (Section 3.3). The droplets were dried on the surface, then two different techniques were used for chemical characterization of the sample: energy dispersive X-ray spectroscopy (EDS) and Raman spectroscopy. Raman and EDS analyses were done approx. 1 and 24 h after droplet application respectively. Samples were covered with 10 nm of gold for EDS experiments.

## 6.3 Results

Figure 6.1 shows chemical maps from a SEM image of deposits formed from a) Surf1 1 g/L + AI and b) Surf2 3 g/L + AI by EDS. For Surf1, the spatial distribution of Tebuconazole was determined using X-Ray emissions of nitrogen (N, 0.392 keV), and chlorine (Cl, 2.61 keV) since these two chemical elements are not present in the Surf1 structure. The localization of the adjuvant was determined from the X-rays of carbon (C, 0.277 keV). The images show that the puddle around the edge of the droplet in Figure 6.1 a) is Surf1.

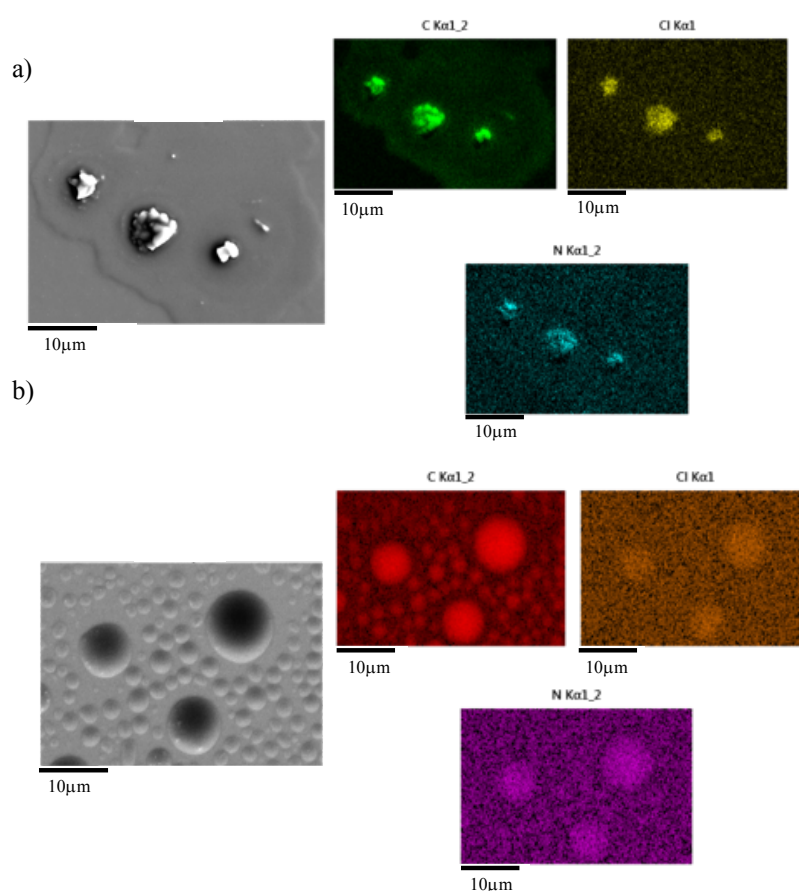


Figure 6.1: Electron image and element map of a deposit formed from a) Surf1 1 g/L + AI and b) Surf2 3 g/L + AI studied by energy disperse X-ray spectroscopy attached to SEM.

However, this technique is not sensitive enough to be able to detect if some of the AI molecules are dissolved in the surfactant and this is the reason why Raman spectroscopy was used. In case b) as Surf2 is an amidoamine-based surfactant, the only

element that is not present in the surfactant structure is the Cl. Raman spectroscopy was also used to study the co-localization of the surfactant and the AI.

A schematic of the Raman spectrometer is shown in Figure 6.2.

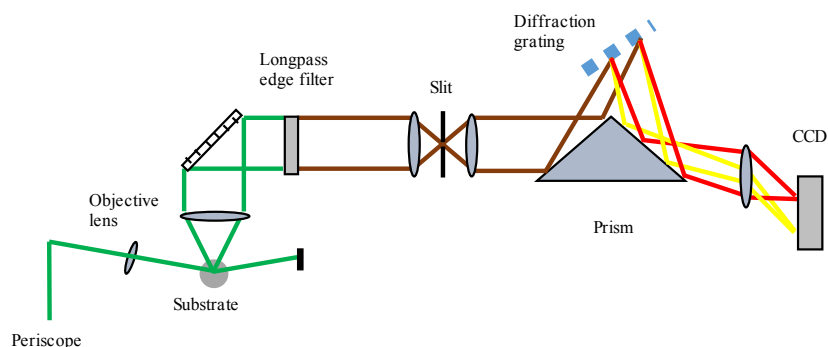


Figure 6.2: Schematic of the beam path within the Raman spectrometer.

The laser emits light at 532 nm (Opus 532, Laser Quantum, Manchester) which is delivered to the spectrometer (Renishaw). The beam passes through a polarising beam splitter and then a half-wave plate, allowing either S or P polarized light to reach the sample. S polarized was chosen since this polarization gave the highest signal levels. The beam then passes through a telescope that expands and collimates the beam using a -25 and a +125 mm lens. After the telescope, there is an iris which is left open during normal operation of the experiment, but which can be contracted to aid with alignment. The beam is then reflected from a 90° mirror to a periscope to the final mirror. The beam is focused onto the sample using a gradient index lens ( $f=120$  mm). The incident light is fixed to an angle of 73°. The scattered light passes through a longpass edge (Semrock, LP03) filter which removes the Rayleigh scattered component.

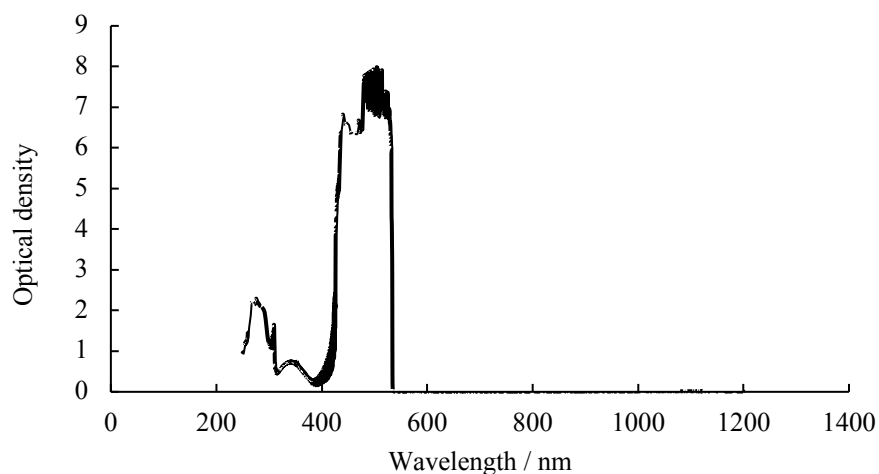


Figure 6.3: Optical density curve for the long pass filter used to block the Rayleigh scattering.

The light enters the spectroscope component through a 200- $\mu\text{m}$  slit, thereby ensuring that divergent light from out-of-focus areas of the sample is removed. The light is reflected by a prism onto a diffraction grating ( $1800 \text{ line mm}^{-1}$ ), which disperses light according to its wavelength. Finally, the light passes through a focusing lens and then onto the CCD camera, which records the intensity of light across it. The lens ensures that all light with the same angle (i.e. the same frequency) is focused to the same point on the CCD.

The scattered radiation was collected through a 0.55 NA objective (Olympus) and directed to the spectrometer. Data were acquired over a fixed wavenumber range including the C-H stretching region (from  $2600$  to  $3400 \text{ cm}^{-1}$ ) of the Stokes scattering. Reference spectra from the raw surfactants and AI were collected over the same range. The Raman instrument was calibrated using the  $\nu_1$  line of silicon at  $520.7 \text{ cm}^{-1}$ . Silicon substrates were selected since it is non-fluorescent and has a Raman spectrum that does not overlap with C-H stretching bands at around  $2900 \text{ cm}^{-1}$ .

The samples were mounted in a commercial microscope (Leica DM LM). The position of the sample could be adjusted using a three-axis translation stage (Newport).

For the measurements of the different spectra, the acquisition time was 10 s and 3 accumulations were summed in order to improve the signal-to-noise ratio. The reason why this option was used instead of using 30 s and 1 accumulation time was to avoid saturating the detector at longer exposures.

Figure 6.4 shows the raw spectra of the two surfactants and AI, dominated by the C-H stretching mode of the alkyl chain and the EO groups of the surfactant and the alkyl groups of the AI below 3000  $\text{cm}^{-1}$  and by the C-H stretching mode of the aromatic groups of the AI above 3000  $\text{cm}^{-1}$ .

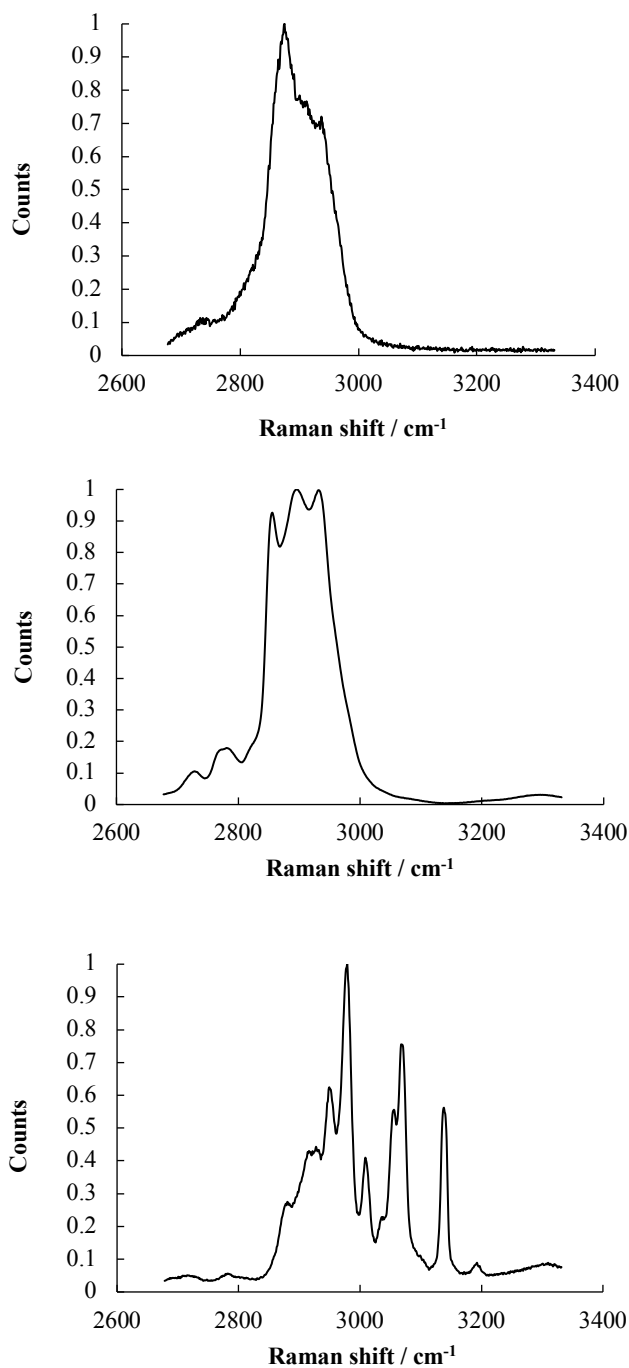


Figure 6.4: Spectra of the neat chemicals: a) Surf1, b) Surf2 and c) Tebuconazole.



In order to check the possible fluorescent background from the substrate and to find out if any substrate peaks overlapped with the Raman spectra of solutions, clean silicon substrates were subjected to Raman spectroscopy (Figure 6.5). There is an offset of about 20 counts for each acquisition time; a total of 60 counts, and also there is a mixture of dark current which is 2 counts/s plus signal.

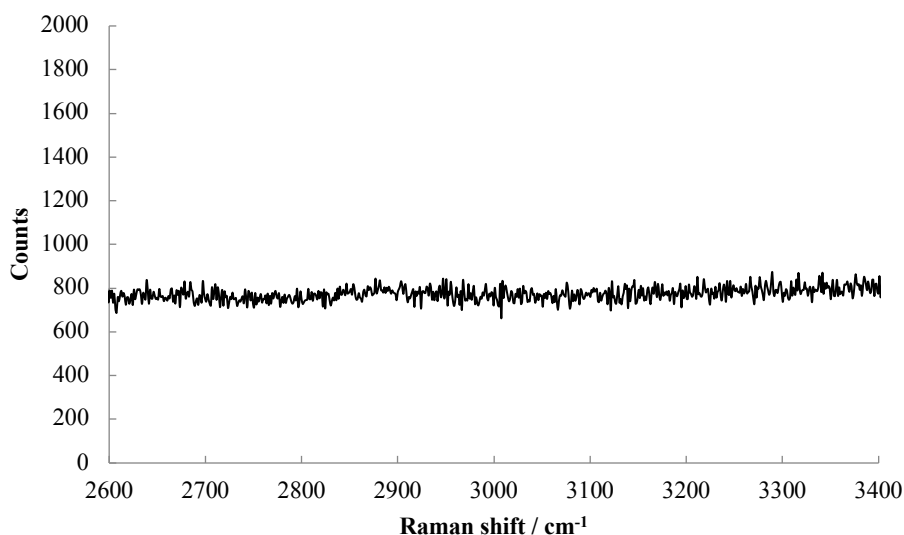


Figure 6.5: Raman spectrum of silicon substrates used in this thesis (500mW, 10 s, 3 accumulations).

The Raman imaging system is described in Figure 6.6. The sample used is the same as for Raman spectroscopy experiments. A tunable bandpass filter (TBP) (Semrock, centre wavelength 628 nm, 20 nm bandwidth) is mounted on a motorized stage so that the angle may be computer controlled. The beam is delivered by the mirrors and through the lens ( $f = 120$  mm) to give an imaging spot size of  $50 \times 40$   $\mu\text{m}$ .

The spectral images were used to construct maps of component distribution using an in-house MATLAB fitting function which was used in the experiments described in this thesis (code written by M. Possiwan).

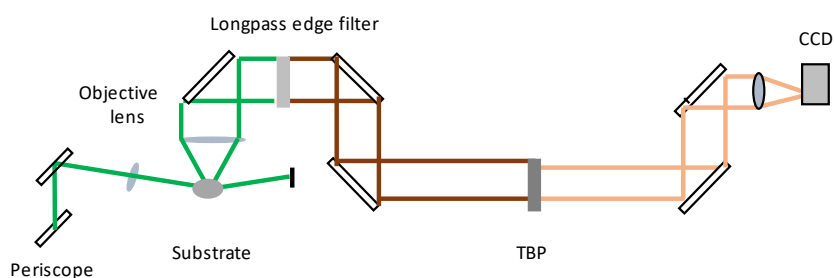


Figure 6.6: Schematic of the imaging path within the Raman spectrometer.

Raman imaging experiments were carried out to investigate the phase separation and the co-localization of the surfactant and the AI on the dried deposit on the silica surface. Different filter angles were used to image separate regions of the spectrum and combined to determine the composition of surfactant and AI across the deposit. In experiments, five different filter settings were used:  $0^\circ$ ,  $4^\circ$ ,  $6^\circ$ ,  $14^\circ$  and  $16^\circ$ . The transmission curves for the different filter angles are shown in Figure 6.7 with the spectrum of Surf1 and the AI. Spectra can also be collected in the same experiment with a few mirror flips. In order to get the Raman imaging, for each measurement the acquisition time was 30 s with a single accumulation and a centred Stokes shift of  $2900\text{ cm}^{-1}$ .

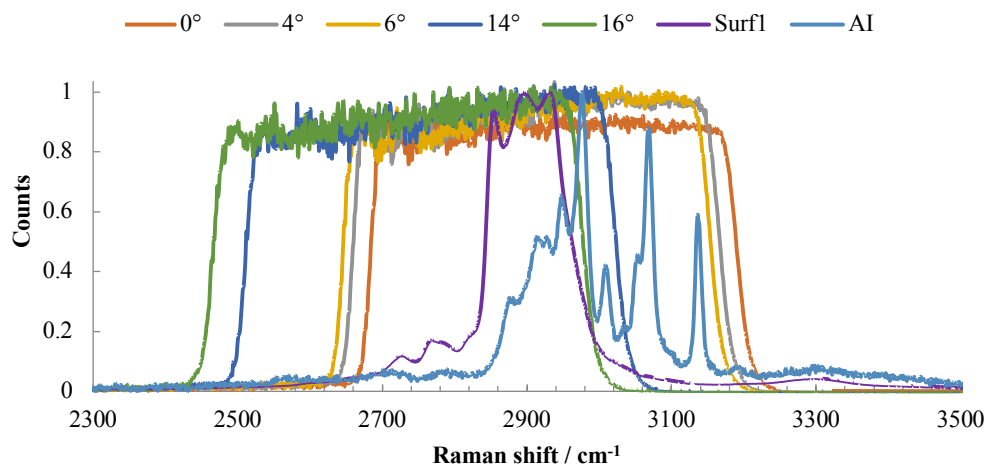
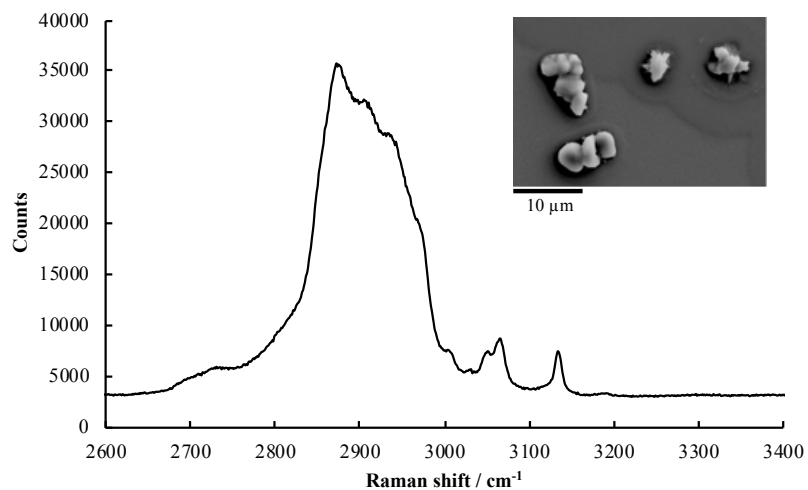


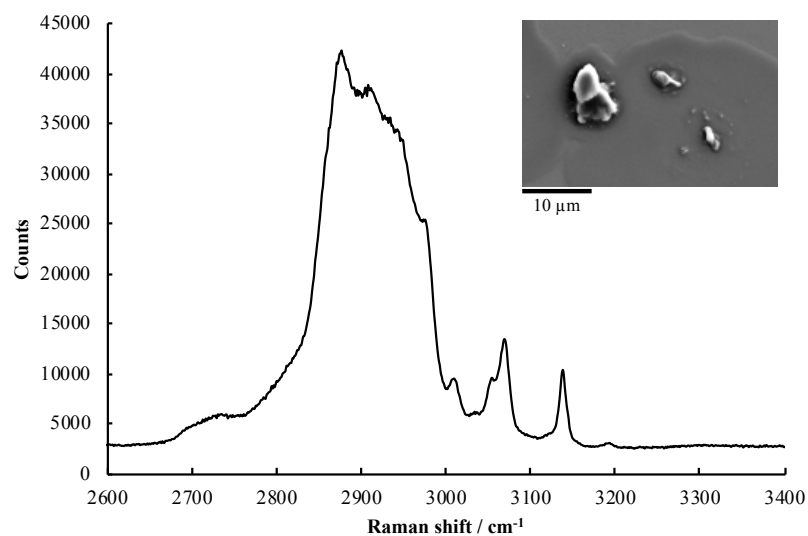
Figure 6.7: Normalised transmission profiles to the maximum transmission of the filter angles  $0^\circ$ ,  $4^\circ$ ,  $6^\circ$ ,  $14^\circ$  and  $16^\circ$  used in fitting procedure and Raman spectrum of Surf1 (purple) and AI (blue).

Raman spectra were taken from different parts of the deposit, identified by optical microscopy, in both formulations for Surf1 + AI and Surf2+ AI at 1 g/L and 3 g/L. A SEM image of the whole deposit is also shown to indicate the areas selected.

a)



b)



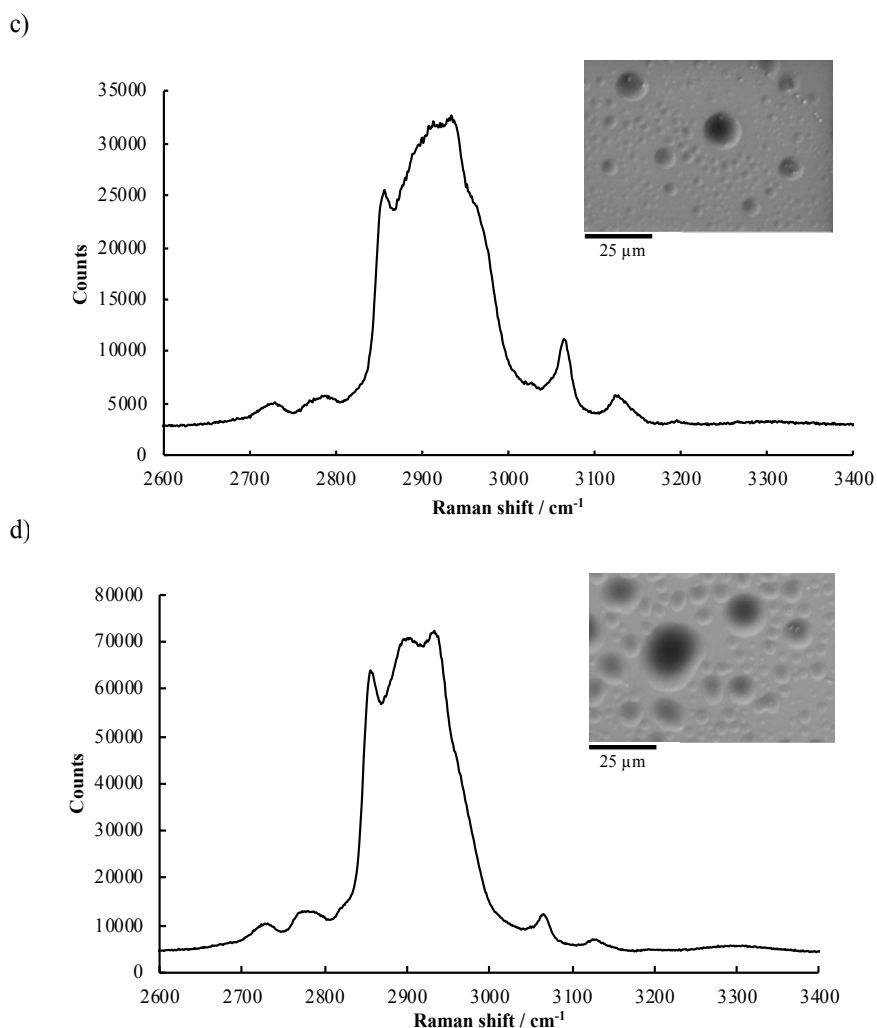


Figure 6.8: Raman spectrum of the area shown in the SEM image of deposits formed from: a) Surf1 1 g/L + AI, b) Surf1 3 g/L + AI c) Surf2 1 g/L + AI and d) Surf2 3 g/L + AI.

Both surfactant and AI can be distinguished on the spectra but their relative intensities changed significantly during the measurements across the deposit for Surf1 as the distribution of AI crystals are different. However, for Surf2 the relative intensities were the same for each concentration.

Spectral images from different filter angles were used to reconstruct maps for the components in the deposit using an in-house written fitting program in MATLAB. For the fitting procedure, intensity profiles between 2600–3400  $\text{cm}^{-1}$  for all filter angles used were recorded together with component reference spectra of Surf1 or Surf2 and AI. The intensity profile describes the Raman shift region ( $506 \text{ cm}^{-1}$  wide) contributing

to images at different filter angles. For every filter angle, the intensity profile was multiplied by the reference spectra intensity and the intensity summed. This gives an expected intensity profile over all filter angles for each component. Over the filter angles imaged, the component intensity profiles are fitted against the measured intensity variation for every pixel. The weighting factors applied to the component intensity profiles during the fitting are used to reconstruct component maps from the spectral images and the expected spectrum at each pixel can be determined.

Figure 6.9 shows Raman imaging results of a deposit formed from Surf1 + AI on silicon substrate (SEM image corresponds to SEM image in Figure 6.1 a).

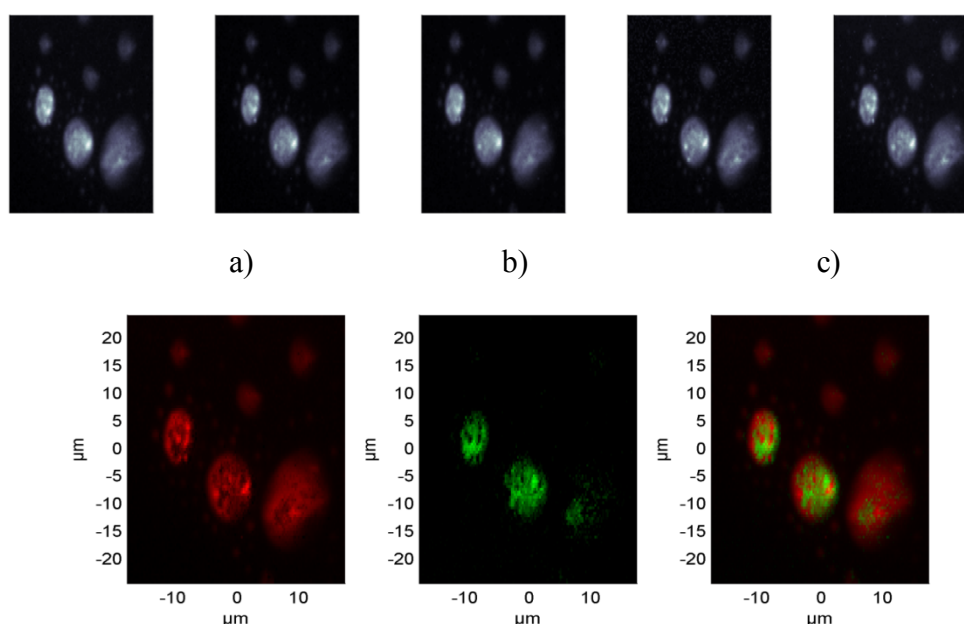


Figure 6.9: Raman imaging component maps of Surf1 and AI reconstructed from spectral images acquired over 30 s for five filter angles ( $0^\circ$ ,  $4^\circ$ ,  $6^\circ$ ,  $10^\circ$  and  $16^\circ$ ) using fitting procedure described above. (a) Surf1; (b) AI; (c) overlay of Surf1 and AI component maps.

Figure 6.9 shows both surfactant and AI associated. However, the detection of the AI molecules in the surfactant areas is still small. It has been shown that Raman spectroscopy is a useful technique to confirm the association between the adjuvants and the AI. Some improvements were tested in order to get a better resolution of this information.

The TBP that has been used for the previous experiments maintained high transmission even at high tilt angles. However, this filter has two drawbacks. First, every angle contains both compounds; at 0°, 4° and 6° basically both compounds are included, but at 16° most of the AI is left out and more contribution comes from the surfactant. Second, the transmission curve at each angle is wide and more fluorescence from the background is collected, which means more noise that degrades the quality of the data. The separation of three compounds in a similar case would be very difficult. The selection of peaks/regions that are specific for individual components will allow an increase in sensitivity and the specificity of the analysis.

A bandpass filter (BP) with a narrower shift region was therefore selected for the next experiments. The drawback of this new filter comes from the decrease in the transmission at tilted angles. (Figure 6.10).

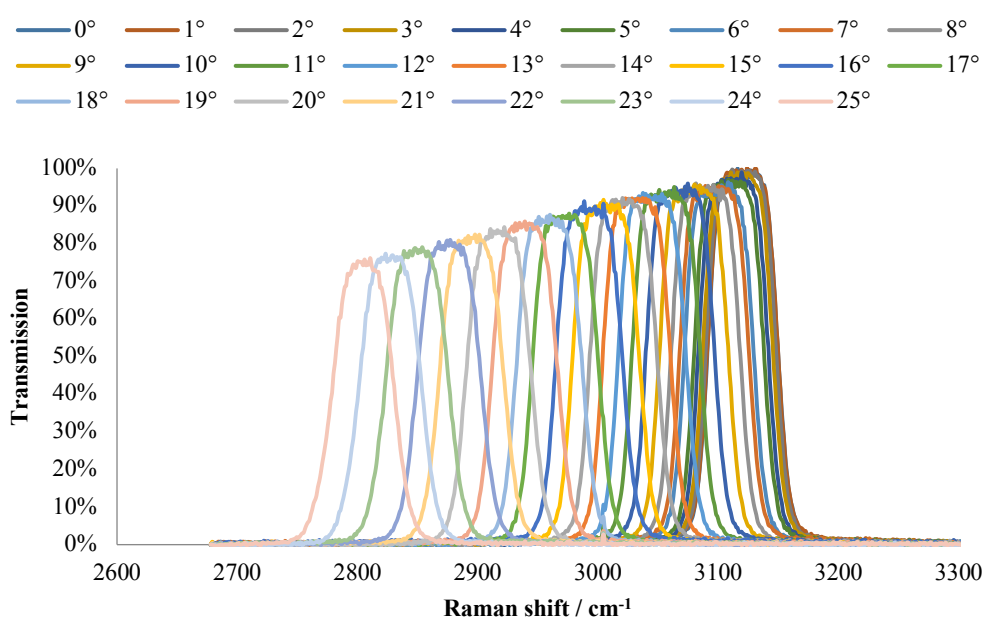


Figure 6.10: Transmission curves for the BP filter. (Semrock, centre wavelength 638 nm, 2.4 nm bandwidth)

The maximum transmission that can be achieved at the highest angle is still useful for the next experiments. The selection of angles with the BP filter to get the Raman images were in this case 0°, 10°, 15°, 20° and 22°. When the BP filter is set to 0° and 10° the only bands that should be observed are from the AI. When the filter is at 18°,

20° and 22°, the two species contribute to the image, but in different ratio, being higher for the surfactant (Figure 6.11).

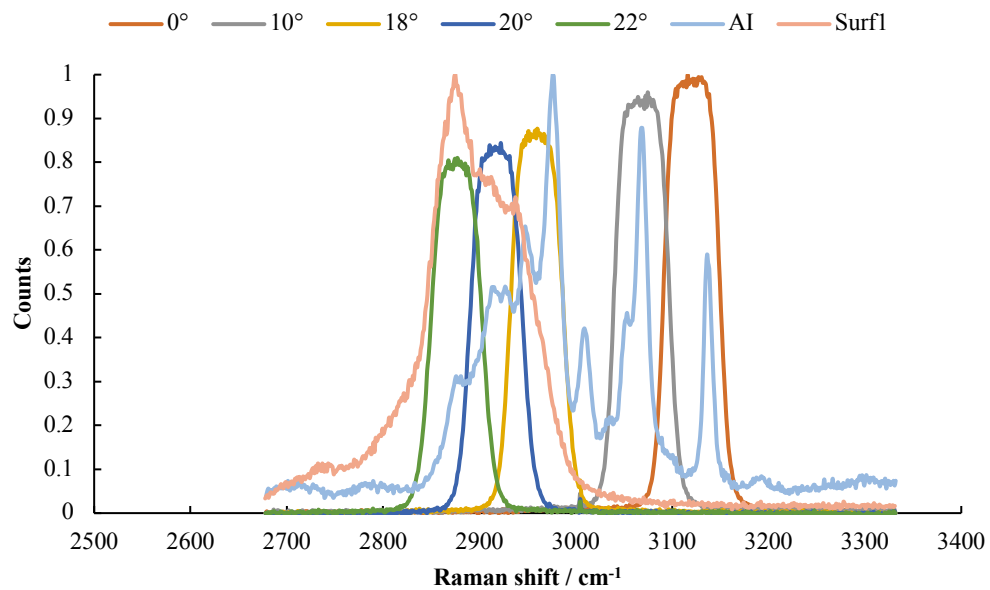


Figure 6.11: Normalised intensity profiles of filter angles 0°, 10°, 18°, 20° and 22° used in fitting procedure and Raman spectrum of Surf1 (pink) and AI (blue).

The BP filter allows signals between two specific frequencies to pass and discriminates against signals at other frequencies. The comparison of the transmission of the light at different wavelengths for the TBP and the BP filter is shown in Figure 6.12.

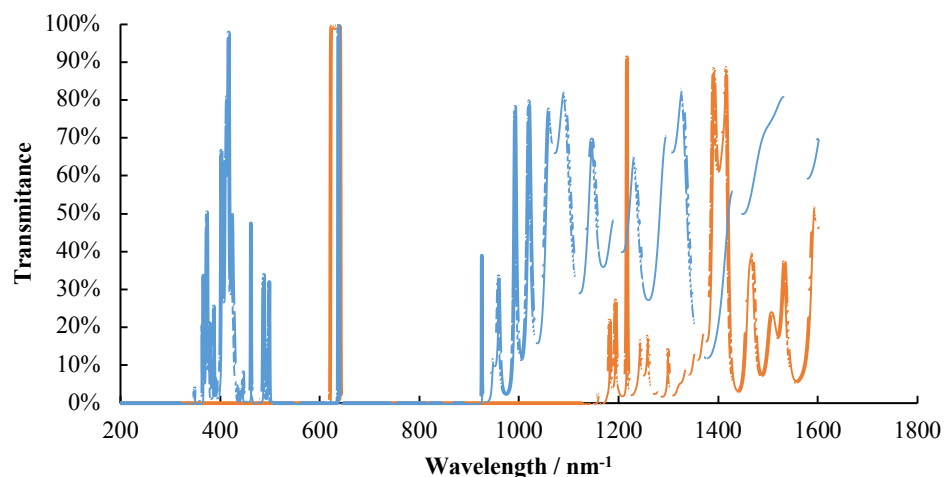


Figure 6.12: Transmission curves for both filters: TBP (orange) and BP (blue) filters.

The transmission of the light above 800 nm<sup>-1</sup> is blocked with the long edge filter that is in the set up (Figure 6.2) The main difference between both filters is the transmission

of the light at wavelengths between 340–530 nm that corresponds to the UV region of the spectrum. When the BP filter was used, the UV light transmitted gave a brighter background on the Raman imaging results giving rise to a bad interpretation of both surfactant and AI positions on the sample. This might be due to a multiphoton process: two-photon absorption and a normal (one-photon) fluorescence.

One alternative to get rid of this extra light is by using an extra UV filter. Another option, as was done in this thesis, was to align both filters in series, where the TBP filter was fixed at 0°, while the BP filter can be tilted in order to get the wavelengths required. The condition to be able to do that is that when the BP filter is tilted at higher angles, all the wavelengths ranges from the BP are within the wide wavelength of the TBP filter at the fixed position, 0° (Figure 6.13).

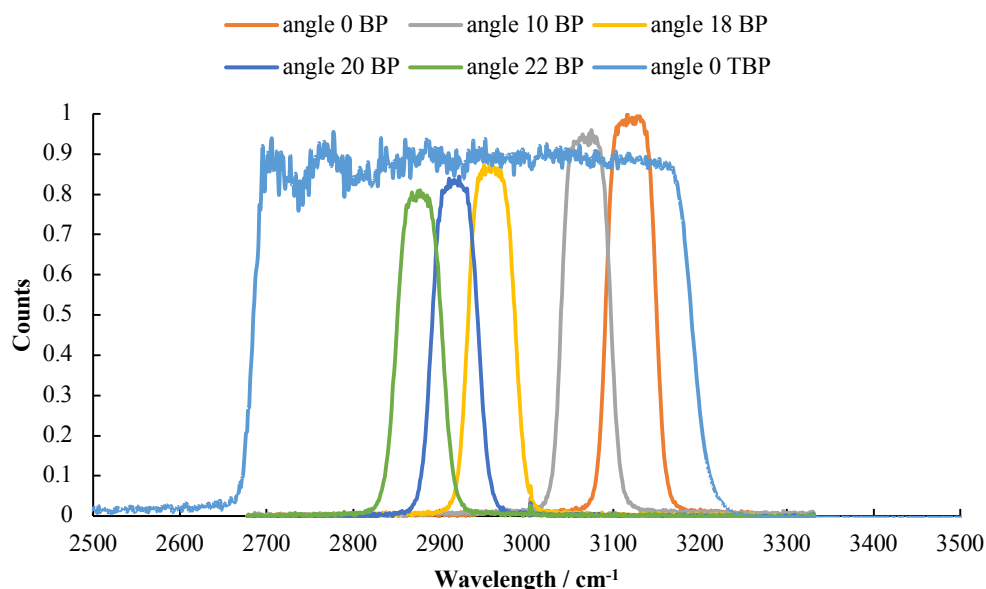


Figure 6.13: Overlapping of transmission curves for both filters: TBP fixed at 0° and BP filter at different angles: 0°, 10°, 18°, 20° and 22°.

Figure 6.14 and 6.15 show Raman imaging results for Surf1 3 g/L + AI and Surf2 3 g/L + AI respectively on silicon substrate for the new set up. Also, an optical image and a Raman spectrum of the specific area are shown with the results.



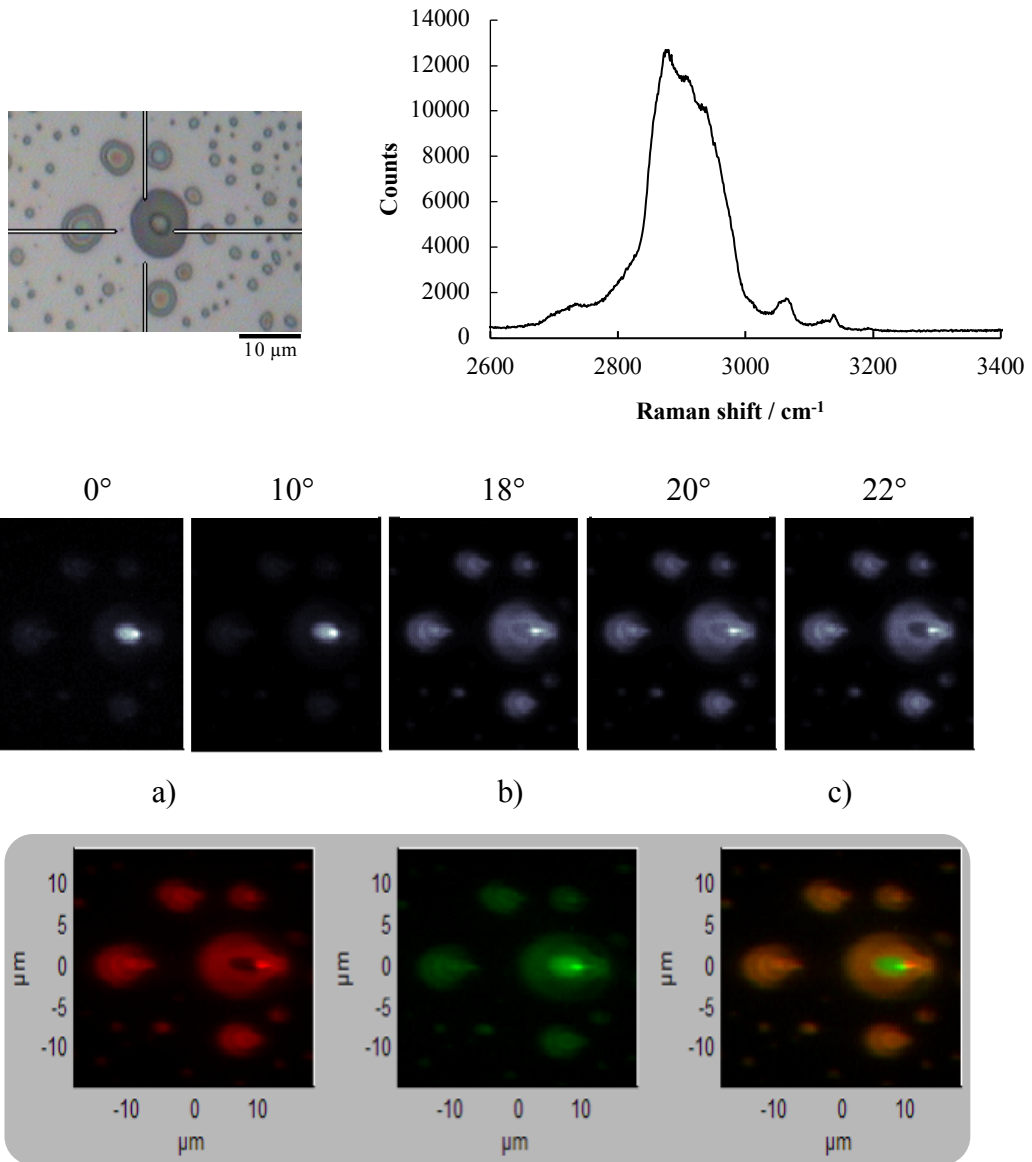


Figure 6.14: Raman imaging component maps of a deposit formed from Surf1 3 g/L and Al reconstructed from spectral images acquired over 30 s for five filter angles using fitting procedure described above. (a) Surf1; (b) Al; (c) overlay of Surf1 and Al component maps.

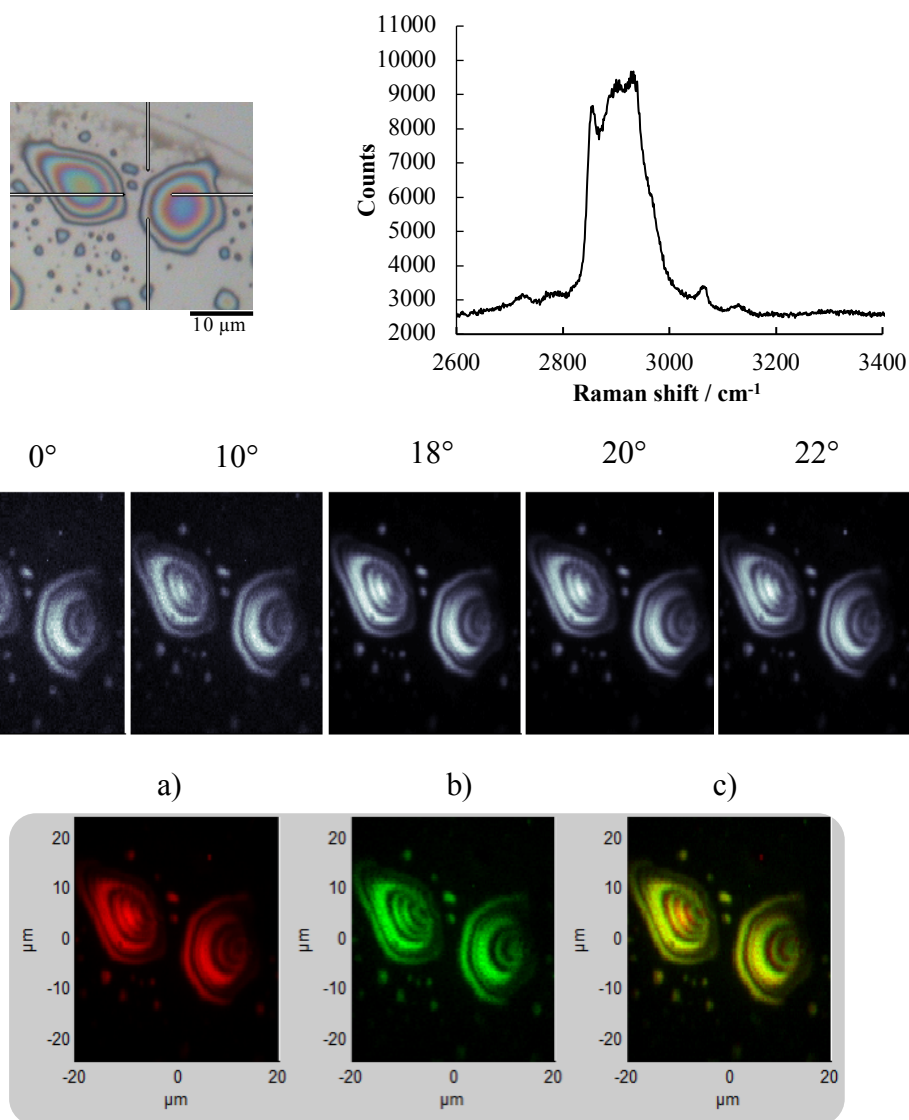


Figure 6.15: Raman imaging component maps of a deposit formed from Surf2 3 g/L and AI reconstructed from spectral images acquired over 30 s for five filter angles using fitting procedure described above. (a) Surf2; (b) AI; (c) overlay of Surf2 and AI component maps.

Figure 6.14 and 6.15 show the component maps for both Surf1 and Surf2 and AI. Modifications in the set up improved the sensitivity for the detection of the AI molecules in the Surf1 puddle and thus, the association between both surfactants and the AI molecules can also be confirmed.

Figure 6.15 shows strong fringes. When the beam hits the sample, there are reflections from the silica and from the top of the droplet and both interfere with each other. Also, the Raman light reflected from the substrate interferes with the Raman light emitted away from the substrate. These contributions combine to give rise to these bright and

dark rings. P-polarised light gave less interference but the amount of signal collected was only half as large and fringes were still present. Also, it can be seen that the right side of the droplet in Figure 6.14 and 6.15 is completely dark because the light coming in is at an angle of  $73^\circ$ . The light coming in refracts giving a dark area at the back of the droplet where the illumination is very low (Figure 6.16).

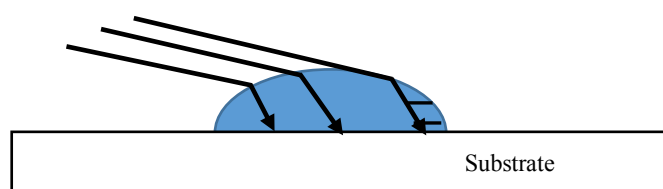


Figure 6.16: Schematic diagram of the path of the incident light through a droplet with a contact angle of  $73^\circ$ . The shaded portion of the drop has no light and it will be dark on the image.

One of the ways I tried to solve this problem was by changing the angle of the incident light from  $73^\circ$  to  $53^\circ$  (Figure 6.17). However, the modification of the incident angle did not give a better result. It is worth mentioning that the bright spot might arise from the lensing effect of the droplet focusing the incident beam.

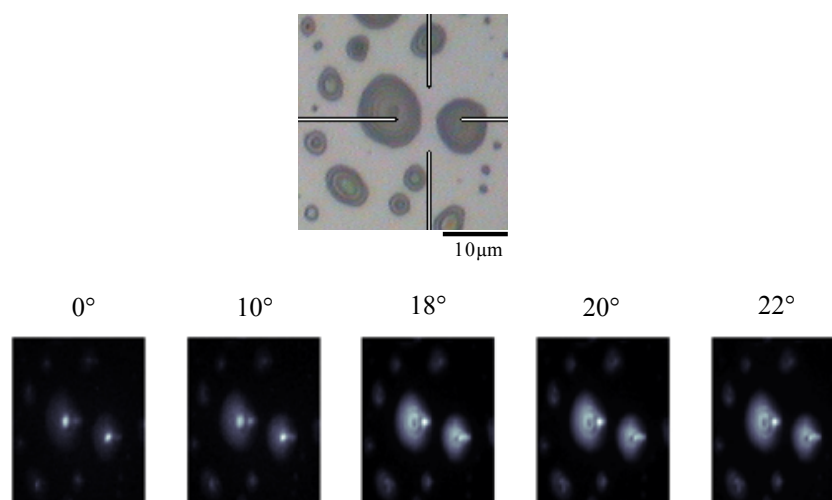


Figure 6.17: Raman imaging component maps of a deposit formed from Surf1 and AI with an angle of incidence of  $53^\circ$ .

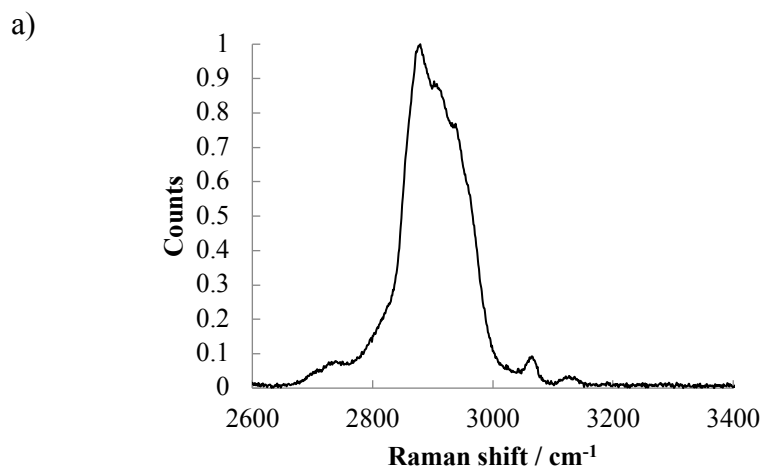
## 6.4 Quantification of AI and surfactant ratio on a deposit

The combination of Raman spectroscopy and  $^1\text{H-NMR}$  was used to quantify the ratio of AI and surfactant on specific areas of the deposits. Solid Tebuconazole was mixed with neat Surf1 or Surf2 and heated up in order to dissolve the AI. Then, a small sample was added to DMSO and a  $^1\text{H-NMR}$  spectrum was taken. Table 6.1 shows the ratio of the areas between the surfactant and AI peaks.

Formulation	Molar ratio surfactant peak : AI peak
1g Surf1 + 0.625 g AI	1.02
3g Surf1 + 0.625 g AI	2.97
1g Surf2 + 0.625 g AI	1.42
3g Surf2 + 0.625 g AI	4.61

Table 6.1: Ratio of surfactant and AI in NMR spectra.

The same samples were also analysed with Raman spectroscopy (Figure 6.18). The raw surfactant spectrum was subtracted from the spectrum of the solution so that only the AI spectrum remained. In the same way, the remaining AI spectrum was subtracted from the spectrum of the solution to leave only the surfactant spectrum. Thus, the intensity of these peaks ( $3062$  and  $2875\text{ cm}^{-1}$ ) can be compared to quantify the ratio of each component.



b) c)

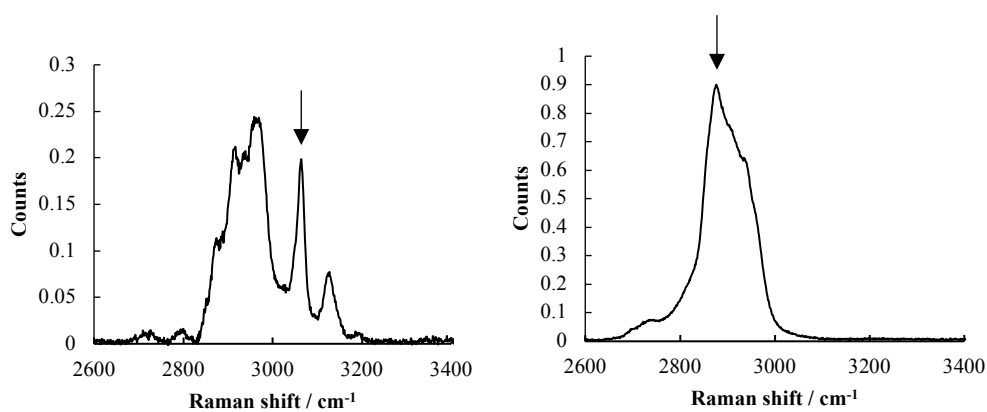


Figure 6.18: Quantification of the amount of each compound: b) amount of AI, c) amount of surfactant) in the residue analysed previously by  $^1\text{H-NMR}$  a) top spectrum).

When the peaks were compared as described the sensitivity factor can be calculated. The sensitivity factor ( $S_f$ ) is defined as the relationship between the molar fraction and the intensities. It can be applicable to any formulation.

$$\frac{\text{moles AI}}{\text{moles Surf}} = S_f \frac{I(\text{AI})\text{at } 3066 \text{ cm}^{-1}}{I(\text{Surf})\text{at } 2875 \text{ cm}^{-1}} \quad \text{Eq. 6.1}$$

where  $S_f$  is the sensitivity factor. For the example shown in Figure 6.18 (Surf1 + AI), the sensitivity factor has a value of  $4.7 \pm 0.2$ .

A specific area of the deposit was analysed in order to quantify the amount of each compound by Raman spectroscopy (Figure 6.19). The selected area of the image has no visible AI crystals.

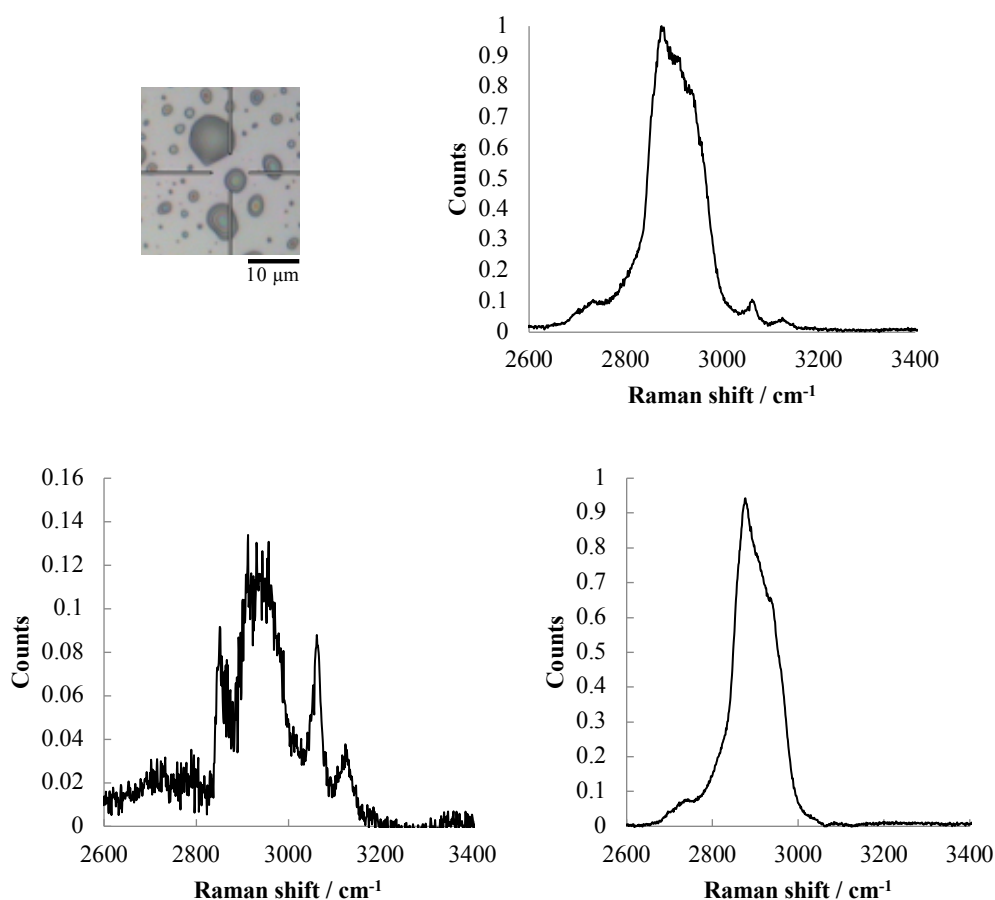


Figure 6.19: Quantification by separation of the spectrum of each component. The spectrum was taken from a dried deposit formed from a Surf1 3 g/L + AI solution (upper image).

Figure 6.19 shows the spectrum taken on a specific area of the deposit (upper image) and the amount of both compounds separately. The ratio of the AI/surfactant intensities at 3062 and 2876  $\text{cm}^{-1}$ , is 0.086 and 0.94 respectively, and was divided by the sensitivity factor, 4.7, to get the relative percentage of each component. In Figure 6.19, there is 30% AI and 70% of surfactant. However, this calculation will be different for different areas on the deposit and can be done for any formulation.

The same method can be applied to Raman imaging by calculating the number of counts in each map in order to get the sensitivity factor and convert intensities into composition.

## 6.5 Summary

Once the droplet is dried on the surface, two different techniques were used for the chemical characterization. Energy dispersive X-ray spectroscopy (EDS) provided evidence for the distribution of AI on the deposit. However, the disadvantage of this technique is the lack of chemical sensitivity to detect Tebuconazole in the thin surfactant film. Raman spectroscopy was a powerful technique for the qualitative and quantitative chemical composition of dried deposits on a surface. Also, with Raman imaging, chemical maps can be achieved. By knowing the chemical structure of the elements on a substrate, different filters were used to discriminate the areas where, in this case, AI is located with respect to the surfactant as AI has peaks above  $3000\text{ cm}^{-1}$ . Modifications in the set up improved the sensitivity for the detection of the AI molecules in the surfactant puddle.

The combination of Raman spectroscopy and  $^1\text{H-NMR}$  was used to get a quantitative analysis of the chemical composition of a selected area of the deposit. The intensity of these peaks were compared to quantify the ratio of each component and a sensitivity factor was obtained. The sensitivity factor ( $S_f$ ) is defined as the relationship between the molar fraction and the intensities. Thus, specific areas of the deposit were analysed to quantify the amount of each compound by Raman spectroscopy. As drop dries, the AI dissolves in the neat surfactant to increase the AI concentration from the solubility limit in micelles (1:10) to that in neat surfactant (1:2.4).

# Chapter 7

## 7. Franz Diffusion Cell: Penetration of Tebuconazole over a cuticular membrane (Clivia Miniata Regel).

### 7.1 Introduction

The fundamental requirement of an effective agrochemical treatment is the delivery of a dose of AI to the site of action<sup>9</sup>. Foliar uptake is a complex process involving a large number of variables. The efficacy of contact or systemic foliar-applied agrochemicals is influenced by their ability to penetrate the leaf cuticle. Cuticular penetration by chemicals is assumed to be largely a concentration-mediated diffusion process as explained by Fick's law (Section 1.6.1). Fick's law predicts that penetration of chemicals should be inversely proportional to cuticular membrane thickness. Although such a relationship has not been established in practice, cuticular structure is likely to have a major influence on foliar uptake<sup>141</sup>.

The role of the deposit form and distribution in the uptake of AI-adjuvant mixtures is a question that remains unanswered<sup>44,142</sup>. In spray applications of pesticides, foliar penetration commences when the spray is retained by the plant surface. Many studies have shown the effect of adjuvants on foliar uptake<sup>143,144</sup>. In all the cases adjuvants are required to act as a solvent and increase the reservoir of "available" material for uptake on the leaf surface. However, the mechanism of surfactant enhanced uptake of AI is still not fully clarified. In general, to understand interactions between the AI and the other formulation components, diffusion studies can be performed. These experiments



measure the amount of AI penetrating into or across a plant cuticle with respect to time. A particular problem with this type of study is the detection of the AI.

The use of *in vitro* static diffusion cells to assess AI permeability has evolved into a major research methodology, providing key insights into the relationships between membranes, AI and formulation. Franz-type diffusion studies frequently involve the use of synthetic membranes<sup>145,146</sup> to model real leaves. Although the artificial membranes will not model the cuticle perturbation effects undergone by biological samples, inferences regarding partitioning and diffusion phenomena can be made.

One of the aims in this thesis was to measure the penetration of Tebuconazole from a solvent system through the cuticle of the leaf. In order to approach the model as close to reality as possible the solution was studied as a solution (infinite dose system) and in the form of a droplets sprayed on the surface of the leaf (simulation of foliar penetration method, SOFP). The method used was a Franz cell methodology, where diffusion through plant membranes can be studied over time. These experiments were performed at AkzoNobel Surface Chemistry, Stenungsund (Sweden).

A schematic picture of the Franz cell equipment is shown in Figure 7.1.

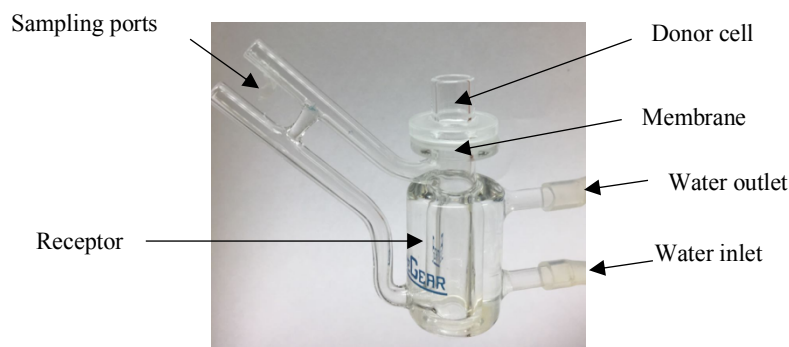


Figure 7.1: Schematic sketch of a Franz diffusion cell.

For the experiments, two main formulations were used: an alkyl ethoxylate, Surf1, and amidoamine-based surfactant, Surf2, at 1 and 3 g/L and a model active ingredient, 2.58 g of 25% SC Tebuconazole which contains 0.625 g of Tebuconazole.

In thermodynamic terms a system can be described by its Gibbs energy,

$$G = H - TS \quad \text{Eq. 7.1}$$

where  $G$  is the Gibbs energy,  $H$  is the enthalpy,  $T$  is the absolute temperature and  $S$  is the entropy of the system to obtain the chemical potential<sup>147</sup>. When temperature and pressure are constant, the Gibbs energy can be differentiated with respect to the number of molecules of a certain compound that is present in the system to obtain the chemical potential. At phase equilibrium, the chemical potential of component  $i$  is equal in all phases. If the system is not in equilibrium, differences in the chemical potential of component  $i$  are present, and a flux of molecules from high to low chemical potential takes place. This phenomenon is called diffusion and its rate is characterised by the diffusion coefficient ( $D_i$ ). All systems strive to minimize their free energy. If pressure and temperature are constant a negative enthalpy change ( $\Delta H$ ) or a positive entropy change ( $\Delta S$ ) produces a lower free energy. If the change in Gibbs energy of transferring a molecule from one location to another is negative, and thermal motion is present, it will transfer by means of diffusion. A two-phase system, connected but very different in their characteristics can contain very different levels of the same compound at the same chemical potential at equilibrium conditions. This phenomenon is called partition<sup>148</sup>. The partition coefficient describes the distribution of a substance between two phases.

## 7.2 Experimental

The preparation of surfactant solutions with and without AI was as follows:

- Alkyl ethoxylate surfactant (Surf1) + AI: with a desired concentration the samples were sealed and incubated at ambient temperature under constant agitation on a stir plate using magnetic stir bars for a day. After 24 h, samples were stored at 40 °C for 3 h to speed up the dissolution of the AI in the surfactant solutions. After 3 h, samples were stirred again for 8 more days at ambient temperature. These solutions were then used in the measurements, added to the donor compartment.
- Amidoamine-based surfactant (Surf2) + AI: with a desired concentration the samples were sealed and incubated at ambient temperature under constant agitation on a stir plate using magnetic stir bars for 4 h. Then, solutions were kept in an ultrasonic bath at 80 °C for 2 h and stirred again for 12 days.
- A control experiment containing no added surfactant was also included, thus AI is added to water and used as a reference.

*Clivia Miniata Regel* was used as a model membrane for the diffusion experiments. The upper (adaxial) surface *Clivia Miniata Regel* lacks stomata<sup>149</sup>. Cuticles were isolated from the adaxial side of the *Clivia* leaves using a dermatome (TCM 3000 BL, Nouvag AG, Goldach, Switzerland). Slices of 50 µm from the middle part of the leaf were taken and used as a membrane. Rings of Parafilm were appended to both sides of the membranes to avoid leakage (outer diameter 23 mm, inner diameter 16 mm).

The receptor compartment of the Franz cell was filled with degassed deionized water. Moreover, a deviation from the established SOFP method was to add surfactant solution above the CMC (3 g/L for both surfactants, 6 mL) to the receptor cell. Both set ups were compared.

The membrane was carefully put on the top, the upper side of the plant leaf facing the donor compartment. It was crucial that the water or surfactant solution is filled up, i.e. in contact with the membrane. The donor compartment was placed on the top. The system was checked for air bubbles at this point. The water + AI or surfactant solutions + AI were added to the donor cell (1 mL). For SOFP, the solutions were sprayed on the leaves and once they dried they were put in the donor compartment instead. Parafilm was used to cover the donor compartment and sampling ports during the experiment. The cells were kept under isothermal conditions at 25 °C and stirred with a stir bar.

Sampling was done from 1 min up to 7 days taking out 500 µL from the receptor cell (lower sampling port) and filling in degassed deionized water or surfactant solution in the receptor cell (upper sampling port) at the same time and same volume. The sample was stored in a vial in the fridge and liquid chromatography–mass spectroscopy (LC-MS) was used to analyse the amount of active ingredient present.

An internal standard (IS) solution (0.5 mL) was added to the samples extracted from the Franz cells in different vials containing the same volume (0.5 mL). The IS solution is made of 100 g of  $\text{MgCl}_2 \cdot 6\text{H}_2\text{O}$  and 100 µL of a stock solution containing hexadecylamine- $d_{31}$  (10 mg hexadecylamine- $d_{31}$  in 100 mL Methanol) in 1 L MeOH:IPA (50:50).

Quantitative analysis involves comparing the instrumental response obtained from the analyte (AI) in an unknown sample with that from one for which the concentration is known – the calibration standard. Calibration standards were prepared with IS and diluted 1:1 with MilliQ  $\text{H}_2\text{O}$  in LC vials prior LC-MS analysis. Ten calibration standards were used in these experiments with a concentration range from 0 to 326 µg/L and 0 to 1141 µg/L for electrospray and atomic pressure chemical ionization analysis respectively (Figure 7.2). The retention time for Tebuconazole and IS solution is 1.81 and 2.33 min respectively.

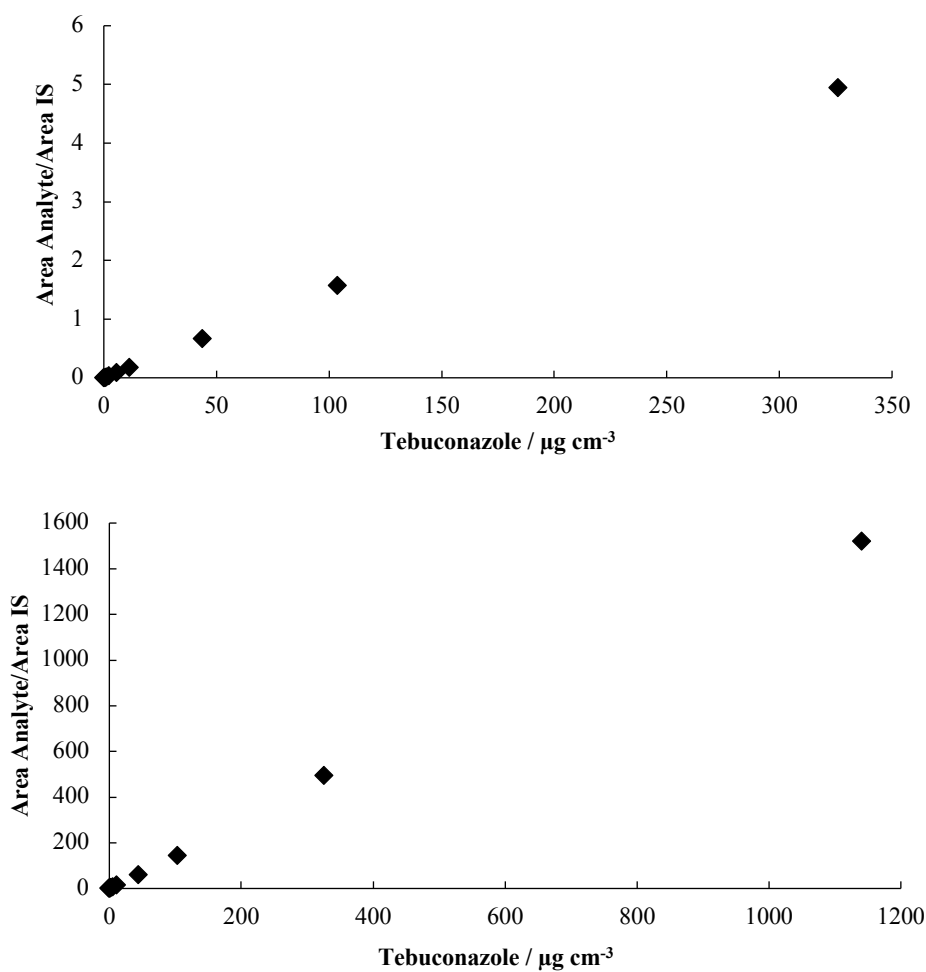


Figure 7.2: Calibration standards used for a) electro spray ionization and b) atomic pressure chemical ionization.

The Tebuconazole samples were then run on a Waters TQD mass spectrometer. Initially, electro spray ionization was used. However when ion suppression was observed, APCI ionization was used instead. The Electro spray and APCI analyses were validated with recovery tests, which mean spiking samples with known amounts of Tebuconazole and calculation of the recovery. The selectivity and specificity of the MS method was assured by using multiple reaction monitoring (MRM) parameters.

The following LC-MS parameters were used:

Column	Acquity UPLC BEH C18 1.7 $\mu\text{m}$ 2.1 $\times$ 50 mm	
Column Temperature	70 $^{\circ}\text{C}$	
Eluents	A= 2 mL TFA, 2.5 mL HAc, 2 mL $\text{NH}_3$ in 1 L MQ $\text{H}_2\text{O}$ B= 2 mL TFA, 2.5 mL HAc, 2 mL $\text{NH}_3$ in 1 L MeOH/IPA	
Flow Rate	0.7 mL/min	
Gradient	Time	% eluent B
	1	30
	0.5	30
	2.3	100
	3.3	100
	3.31	30
	4.3	30
Injection Volume	45 $\mu\text{L}$	

Compound	Parent Ion m/z	Daughter Ion m/z	Cone V	Collision eV	Collision Gas Flow mL/min	Dwell Time s
Hexadecylamine- $d_{31}$	273.50	66.10	25	30	0.3	0.161
Tebuconazole	308.16	69.97	40	20	0.3	0.161

Table 7.1: LC-MS parameters used for the detection of Tebuconazole in the receptor cell.

The concentration of Tebuconazole in the receptor compartment at the different sampling times is converted into cumulative amounts,  $AI_{cumulative}$ , by Eq. 7.2.

$$\frac{AI_{cumulative}}{area} = \sum_{i=1-(n-1)} \frac{C_{i_s} V_s}{a} \frac{C_{n_r} V_r}{a} \quad \text{Eq. 7.2}$$

where  $C_i$  is the concentration of AI in the receptor compartment at sampling time  $t_i$ ,  $V_s$  is the sampling volume,  $C_n$  is the concentration of AI at sampling point  $t_n$  and  $V_r$  is the volume of the receptor compartment.  $AI_{cumulative}$  is divided by the area,  $a$ , of the cuticle that the solution can penetrate through in order to normalise the data for comparison with cells of different designs. The standard deviation can be relatively high when working with leaves; the barrier properties of the CM are highly affected by temperature, humidity and maturation of the leaf<sup>150</sup>.

For the spray application studies, leaves were deposited, adaxial side up, on a glass substrate. They were sprayed by a stand-held spray applicator at a distance of 30 cm and left to dry. The amount deposited on the surface was determined by weighing the glass substrate with the leaf immediately after spraying and calculating the dose per unit area for each substrate. Spray solutions were prepared just prior to spraying to minimise any unwanted formulation aging effects. The container used to spray the agrochemical solutions is a PZ2 Classic from Aptar Actuator.

## **7.3 Results**

The infinite dose system is a broadly used method to study the penetration of AI through the cuticles of the leaf. However, this method is not related to the drying process as 1 mL of the agrochemical solution is added to the donor compartment and the cuticle of the leaf remains wet during the whole experiment. For this reason the simulation of foliar penetration (SOFP) method was also used. In SOFP, formulations are sprayed on the surface of the leaf to obtain a maximum coverage of individual droplets on the surface while avoiding the formation of a film of liquid. Some modifications were made on the Franz cell set up in order to increase the detection of the AI in the receptor cell.

### **7.3.1 Infinite dose experiments**

#### **a) water vs surfactant in the receptor cell**

Initially, experiments were performed to determine the detection of AI penetrated when the receptor cell was filled up with deionized water. 1 mL of Surf1 at 1 g/L and 3 g/L concentrations with AI was added to the donor compartment at the beginning of the experiment. Also, an AI aqueous solution was added to the donor cell as a control in order to study the penetration without surfactant added.

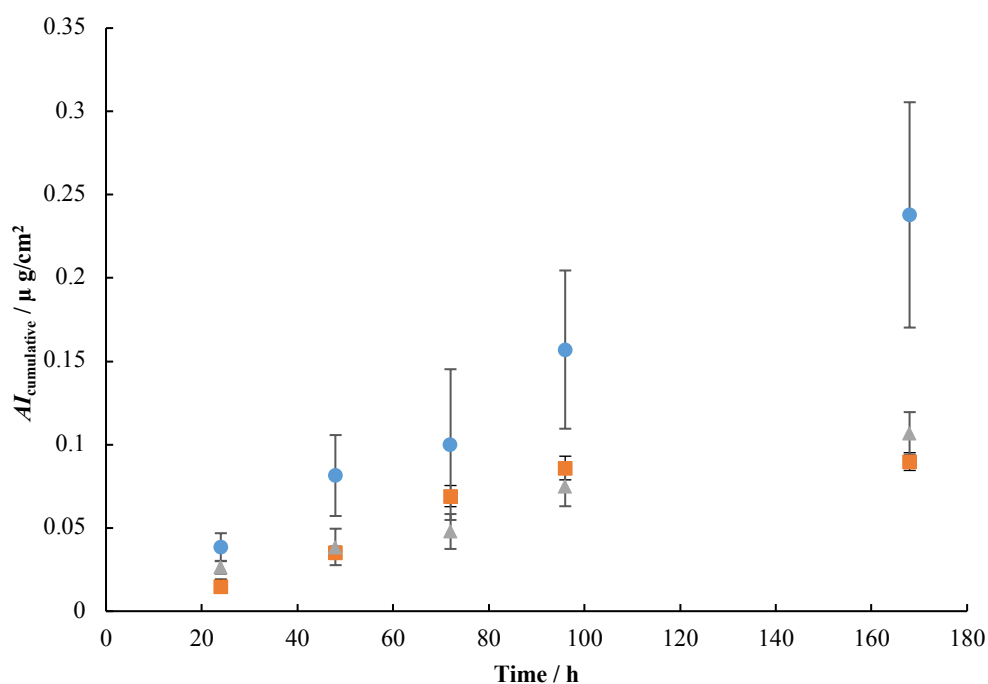


Figure 7.3: The cumulative amount of Tebuconazole in the receptor solution of the Franz cell for Surf1 + AI at two different concentrations: 1 g/L (grey triangles) and 3 g/L (blue circles) plotted against time when the receptor cell is filled with water. Error bars from 6 different measurements ( $\sigma_m$ ). AI without surfactant added used as a control (orange squares).

The control experiment, where no surfactant solution was added, and Surf1 at 1 g/L show very similar behavior. This might be due to the absence of micelles in the solution, so all the AI is present as monomers in solution or as crystals. The results suggest that Surf1 at 1 g/L is not softening the CM to enhance the diffusion of AI. When the concentration of Surf1 is 3 g/L, above the CMC, the detection of AI in the receptor cell is higher.

Compounds that are essentially insoluble in water may not partition freely into the aqueous receptor fluid. For the next experiments, all the conditions were kept the same with the only difference of the addition of Surf1 at 3 g/L added to the receptor cell (Figure 7.4).



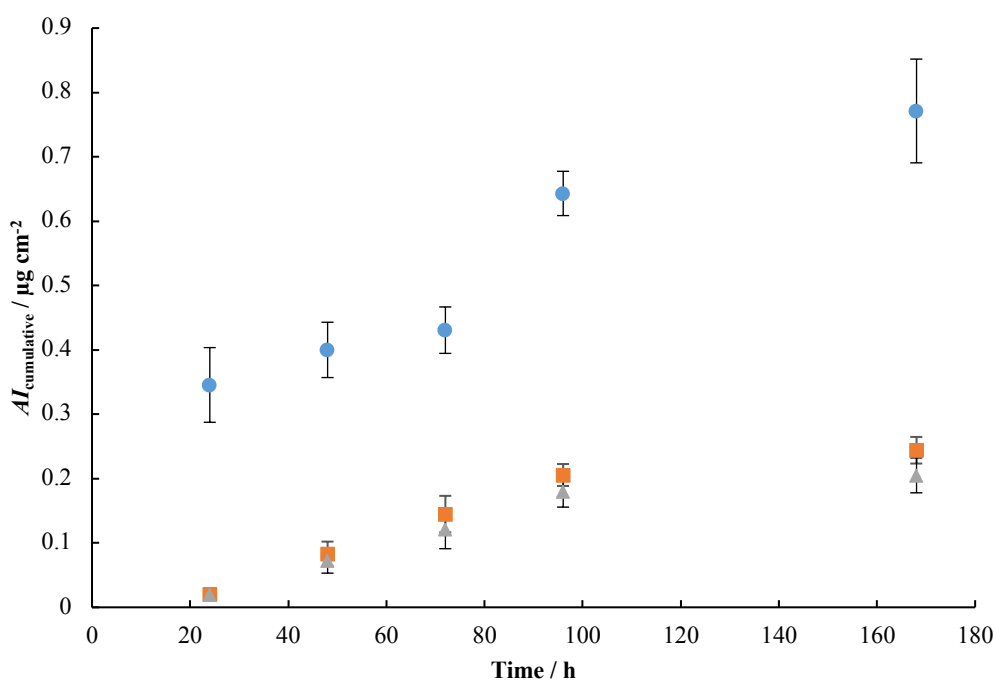


Figure 7.4: The cumulative amount of Tebuconazole in the receptor solution of the Franz cell for Surf1 + AI at two different concentrations: 1 g/L (grey squares) and 3 g/L (blue triangles) plotted against time when the receptor cell is filled with Surf1 at 3 g/L. Error bars from 6 different measurements ( $\sigma_m$ ). AI without surfactant added used as a control (orange circles).

As can be seen in Figure 7.4, when the water in the receptor cell was replaced with surfactant solution in a concentration above the CMC, the amount of AI detected in the receptor cell increased over time. By adding the surfactant solution in the receptor cell at the beginning of the experiment, the partition coefficient of AI between the cuticle and the receptor cell increased due to a decrease in the chemical potential of the AI in the receptor solution. All the subsequent experiments had surfactant solution in the receptor cell.

Figure 7.5 shows the penetration studies for Surf2 + AI at two different concentrations. Surf2 at a concentration of 3 g/L was added to the receptor cell.

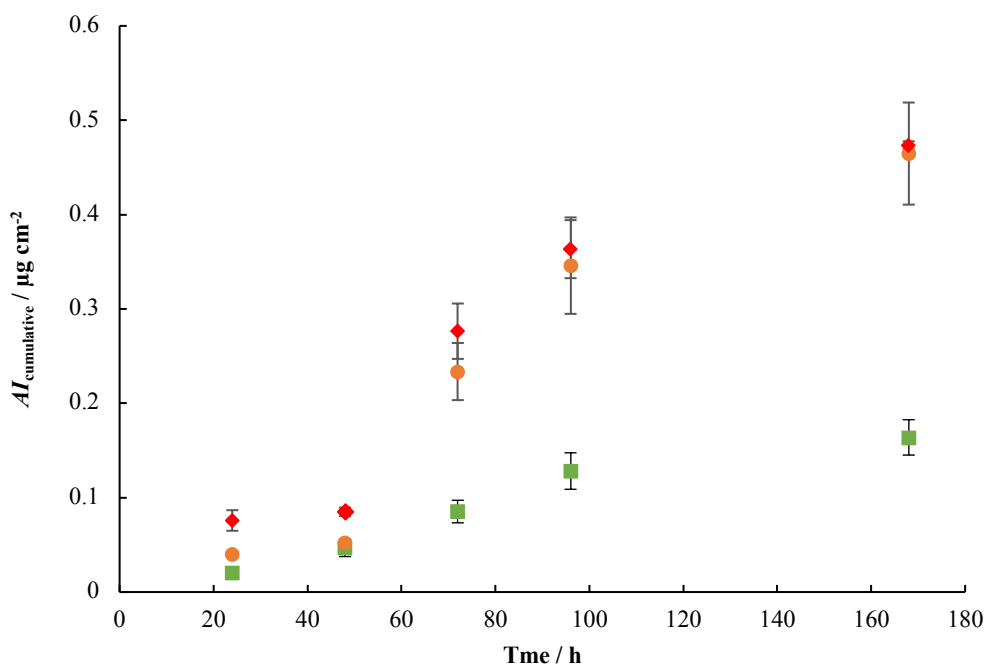


Figure 7.5: The cumulative amount of Tebuconazole in the receptor solution of the Franz cell for Surf2 + AI at two different concentrations: 1 g/L (orange circles) and 3 g/L (red diamonds) plotted against time when the receptor cell is filled with Surf1 at 3 g/L. Error bars from 6 different measurements ( $\sigma_m$ ). AI without surfactant added used as a control (green squares).

Figure 7.5 shows no significant difference between the two concentrations of Surf2, both of which are above the solubility limit. Figures 7.3, 7.4 and 7.5 show the control experiment with no surfactant added showing that AI penetration is improved by the addition of surfactants. Even though only cuticles from leaves with the same physiological age were selected, great variability in the AI penetration is seen for both formulations.

Initially, test experiments were carried out with Surf2 in the receptor cell. However, Surf2 extracted pigments from the membrane and we were concerned that changes to the membrane could influence the transport rate. Consequently, experiments were performed with Surf2 + AI in the donor cell and Surf1 at 3 g/L in the receptor cell to compare the influence of the type of surfactant in the donor cell.

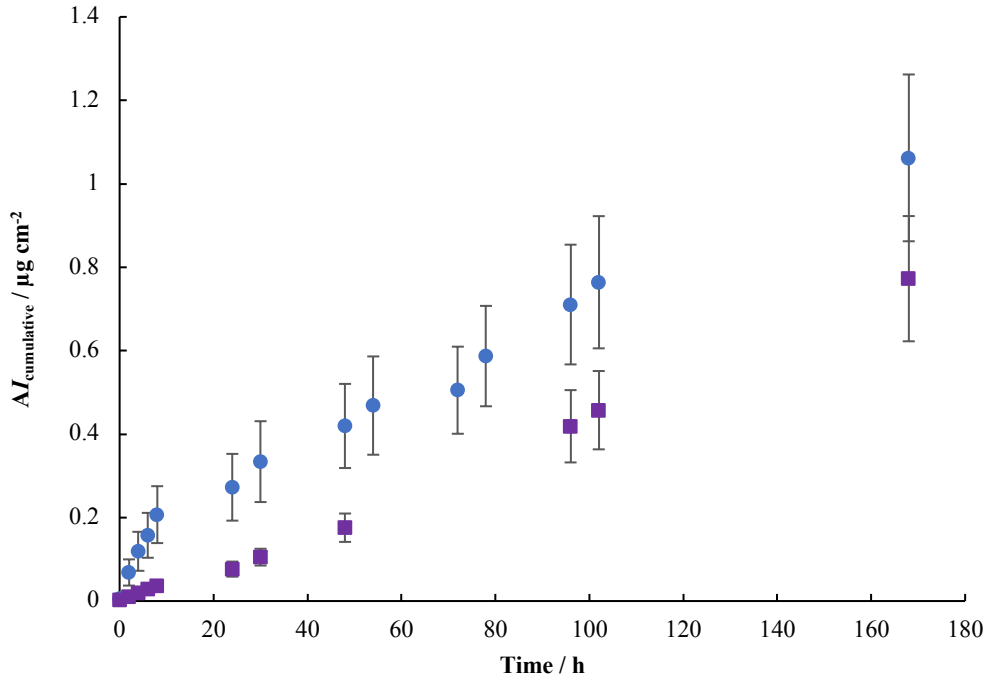


Figure 7.6: The cumulative amount of Tebuconazole in the receptor solution of the Franz cell for Surf1 + AI (blue circles) and Surf2 (purple squares) + AI at 3 g/L plotted against time when the receptor cell is filled with Surf1 at 3 g/L. Error bars from 6 different measurements ( $\sigma_m$ ).

The addition of a different surfactant in the receptor cell showed an increase in the transport rate behaviour for Surf2 (Figure 7.5 and Figure 7.6). Also, it seems that when Surf1 above the CMC is added to the donor cell, the penetration of AI is higher than Surf2. The presence of micelles might be more efficient at transporting Tebuconazole.

#### b) Effect of the cuticle selection

The penetration of AI through three different leaves with the same physiological age and also using cuticles from the same leaf were used in order to distinguish variability within a leaf from variability between leaves.

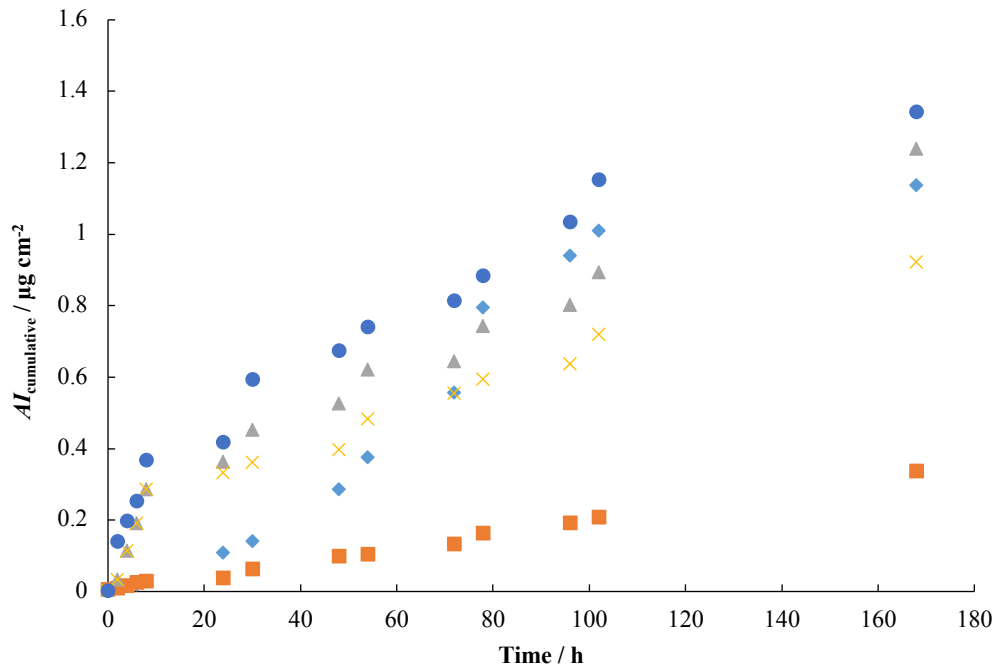


Figure 7.7: Penetration of AI in cuticles from the same age and same or different leaves using Surf1 3 g/L + AI. ( 5 different measurement in three different leaves. Leaf 1: blue diamonds and orange squares; leaf 2: grey triangles and yellow crosses and leaf 3: blue circles).j

Figure 7.7 shows that the variability in the AI penetration is still high either for leaves of the same physiological age of leaves or for cuticles cut from the same leaf.

### c) modification of waxes

For many years it was thought that adjuvants were improving the efficiency of pesticides by modifying the epicuticular wax layer, disrupting the cuticle structure and thus enhancing foliar uptake of the AI. Foy et al.<sup>10</sup> showed that surfactants modified the distribution and physical form of the herbicide on the cuticle surface by modifying its partitioning into the cuticles as well as the concentration gradient across the cuticle, and by modifying the permeance of the herbicide within the cuticle after surfactants are absorbed into the cuticle. Stock et al.<sup>151</sup> suggested that the surfactant may interact with barriers which impede diffusion of a compound, reducing resistance to penetration and facilitate absorption into the leaf. It was also proposed<sup>152</sup> that wax molecules could be solubilized in mixed micelles formed when pure surfactant micelles interact with the cuticle surface. However, the majority of the subsequent attempts to confirm surfactant-induced damage on leaves by SEM failed to detect any dramatic changes in wax morphology<sup>153</sup>.

In this thesis, modification of waxes by a surfactant solution prior to the addition of an agrochemical formulation was tested (Figure 7.8). Experiment A shows the same procedure explained above with the addition of Surf1 3 g/L +AI to the donor cell. However, for experiment B a surfactant solution (Surf1 3 g/L) was added to the donor cell for 48 h prior to the experiment with the agrochemical solution. After 48 h, the surfactant solution was sucked from the donor cell and was replaced with Surf1 3 g/L +AI.

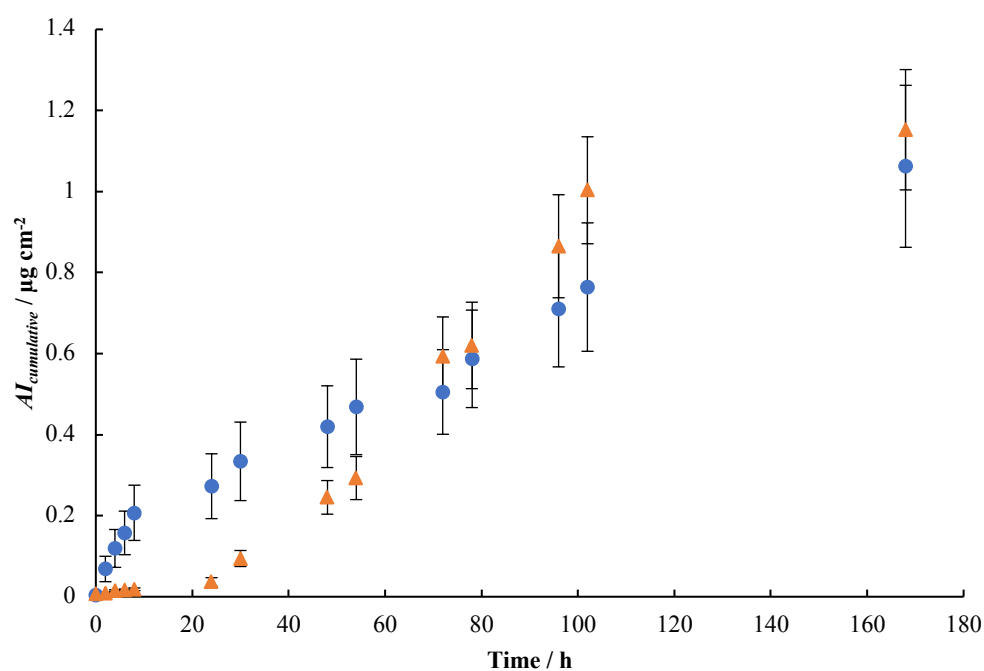


Figure 7.8: The cumulative amount of Tebuconazole in the receptor solution of the Franz cell for Surf1 3 g/L+ AI with (orange triangles experiment B) and without modified waxes (blue circles, experiment A). Error bars from 6 different measurements ( $\sigma_m$ ).

No increase of the penetration of AI at early stages of the experiment was observed. In fact, presoaking the surfactant solution reduced the initial rate of permeation through the membrane, possibly because the cuticle was older when the AI was first added, although the final level of AI penetration was very similar.

### 7.3.2 Spray application experiments

The spray deposits on a silane-coated glass substrates (CDO) are shown in Figure 7.9. On increasing the spray volume, a film is formed on the surface, thus, the volume was kept constant.

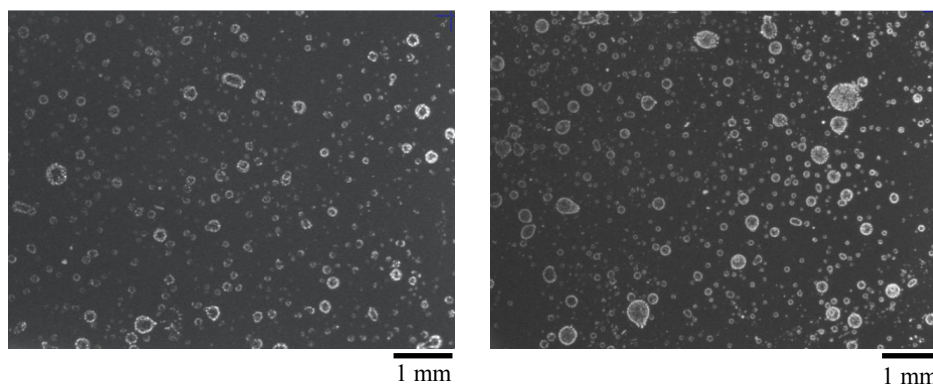


Figure 7.9: Spray deposits of Surf1 + AI (left) and Surf2 + AI (right) at a concentrations of 3 g/L on CDO-coated glass.

The dark field images from left to right correspond to Surf1 and Surf2 at 3 g/L + AI and show an even coverage by the spray with individual drops typically  $< 200 \mu\text{m}$  in size. The total coverage area was estimated with MATLAB (code written by Dr. L. Yang) giving an average value of  $9 \pm 3\%$  covered over  $30 \text{ mm}^2$ , for both Surf1 and Surf2 tested in 20 samples for each formulation.

Surf1 at 1 g/L and 3 g/L and Surf2 at 3 g/L with AI were sprayed on the cuticle on the leaf and when it was dried, cuticles were inserted into the Franz cell diffusion cell. Measurements were taken for 7 days. The same surfactant solution was added to the receptor cell, Surf1 3 g/L, in order to reject any influence from the surfactant solution used. Cuticles from the same and different leaves were also used.

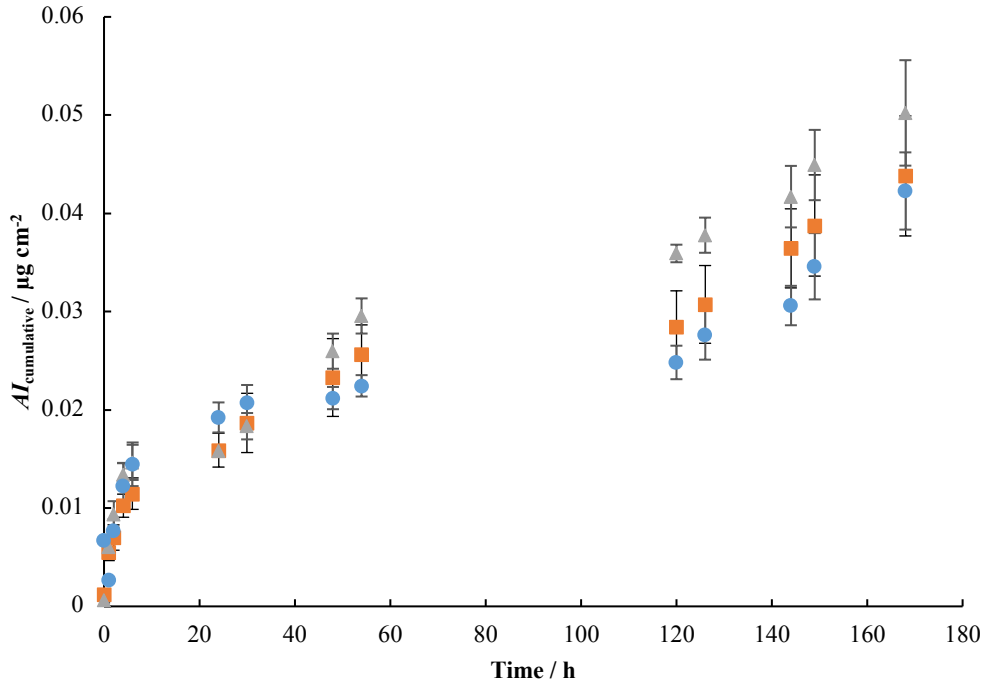


Figure 7.10: The cumulative amount of Tebuconazole in the receptor solution of the Franz cell for sprayed solutions: Surf1 + AI at two different concentrations (1 g/L orange squares, 3 g/L grey triangles) and Surf2 at 3 g/L (blue circles) plotted against time when the receptor cell is filled with Surf1 at 3 g/L. Error bars from 6 different measurements ( $\sigma_m$ ).

Surf1 at higher concentration gave the highest penetration of the AI followed by Surf1 at 1 g/L and Surf2 at 3 g/L, which both have similar behaviour. There is not a big difference between Surf1 at both concentrations as in infinite dose experiments. As Surf1 1 g/L + AI droplets dry, the water evaporates and Surf1 will be above the CMC and this might affect the penetration.

It has been shown that the addition of silica particles to Surf1 + AI formed a ring stain at all concentrations used (Section 5.7). Penetration of AI was studied when 0.25 wt% silica particles were added to Surf1 3 g/L + AI and sprayed on leaves to see any possible effect or not on the foliar penetration (Figure 7.11).

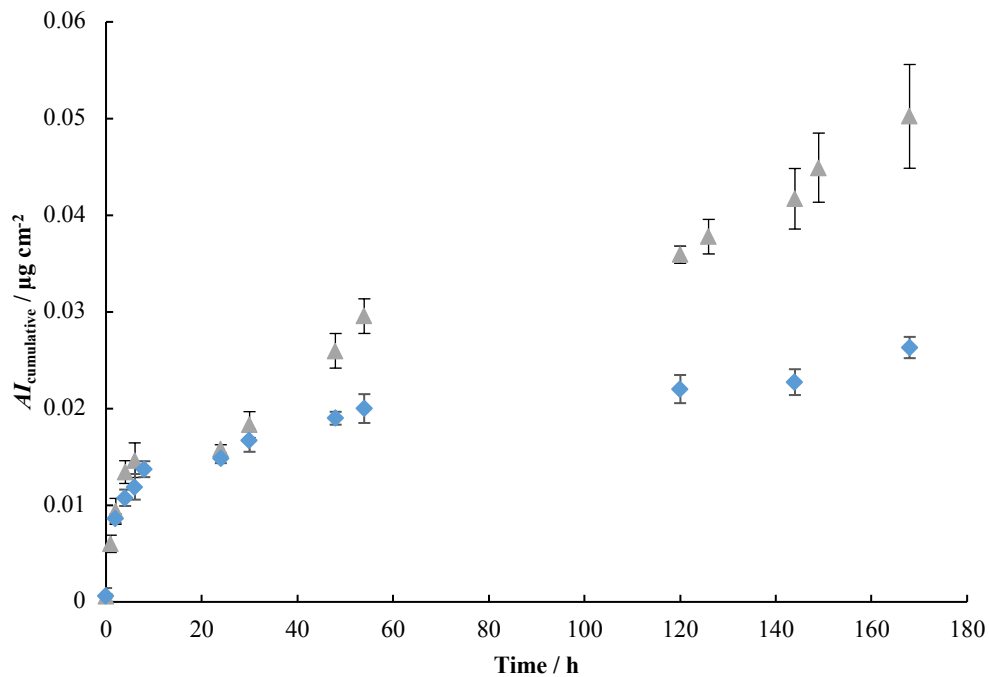


Figure 7.11: The cumulative amount of Tebuconazole in the receptor solution of the Franz cell for Surfl 3 g/L+ AI with (blue diamonds) and without (grey triangles) silica particles (0.25 wt%). Error bars from 5 different measurements for the silica experiments ( $\sigma_m$ ).

Figure 7.11 shows that the addition of silica particles did not enhance the penetration of AI.



## 7.4 Summary

Research on pesticide uptake and adjuvant application has gone through many years. Surfactants are included routinely in foliage-applied pesticide formulations to enhance their performance, however, the progress has been slow due to the poor understanding of how surfactants enhance the uptake of pesticides because it is a complex mechanism. Different surfactants act differently depending on the agrochemical and the target species. An ideal surfactant should produce the desired contact area on the leaf, keep the AI in a soluble form and increase the permeability of the cuticle<sup>43</sup>. The major rate-limiting barrier to penetration is the cuticle waxes which are located on the outer side of the CM. *Clivia* is an appropriate model plant as it does not have stomata that might affect the transport of AI.

Franz cell diffusion is a method to study the penetration of AI through the cuticles of leaves. The control experiments with no surfactant added showed that the penetration of AI was improved by the addition of surfactant. However, if the surfactant is below the CMC and the AI is present as monomers in solution or as crystals the penetration of AI is very similar to the previous free surfactant case. Surfactants above CMC or above the solubility limit showed the highest penetration.

The addition of a different surfactant in the receptor cell showed an increase in the transport rate behaviour for Surf2. Also, it seems that when Surf1 above the CMC is added to the donor cell, the penetration of AI is better than Surf2 even though the AI is dissolved on the dried deposit. The presence of micelles might be more efficient at transporting the tebuconazole .

Surfactants may interact with the structure of the leaf<sup>1</sup>. However, when a surfactant solution was applied for 48 h prior the addition of AI, there was no increase of the AI penetration at early stages. In fact, the initial rate of penetration through the membrane was reduced.

In order to approach the model as close to reality as possible the solution was studied in the form of droplets sprayed on the surface of the leaf using the simulation of foliar penetration method (SOFP). The sensitivity for the detection of AI in the receptor cell was increased by the addition of a surfactant solution at a concentration above the CMC to the receptor cell. Addition of surfactant to the receptor cell increases the partition coefficient of AI between the cuticle and the receptor cell due to a decrease in the chemical potential of the AI in the receptor solution caused by solubilization in micelles. The three formulations tested, Surf1 at both concentrations + AI and Surf2 3 g/L + AI showed very similar results in the spray experiments.

Franz cell diffusion is an established method for studying penetration of AI through the cuticles of the leaves, but the large variation within and between leaves means that it can be hard to draw firm conclusions on foliar efficiency.

## 8. Concluding remarks

Throughout this thesis many parameters have been shown to affect the morphology of the deposits that at the same time will affect the penetration of the AI through the cuticle of the leaf. In this thesis, two model surfaces (a silane-coated glass substrate (CDO) and *Clivia Miniata Regel*) were used, but they demonstrate the principles for the deposition of droplets and the penetration of AI on surfaces.

Surface tension and NMR experiments were combined in order to study the physico-chemical properties of two formulations, Surf1 (non-ionic surfactant) and Surf2 (cationic surfactant) without and with AI. Surface tensiometry and NMR can be used to determine the value of the CMC. The presence of micelles can be confirmed by studying the diffusion coefficient. It is confirmed that only Surf1 formed micelles. There was no difference in the diffusion coefficient for Surf2 at any of the concentrations tested, so it can be concluded that micelles are not formed.

Micelles can solubilize hydrophobic substances in their hydrophobic core. Solubility of AI in micelles and in neat surfactant was compared. It was also shown that the solubility of the AI on the deposit is equal to the saturation concentration. This is favorable for the application because when a droplet dries on a surface, only surfactant and AI remained on the deposit and the diffusion of Tebuconazole will be through the surfactant film.

The most important and fundamental physiochemical property of surfactants is the ability to lower interfacial tension between two phases. The lower surface tension, the higher spreading and the faster drying time. The addition of particles to the solution can also decrease the surface tension. In Surf1, the decrease in surface tension because the addition of AI might be due to some interaction of the AI at the air-liquid interface. For Surf2, there was no changes in the surface tension with the addition of particles.

After finding an accurate and reproducible method for studying the effects of droplet drying in agrochemical sprays, different strategies were applied in order to modify the morphology of the deposit since it is believed that the association between the

surfactant and AI is important for better uptake. SEM was used to study the morphology of a suspension (Surf1), where adjuvant and AI are mainly at the edge, and an emulsion (Surf2), where the AI is dissolved in the oil droplets. Surf2 at 1 g/L + AI is considered a supersaturated solution because some of the crystals crystallized out of solution over time. In supersaturated solutions, the chemical potential of the AI increases and it might have enhanced the transport of the AI through the leaf. However, Surf2 did not show a higher uptake than Surf1. The strategies used to modify the morphology of the deposit were: i) evaporation-driven sol-gel transitions by using Laponite and silica particles and ii) addition of “Superspreaders”. The addition of Laponite and silica particles increased the surface tension of the final formulations at any of the concentrations. Laponite formed uniform deposits because the CL receded obtaining deposit of a smaller area and silica particles did not suppress the CRE. The addition of “Superspreaders” did not have an effect on the whole morphology of the deposit, but the contact angle of the small droplets inside the deposit was lower and more uniform when Silwet Gold was added to Surf2 + AI at 0.03 wt%. A lower contact angle will give a better contact between the surface of the leaf and the deposit which is good for penetration.

Once the droplet is dried on the surface, two different techniques were used for the chemical characterization. EDS showed the distribution of surfactant and AI particles on the deposit, but it was not sensitive enough to detect the AI molecules in the surfactant film. Raman spectroscopy with the use of a narrower BP filter and even with strongly overlapping peaks detected the AI molecules in surfactant. The effectiveness of the technique was demonstrated by continued use by researchers in the group in systems with three components. The combination of Raman spectroscopy and <sup>1</sup>H-NMR was used to get a quantitative analysis of the chemical composition of selected areas on the deposit.

Franz cell diffusion was used to study the penetration of AI through the cuticles of leaves. It is shown that the penetration of AI was improved by the addition of surfactant to the formulation. However, if the surfactant is below the CMC and the AI is present as monomers in solution or as crystals the penetration of AI is very similar to the previous free surfactant case. Surfactants above CMC or above the solubility limit

showed the highest penetration for the infinite dose experiments. However, this method is not related to the drying process and formulations were sprayed on leaves by SOFP. Surfactant solutions above the CMC were added to the receptor cell to increase the partition coefficient of AI between the cuticle and the receptor cell. The three formulations tested, Surf1 at both concentrations + AI and Surf2 3 g/L + AI showed a very similar results in the spray experiments. The scattering of the FZ experiments was so high that it was difficult to correlate the results from the morphology studies with the efficacy. It would be necessary to develop better methods of measuring efficacy which were not involved in the field trials due to cost.

## 9. References

- <sup>1</sup> A. Fagerström, *PhD Thesis*, Malmö University, 2014.
- <sup>2</sup> E. Lichfouse, J. Schwarzbauer and D. Robert, *Green materials for energy, products and depollution*, Springer Science & Business Media, Heidelberg, Germany, 2013.
- <sup>3</sup> W. Krämer, U. Schirmer, P. Jeschke and M. Witschel, *Modern crop protection compounds*, (2nd ed). Wiley, Weinheim, Germany, 2012.
- <sup>4</sup> Börner, H, *Plant diseases and plant protection*, Springer, Berlin Heidelberg, Germany, 2009.
- <sup>5</sup> A. Buchholz, *J. Exp. Bot.*, 2006, **57**, 2501–2513.
- <sup>6</sup> M.A. Faers and R. Pontzen, *Pest. Manag Sci.*, 2008, **64**, 820–833.
- <sup>7</sup> R. C. Kirkwood, *Pestic. Sci.*, 1999, **55**, 69–77.
- <sup>8</sup> F. D. Hess and C. L. Foy, *Weed Technol.*, 2000, **14**, 807–813.
- <sup>9</sup> A.S. Craft, *Weeds*, 1960, **8**, 19-25.
- <sup>10</sup> P. J. Franks and G. D. Farquhar, *Plant Physiology*, 2007, **143**, 78–87.
- <sup>11</sup> J. Schonherr, *Planta*, 2000, **212**, 112–118.
- <sup>12</sup> J. Schonherr, *Journal of plant nutrition and soil science*, 2001, **164**, 225–231.
- <sup>13</sup> J. Schonherr, *Pest management science*, 2002, **58**, 343–351.
- <sup>14</sup> T. K. Schledel and J. Schonherr, *Planta*, 2005, **221**, 648–655.
- <sup>15</sup> J. Schonherr and L. Schreiber, *Planta*, **219**, 405–411.
- <sup>16</sup> W. D. Stein, *The movement of molecules across cell membranes*, Academic Press, London, New York, 1967.
- <sup>17</sup> T. J. Muzik, *Influence of environmental factors on toxicity to plants*, Vol. 2. Academic Press, London. 204–237, 1976.
- <sup>18</sup> C. E. Price, *The Association of Applied Biologists*, 1983, **4**, 157–169.
- <sup>19</sup> M.Devine, S. O. Duke and C. Fedtke, *Naturally occurring chemicals as herbicides*, In: M. D. Devine, S. O. Duke and C. Fedtke, editors. *Physiology of Herbicide Action*, Prentice Hall, Englewood Cliffs, New Jersey; 1993.

- <sup>20</sup> D. M. Anderson, C. J. Swanton, J. C. Hall, B. G. Mersey, *Weed Res.*, 1993, **33**, 139–147.
- <sup>21</sup> T. N. Jordan, *Weed Sci.*, 1977, **25**, 448–451.
- <sup>22</sup> P. J. Baur, *Agric. Food Chem.*, 1999, **47**, 753–761.
- <sup>23</sup> D. Penner, *Weed Technol.*, 2000, **14**, 785–791.
- <sup>24</sup> M. J. Castro and A. F. Cirelli, *Environ. Chem. Lett.*, 2014, **12**, 85–95.
- <sup>25</sup> S. Semenov, V. Starov, and R. G. Rubio, *Droplet wetting and evaporation: From pure to complex fluids*, ed. D. Brutin, UK, 2015.
- <sup>26</sup> W. C. Preston, *J. Phys. Colloid Chem*, 1948, **52**, 84–97.
- <sup>27</sup> M. J. Rosen, *Surfactants and interfacial phenomena*, Wiley, New York, US, 2nd Ed., 1989.
- <sup>28</sup> E. Kissa, *Liquid-Vapour and Liquid-Liquid Boundaries*, In: E. Kissa, Ed. Marcel Dekker Inc.: New York, 2001.
- <sup>29</sup> J. N. Israelachvili, *Intermolecular & Surface Forces*, Academic Press, California, USA 1991.
- <sup>30</sup> M. Miyake and Y. Einaga, *J. Phys. Chem. B*, 2007, **111**, 535–542.
- <sup>31</sup> E. Fischer, W. Fieber, C. Navarro, H. Sommers, D. Benczedi, M. I. Velazco and M. Schonhoff, *J. Surfactants Deterg.*, 2008, **12**, 1104–1108.
- <sup>32</sup> G. Danchen, A. S. Narang and D. Delmare, *Inter. J. of Paharmaceutics*, 2007, **345**, 9–25.
- <sup>33</sup> M. J. Hou and D. O. Shah, *Langmuir*, 1987, **3**, 1086–1096.
- <sup>34</sup> R. E. Gaskin and P. J. G. Stevens, *Pestic. Sci.*, 1993, **38**, 185–192.
- <sup>35</sup> Z. Q. Liu, *J. Agric. Res.*, 2003, **54**, 877–884.
- <sup>36</sup> C. J. Wang and Z. Q. Liu, *Pesticide Biochem. and Physiology*, 2007, **87**, 1–8.
- <sup>37</sup> D. Stock and P. J. Holloway, *Pestic. Sci.*, 1993, **38**, 165–177.
- <sup>38</sup> F. D. Hess and C. L. Foy, *Weed Technol.*, 2000, **14**, 807–813.
- <sup>39</sup> W. C. Griffin, *J. Cosmet. Sci.*, 1949, **5**, 311–326.
- <sup>40</sup> W. C. Griffin, *J. Cosmet. Sci.*, 1954, **5**, 249–256.
- <sup>41</sup> J. D. Nalewaja, and R. Matysiak, *Weed Res.*, 1996, **36**, 241–247.
- <sup>42</sup> Nuyttens, D., De Schampheleire, M., Baetens, K., Sonck, B., *Biol Eng Trans.*,

2007, **50**, 1129–1140.

<sup>43</sup> M. Schampheleire, D. Nuyttens, K. Baetens, W. Cornelis, D. Gabriels and P. Spanoghe, *Precis. Agric.*, 2009, **10**, 409–420.

<sup>44</sup> E. R. Lee, *Microdrop Generation*, CRC PRESS, FL, USA, 2003.

<sup>45</sup> E. Q. Li, Q. Xu, J. Sun, J. Y. H. Fuh, Y. S. Wong, S. T. Thoroddsen, *Sens. Actuators A: Phys.*, 2010, **163**, 315–322.

<sup>46</sup> H. Ulmke, T. Wriedt, H. Lohner and K. Bauckhage, in *Precision Engineering e Nanotechnology 1st International European Conference 1999*, 290–293.

<sup>47</sup> H. Ulmke, T. Wriedt and K. Bauckhage, *Chem. Eng. Technol.*, 2001, **24**, 265–268.

<sup>48</sup> F. Kuang-Chao, C. Jhing-Yuan, W. Ching-Hua and Wen-Chueh, *Sens. Actuators A Phys.*, 2008, **137**, 649–655.

<sup>49</sup> R. E. Saunders, J. E. Gough and B. Derby, *Biomaterials*, 2008, **29**, 193–203.

<sup>50</sup> J. Luo, L. H. Qi, J. M. Zhou, Y. Xiao and F. Yang, *China Technol. Sci.*, 2011, **54**, 1833–1840.

<sup>51</sup> J. Castrejon-Pita, G. Martin, S. Hoat and I. Hutchings, *Rev. Sci. Instrum.*, 2008, **79**, 1081–1082.

<sup>52</sup> O. A. Basaran, H. Gao and P. P. Bhat, *Annu. Rev. Fluid Mech.*, 2013, **45**, 85–113.

<sup>53</sup> I. M. Hutchings and G. D. Martin, in *Inkjet Technology for Digital Fabrication*, eds. I. M. Hutchings and G. D. Martin, John Wiley & Sons, Ltd., Chichester, U.K., 2013.

<sup>54</sup> A. Fagerström, V. Kocherbitov, T. Ruzgas, P. Westbye, K. Bergström, and J. Engblom, *Colloids and Surfaces B: Biointerfaces*, 2013, **103**, 572–579.

<sup>55</sup> T. J. Franz, *J. Invest. Dermatol.*, 1975, **52**, 190–195.

<sup>56</sup> C. Popp, M. Burghardt, A. Friedmann and M. Reiderer, *J. Exp. Bot.*, 2005, **56**, 2797–2806.

<sup>57</sup> A. Fagerstrom, V. Kocherbitov, P. Westbye, K. Bergstrom, V. Mamontova and J. Engblom, *Thermochimica Acta*, 2013, **571**, 42–52.

<sup>58</sup> J. H. de Boer, *The Dynamic Character of Adsorption*, Clarendon Press, Oxford, UK, 1968.

<sup>59</sup> M. A. Kohanski, D. J. Dwyer and J. J. Collins, *Nat. Rev. Microbiol.*, 2010, **8**, 423–435.

<sup>60</sup> J. Park J and J Moon, *Langmuir*, 2006, **22**, 3506–3517.

<sup>61</sup> P. Calvert P, *Chem Mater.*, 2001, **13**, 3299–3313.



- <sup>62</sup> Y. Yu, H. Zhu, J. M. Frantz, M. E. Reding, K. C. Chan and H. E. Ozkan, *Biosystems Eng.*, 2009, **104**, 324–331.
- <sup>63</sup> D. Y. Xia and S. R. Brueck, *Nano Lett.*, 2008, **8**, 2819–2824.
- <sup>64</sup> M. Kimura, M. J. Misner, T. Xu, S. H. Kim and T. P. Russel, *Langmuir*, 2003, **19**, 9910–9916.
- <sup>65</sup> V. X. Nguyen and K. Stebe, *J Phys Rev Lett.*, 2002, **88**, 164501–1645015.
- <sup>66</sup> W. Jia and H.H. Qiu, *Exp Therm Fluid Sci.*, 2003, **27**, 829–838.
- <sup>67</sup> D. Bensimon, A. J. Simon, V. Croquette and A. Bensimon. *Phys Rev Lett.*, 1995, **74**, 4754–4757.
- <sup>68</sup> X. Fang, B. Li, E. Petersen, Y. S Seo, V. A. Samuilov and Y. Chen, *Langmuir*, 2006, **22**, 6308–6312.
- <sup>69</sup> T. Kawase, H. Siringhaus, R. H. Friend and T. Shimoda, *Adv Mater*, 2001, **13**, 1601–1609.
- <sup>70</sup> K. N. Prabhu, P. Fernandes and G. Kumar, *Mater. Des.*, 2009, **2**, 297–305.
- <sup>71</sup> X. Zhao, M. J. Blunta and J. J. Yao, *Pet. Sci. Technolo. Eng.*, 2010, **71**, 169–178.
- <sup>72</sup> Y. Son, C. Kim, D. H. Yang and D. J. Ahm, *Langmuir*, 2008, **24**, 2900–2907.
- <sup>73</sup> E. L. Talbot, A. Berson, P. S. Brown and C. B. Bain, *Phys. Rev. E*, 2012, **6**, 85–90.
- <sup>74</sup> Y. Yuan and T. R. Lee, *Contact Angle and Wetting Properties, vol 51*, Springer, Berlin and Heidelberg, 2013.
- <sup>75</sup> Y. F. Li, *Langmuir*, 2014, **30**, 7716–7723.
- <sup>76</sup> T. Young, *Philos. Trans. R. Soc.*, 1805, **95**, 65–87.
- <sup>77</sup> R. E. Johnson and R. H. Dettre, *Phys. Chem.*, 1964, **68**, 1744–1750.
- <sup>78</sup> L. W Schwartz and S. Garoff, *Langmuir*, 1985, **1**, 219–230.
- <sup>79</sup> J. F. Joanny and P. G. Gennes, *Chem. Phys.*, 1984, **81**, 552–562.
- <sup>80</sup> K. Selfiane, *Langmuir*, 2015, **31**, 3653–3660.
- <sup>81</sup> J. M. Stauber, S. K. Wilson and B. R. Duffy, *Langmuir*, 2015, **31**, 3653–3660.
- <sup>82</sup> M. E. R. Shanahan, *Langmuir*, 1995, **11**, 1041–1043.
- <sup>83</sup> H. Hu and R. G. Larson, *J. Phys. Chem. B*, 2002, **106**, 1334–1344.

- <sup>84</sup> Y. O. Popov, *Phys. Rev. E*, 2005, **71**, 1–17.
- <sup>85</sup> C. Poulard, G. Guena and A. M. Cazabat, *Condens. Matter*, 2005, **17**, 4213–4227.
- <sup>86</sup> H. Y. Erbil, *Adv. Colloid Interface Sci.*, 2012, **170**, 67–86.
- <sup>87</sup> H. Gelderblom, *PhD Thesis*, University of Twente, The Netherlands, 2013.
- <sup>88</sup> H. K. Cammenga, *Curr. Top. in Mater. Sci.*, 1980, **5**, 335–446.
- <sup>89</sup> R. G. Larson, *AIChE J.*, 2014, **60**, 1538–1571.
- <sup>90</sup> G. J. Dunn, S. K. Wilson, B. R. Duffy, S. David and K. Sefiane, *J. Fluid Mech.*, 2009, **623**, 329–351.
- <sup>91</sup> R. D. Deegan, O. Bakajin, T. F. Dupont, G. Huber, S. R. Nagel and T. A. Witten, *Nature*, 1997, **389**, 827–829.
- <sup>92</sup> M. A. Faers and R. Pontzen, *Pest Manag Sci.*, 2008, **64**, 820–823.
- <sup>93</sup> M. Anyfantakis, D. Baigl and B. P. Binks, *Langmuir*, 2017, **33**, 5025–5036.
- <sup>94</sup> E. L. Talbot, L. Yang, A. Berson and C. D. Bain, *ACS Appl. Mater. Interfaces*, 2014, **6**, 9572–9583.
- <sup>95</sup> J. Thompson, *The London, Edinburgh and Dublin Philosophical Magazine and Journal of Science*, 1855, **10**, 330–333.
- <sup>96</sup> Y. Hamamoto, J. R. Christy and K. Sefiane, *J. Therm. Sci. Technol.*, 2012, **7**, 425–436.
- <sup>97</sup> J. Park and J. Moon, *Langmuir*, 2006, **22**, 3506–3513.
- <sup>98</sup> K. Sefiane, *J. Pet. Sci. Eng.*, 2006, **51**, 238–252.
- <sup>99</sup> O. A. Soboleva and B. D. Summ, *J. Colloid Interface Sci.*, 2003, **65**, 89–93.
- <sup>100</sup> G. Gutierrez, J. M. Benito, J. Coca and C. J. Pazos, *Chem. Eng.*, 2010, **162**, 201–207.
- <sup>101</sup> S. J. Gokhale, J. L. Plawsky, P. C. Wayner, *Langmuir*, 2005, **21**, 8188–8197.
- <sup>102</sup> P. Alexandridis, S. Z. Munshi, Z. Gu, *Ind. Eng. Chem. Res.*, 2011, **50**, 580–589.
- <sup>103</sup> A. W. Adamson and A. P. Gast, *Physical Chemistry of Surfaces*, John Wiley & Sons, Inc., New York, U.S.A., 6th edn., 1997.
- <sup>104</sup> C. V. Raman and K. S. Krishnan, *Nature*, 1928, **121**, 501–502.
- <sup>105</sup> A. Smekal, *Nature*, 1923, **11**, 873–875.

- <sup>106</sup> F. A. Settle, *Handbook of instrumental techniques for analytical chemistry*, Prentice Hall, New Jersey, 1997.
- <sup>107</sup> T. L. Meragelman, *J. Nat. Prod.*, 2005, **68**, 1578–1579.
- <sup>108</sup> J. M. Laundry, D. G. Marangoni, M. D. Lumsden and R. Berno, *Canadian Journal of Chemistry*, 2007, **87**, 202–207.
- <sup>109</sup> U. R. Kjellin, J. Reimerand and P. Hansson, *J. Colloid Interface Sci.*, 2003, **262**, 506–515.
- <sup>110</sup> M. J. Blandamer, P. M. Cullis, L. G. Soldi, J. B. F. Engberts, A. Kacperska, N. Van and M. C. Subha, *Adv. Colloid Interfaces*, 1995, **58**, 171–209..
- <sup>111</sup> S.D. Wettig and R. E. Verrall, *J. Colloid Interface Sci.*, 2001, **235**, 310–315.
- <sup>112</sup> M. E. Amato, E. Caponetti, D. C. Martino and L. Pedone, *J. Phys. Chem.B.*, 2003, **107**, 10048–10056.
- <sup>113</sup> C. Tandford, *The hydrophobic effect: formation of micelles and biological membranes*, 2nd ed.; John Wiley and Sons, New York, 1980.
- <sup>114</sup> H. J. Hunter, *Foundations of Colloid Science*, Clarendon Press; Oxford, Vol 1, 1987.
- <sup>115</sup> M. Rosen, *Surfactants and Interfacial Phenomena*, John Wiley and Sons, Inc., New York, 1989.
- <sup>116</sup> D. Attwood and A. T. Florence, *J. Pharm. Sci.*, 1985, **74**, 1140–1141.
- <sup>117</sup> J. D. Nalewaja and R. Matysiak, *Weed Technol.*, 2000, **14**, 740–749.
- <sup>118</sup> R. Matysiak, Role of adjuvants in product retention and form of deposit on targets, in *Proc Fourth Internat Symp on Adjuvants for Agrochemicals – FRI Bulletin No. 193 (Melbourne, Australia)*, ed. by Gaskin RE. New Zealand Forest Research Institute, Rotorua, New Zealand, pp. 112–119 (1995).
- <sup>119</sup> Nalewaja JD and Matysiak R, Nicosulfuron response to adjuvants, salts, and spray volume, in *Proc Sixth Internat Symp on Adjuvants for Agrochemicals (Amsterdam, The Netherlands)*, ed. by de Ruiter H. International Society for Agrochemical Adjuvants, Wageningen, The Netherlands, pp. 304–314 (2001).
- <sup>120</sup> Bukovac MJ, Leon JM, Cooper JA, Whitmoyer RE, Reichard DL and Brazee RD, Spray droplet: plant surface interaction and deposit formation as related to surfactants and spray volume, in *Proc Fourth Internat Symp on Adjuvants for Agrochemicals – FRI Bulletin No. 193 (Melbourne, Australia)*, ed. by Gaskin RE. New Zealand Forest Research Institute, Rotorua, New Zealand, pp. 177–185 (1995).
- <sup>121</sup> P. J. G. Stevens and E. A. Baker, *Pestic Sci.*, 1987, **19**, 265–281.

- <sup>122</sup> Faers MA, Tsangaris K, Pontzen R and Bismarck A, Studies on leaf deposit microstructures through changes in colloidal and surface forces, in *Proc Ninth Internat Symp on Adjuvants for Agrochemicals (Freising, Germany)*, ed. by Baur P and Bonnet M. International Society for Agrochemical Adjuvants, Wageningen, The Netherlands, pp. 309–318 (2010).
- <sup>123</sup> R. D. Deegan, O. Bakajin, T. F. Dupont, G. Huber, S. R. Nagel, and T. A. Witten, *Phys. Review E*, 2000, **62**, 756–765.
- <sup>124</sup> P. Baur, *J. Agric. Food Chem.*, 1999, **47**, 753–761.
- <sup>125</sup> D. Stock and G. Briggs, *Weed Technol.*, 2000, **14**, 798–806.
- <sup>126</sup> S. Phongikaroon, R. Hoffmaster, K. P. Judd, G. B. Smith, and R. A. Handler, *Journal of Chemical & Engineering Data*, 2005, **50**, 1602–1607.
- <sup>127</sup> M. Hunsche and G. Noga, *Pest. Manag. Sci.*, 2012; **68**, 231–239.
- <sup>128</sup> H. Zhu, Y. Yu, H. E. Ozkan, R. C. Derksen and C. R. Krause, *ASABE Annual International Meeting*, Sponsored Convection Center Providence, Rhode Island, 2008.
- <sup>129</sup> G. T. Cook, A. G. T. Babiker, and H. J. Duncan, *Pestic. Sci.*, 1977, **8**, 137–146.
- <sup>130</sup> W. B. Zeid and D. Brutin, *Colloids and Surfaces A: Physicochem. Eng. Aspects*, 2013, **430**, 1–7.
- <sup>131</sup> H. Z. Cummins, *J. Non-Cryst. Solids*, 2007, **353**, 3891–3905.
- <sup>132</sup> [https://www.byk.com/fileadmin/byk/additives/product\\_groups/rheology/former\\_rockwood\\_additives/technical\\_brochures/BYK\\_B-RI21\\_LAPONITE\\_EN.pdf](https://www.byk.com/fileadmin/byk/additives/product_groups/rheology/former_rockwood_additives/technical_brochures/BYK_B-RI21_LAPONITE_EN.pdf)
- <sup>133</sup> G. Michael and H. Ferch, *Schriftenreihe Pigmente*, Degussa AG (F.R.G.), 1991, **11**, 63–74.
- <sup>134</sup> S. Zhu, W. G. Miller, L. E. Scriven and H.T. Davis, *Colloids & Surfaces A*, 1994, **90**, 63–78.
- <sup>135</sup> O. E. Jensen, *Phys. Fluids*, 1994, **6**, 1084–1094.
- <sup>136</sup> Eugene Hecht, *Optics*, in 385–442, Addison Wesley, 2002.
- <sup>137</sup> A. Puri, *Weed Biol. Manag.*, 2008, **8**, **1**, 133–138.
- <sup>138</sup> R. E. Gaskin and P. J. G. Stevens, *Pestic. Sci.*, 1993, **38**, 185–200.
- <sup>139</sup> S.A. MacIsaac, R.N. Paul and M.D. Devine, *Pestic. Sci.*, 1991, **31**, 65–72.
- <sup>140</sup> P. Baur and R. Pontzen, Basic features of plant surfaces wettability and deposit formation and the impact of adjuvants in *Proc Eighth Internat. Symp. on adjuvants for agrochemicals*, Christchurch, New Zealand, 2007.

- <sup>141</sup> P. J. Holloway, *The Plant Cuticle*, Academic Press, London, 1982
- <sup>142</sup> W. A. Forster, J. A. Zabkiewicz and M. Rieder, *Pest. Management Sci.*, 2004, **6**, 1105–1113.
- <sup>143</sup> P. Baur, *Plant Cell and Environ.*, 1997, **20**, 982–994.
- <sup>144</sup> P. Baur, *Pestic. Sci.*, 1997, **51**, 121–152.
- <sup>145</sup> N. G. Shioh-Fern, J. Rouse, D. Sanderson and G. Eccleston, *Pharmaceutics*, 2010, **2**, 209–223.
- <sup>146</sup> B. Desmedt, P. Courselle, J. O. De Beer, V. Rogiers, M. Grosber, E. Deconinck and K. De Paepe, *J. Eur. Acad. Dermatol. Venereol.*, 2016, **30**, 943–950.
- <sup>147</sup> D. F. Evans and H. Wennerstrom, *The Colloidal Domain: Where Physics, Chemistry, Biology and Technology Meet*, Wiley, New York, USA, 1999, **657**, 195–198.
- <sup>148</sup> C. Leo, D. Hansch and D. Elkins, *Chem. Rev.*, 1971, **71**, 525–616.
- <sup>149</sup> A. Fagerström, V. Kocherbitov, P. Westbye, , K. Bergström, J. Engblom, *Thermochim. Acta*, 2013, **57**, 42–52.
- <sup>150</sup> A. Fagerström, V. Kocherbitov, T. Ruzgas, P. Westbye, K. Bergström and J. Engblom, *Colloids Surf. B*, 2013, **103**, 572–579.
- <sup>151</sup> P. J. Holloway and D. Stock, *Factors affecting the activation of foliar uptake of agrochemicals by surfactants*, Royal Society of Chemistry, Cambridge, UK, 1990.
- <sup>152</sup> M. F. Cox, *J. Am. Oil Chem. Soc.*, 1989, **66**, 367–374.
- <sup>153</sup> G. Noga, M. Wolter, W. Barthlott and W. Petry, *Angrew. Botanik*, 1991, **65**, 239–252.